Polymeric Nanocarriers: From Preparation to Understanding their Behavior in the Blood Stream

Dissertation zur Erlangung des Grades

“Doktor der Naturwissenschaften”

im Promotionsfach Chemie

am Fachbereich Chemie, Pharmazie,

Geographie und Geowissenschaften

der Johannes Gutenberg-Universität in Mainz

vorgelegt von

Sascha Schmitt

geboren in Waiblingen

Mainz, April 2022

Die vorliegende Arbeit wurde im Zeitraum von Oktober 2018 bis April 2022 am Max-Planck-Institut für Polymerforschung in Mainz unter Anleitung von Herrn Prof. Dr. [redacted] und Herrn Dr. [redacted] angefertigt.

Mainz, 28. April 2022

1. Berichterstatter: Prof. Dr. [redacted]

2. Berichterstatter: Prof. Dr. [redacted]

3. Berichterstatter: Prof. Dr. [redacted]

D77 (Dissertation Mainz)

Declaration

I hereby declare that I wrote the dissertation submitted without any unauthorized external assistance and used only sources acknowledged in the work. All textual passages which are appropriated verbatim or paraphrased from published and unpublished texts as well as all information obtained from oral sources are duly indicated and listed in accordance with bibliographical rules. In carrying out this research, I complied with the rules of standard scientific practice as formulated in the statutes of Johannes Gutenberg-University Mainz to insure standard scientific practice.

Sascha Schmitt

„Semper Paratus“

Danksagung

[In der elektronischen Fassung aus Datenschutzgründen entfernt]

Zusammenfassung

Die Verwendung von Nanopartikeln als Transportvehikel, um Medikamente über die Blutbahn zu ihrem Zielort innerhalb des Körpers zu bringen, ist ein vielversprechender therapeutischer Ansatz für eine wirksame Behandlung verschiedener Krankheiten. Über die letzten Jahre wurden viele Forschungsanstrengungen unternommen hinsichtlich der Synthese, Charakterisierung, Wirkstofffreigabe, und dem Verhalten von Nanopartikeln unter *in vitro* und *in vivo* Bedingungen. Zielsetzung dieser Arbeit ist es, zwei Forschungsbereiche näher zu beleuchten, nämlich den Bildungsprozess von Nanopartikeln und die Charakterisierung von Nanopartikeln in komplexen Umgebungen wie Vollblutproben.

Der Entstehungsprozess von Nanopartikeln ist, aufgrund fehlender geeigneter Untersuchungsmethoden, mechanistisch nicht gut untersucht. Speziell der Übergang der initial gebildeten Emulsionstropfen zur finalen Partikeldispersion ist nur unzureichend verstanden. Daher befasst sich der erste Teil dieser Arbeit mit dem Entstehungsprozess von polymerbasierten Nanopartikel. Untersucht werden zwei verschiedene Synthese Ansätze: die Lösungsmittelverdampfung aus Emulsionstropfen und die Miniemulsionspolymerisation. Vorgestellt wird ein Ansatz, der zwei Charakterisierungstechniken kombiniert, die zeitkorrelierte Einzelphotonenzählmethode und die Fluoreszenzkorrelationsspektroskopie, um den Entstehungsprozess der Nanopartikel zu verfolgen. Hierfür, wird ein fluoreszierender molekularer Rotor in die Emulsionstropfen eingekapselt. Über Messungen der Fluoreszenzlebensdauer des molekularen Rotors konnten lokale Viskositätsänderungen in Abhängigkeit des Reaktionsfortschrittes detektiert werden. Zeitgleich konnte über FCS Messungen die Größenänderung während der Reaktionen verfolgen werden.

Die Charakterisierung von Nanopartikeln in komplexen Umgebungen wie Blut, gestaltet sich schwierig, aufgrund der zellulären Bestandteile von Blut, die während einer FCS Messung das Detektionsvolumen besetzen können und somit die FCS Messung verhindern. Daher wird im zweiten Teil ein neu entwickelter Ansatz präsentiert, welcher es ermöglicht, das FCS Detektionsvolumen während einer Messung frei von zellulären Bestandteilen zu halten. Hierfür wurde eine Membran verwendet, welche für Blutzellen undurchlässig ist. Um die Praktikabilität des hier vorgestellten Ansatzes zu demonstrieren, wurden Nanopartikel einer Maus injiziert und die entnommen Blutproben untersucht. Es wurde festgestellt, dass die Nanopartikel bis zu drei Tage nach Injektion noch in den Blutproben nachgewiesen werden konnten.

Abstract

The use of nanocarriers (NCs) to deliver small and sensible drugs to their target site inside the body via the blood stream is a promising approach for the effective treatment of different diseases. Over the last decades, a lot of research effort has been done regarding NCs designed for drug delivery reaching from the synthesis and the characterization to studying the behavior of these NCs *in vitro* and *in vivo*. The objective of this thesis is to look closer into two research fields: the first part of the thesis will deal with the monitoring of the formation process of nanoparticles, whereas the second part of this thesis will present a newly developed experimental method for NCs characterization in whole blood samples.

Due to a lack of suitable characterization methods, a broad understanding of the mechanism regarding the formation process of nanoparticles is still missing. Especially, a broad understanding of the transition of the initial emulsion droplets to the final nanoparticle dispersion is missing. Therefore, the first part of this thesis will investigate the formation process of polymeric nanoparticles with two commonly used methods: the solvent evaporation from emulsion droplets process and the miniemulsion polymerization. Here an approach is presented which combines two characterization techniques the time-correlated single-photon counting method and the fluorescence correlation spectroscopy to follow the formation process. A tailored fluorescent molecular rotor acts as a reporter and provides information from the inside of the emulsion droplets. The recorded fluorescence lifetime reflected local viscosity changes in dependence on the reaction progress. Further, the fluorescence signal of the molecular rotor is also utilized to track the evolution of the size during the reaction.

Characterizing nanoparticles in more complex environments such as blood is difficult due to the cellular components of blood which can occupy the FCS detection volume, preventing the recording of autocorrelation curves. Therefore, the second part of this thesis will introduce a newly developed approach that enables FCS measurements in small whole blood samples by preventing the cellular fraction to enter the FCS detection volume. To accomplish this, a membrane was used which separates the liquid part of the blood from the cellular fraction. This approach enabled a unique way for following the fate of NCs in living mice with FCS experiments. Small blood (~ 50 µL) samples were collected at predefined time points after injection of the NCs and measured with the newly developed approach. It was possible to follow the injected NCs for up to 72 hours inside the mouse.

Table of Content

Abbreviations

AIBN	**A**zob**i**siso**b**utyro**n**itrile
CRC	**C**ollaborative **r**esearch **c**enter
DLS	**D**ynamic **l**ight **s**cattering
FCS	**F**luorescence **c**orrelation **s**pectroscopy
IRF	**I**nstrument **r**esponse **f**unction
MEP	**M**ini**e**mulsion **p**olymerization
NCs	**N**ano**c**arrier**s**
NIR	**N**ear-**i**nfrared **r**egion
OD	**O**ptical **d**ensity
PBS	**P**hosphate-**b**uffered **s**aline
PEG	**P**oly**e**thylene **g**lycol
PNPs	**P**olymeric **n**ano**p**article**s**
PS	**P**oly**s**tyrene
SEED	**S**olvent **e**vaporation from **e**mulsion **d**roplets
SEM	**S**canning **e**lectron **m**icroscopy
TCSPC	**T**ime **c**orrelated **s**ingle **p**hoton **c**ounting
TEM	**T**ransmission **e**lectron **m**icroscopy
TICT	**T**wisted **i**ntramolecular **c**harge **t**ransfer

1. Introduction

The word polymer is derived from the Greek word “poly” which means “many” and “meres” meaning “parts”. Hence, polymers are made of repeating units, called monomers, and can reach very high molar masses.[1] Polymers possesses a broad application range reaching from plastic bags to cloths made of synthetic fibers[1], and from electronics[2-4] to medical implants[5, 6]. Besides synthetic polymers, biopolymers like DNA and proteins are fundamental for biology. Due to their natural occurrence and biocompatibility, biopolymers are also utilized in the biomedical, food, and biofuel sectors.[7, 8]

Interestingly, the properties of polymeric bulk materials change, if the dimensions of these materials are decreased to a nanometer size range of around 1 to 100 nm.[9, 10] Polymeric nanoparticles (PNPs) can be used in different application fields ranging from electronics and photonics to biotechnology and medicine.[11-16] Especially the application of PNPs as nanocarriers (NCs) in the medical field is very promising. The possibility to encapsulate small drug molecules in such NCs can increase the drug molecules stability by protecting them during their transportation inside the blood vessel system, reducing potential side effects, and can alter their pharmacokinetics.[13, 16-23] Further, the NCs can be fully optimized for a specific target inside the body. The material, size, shape, and surface functionalization are only a few parameters that can be optimized.[13, 15, 16, 20, 24]

Nowadays, several NCs designed for drug delivery got approved in the USA or in South Korea e.g. Doxil® or Genexol-PM.[13, 16, 25] The aforementioned approved nanomedicines are relying on different NCs architectures to deliver the encapsulated drug to their target site. For example, the NC architecture of Doxil® is based on phospholipids assembled into a liposome encapsulating the drug doxorubicin. Liposomes are spherical vesicles consisting of a lipid bilayer membrane structure. Due to their bilayer structure liposomes can encapsulate hydrophilic drug agents in their aqueous core, while hydrophobic drugs can be encapsulated in the hydrophobic regions of the bilayer.[23, 25] In different to Doxil®, the utilized NC architecture for the nanomedicine Genexol-PM is based on a polymeric micelle. Polymeric micelles consist of block-copolymers which self assemble into micelles with a hydrophobic core and a hydrophilic shell.[16, 26] The self-assembling of the block-copolymers into micelles occurs spontaneously after a certain concentration is reached, the so-called critical micellar concentration. The micelle used for Genexol-PM consists of the block-copolymer poly(ethylene glycol)-poly(D,L-lactide) which encapsulates the drug paclitaxel. Besides poly(D,L-lactide) other polymers like poly(lactide-*co*-glycolide), polycaprolactone, poly(glutamic acid), and *N*-(2-hydroxypropyl)meth-acrylamide are utilized as building materials for NCs.[22, 26, 27] Further, naturally occurring polymers are also considered for building NCs including albumin, dextran, gelatin, and heparin.[27-29]

For a broad understanding of the NC-mediated drug delivery process, it is necessary to possess information about the whole process, reaching from the synthesis of the NCs to the drug release at the target site inside the body. Therefore, two research fields can be identified which contribute toward a broad understanding of the NC-mediated drug delivery processes. On the one hand, researchers conduct mechanistic studies on the NCs formation in aqueous environments, including the formation process of NCs, encapsulation efficiency, optimizing the stability in different environments reaching from aqueous buffer to human blood plasma, and biocompatibility studies.[30-32] On the other hand, researchers concentrate on studies performed in cells and *in vivo*. Here, the research interests focus on the drug delivery process, cellular uptake, drug release, and toxicity studies.[19, 33-36]

Synthesizing PNPs can be achieved by various synthesis strategies. Commonly used strategies for producing PNPs are based on emulsified systems.[37] For example, PNPs can be produced by emulsification of pre-synthesized polymer with subsequent evaporation of the discontinuous phase.[38-40] Contrary to using pre-synthesized polymers, PNPs can also be produced by emulsifying monomers with subsequent polymerization.[12, 40, 41] Advantageous of using emulsion droplets as “nanoreactors” is the controllable size of these droplets by emulsifying methods e.g. ultrasonication.[42] Further, the aforementioned methods hold the potential for encapsulation of different compounds[43] or to build complex morphologies[44]. After the synthesis of the PNPs, the final particle dispersion can be characterized by several methods including dynamic light scattering, nanoparticle tracking analysis, fluorescence correlation spectroscopy (FCS), size exclusion chromatography, zeta potential measurements, or scanning electron microscopy.[45, 46] These techniques can characterize PNPs in an aqueous environment like buffer solutions in regards to stability, aggregation behavior, size, and premature drug release.

Despite huge research efforts over the past years, open questions and challenges remain in the field of nanoparticle synthesis and characterization. For example, the stabilization mechanism of emulsified systems is well understood[38, 39, 47, 48], but mechanistic studies to obtain information about the transition from the initial liquid nanodroplet to the final particle dispersion are still missing. The polymerization rate during the formation process of PNPs can be determined using e.g. calorimetric methods, but this method does not provide further information about the local viscosity and morphology of the PNPs. In general, there is a lack of experimental techniques which are able to probe nanoparticles regarding their inner morphology and structure while diffusing in a continuous phase. With this in mind, Chapter 3 of this thesis presents a mechanistic study on the possibility of utilizing a tailored fluorescent probe and combining time-correlated single-photon counting and FCS for gaining information about the inner morphology and simultaneously tracking the size evolution during the PNP formation process. Two commonly used synthesis strategies for PNPs are explored, the solvent evaporation from emulsion droplets and the miniemulsion polymerization are investigated and compared.

Another challenging undertaking is the characterization of NCs in complex biological environments like blood. The complexity of blood arises from an increased scattering and absorption coefficient[49] and a high concentration of cells and blood plasma proteins. Predetermined properties of NCs in an aqueous environment can change if they are in contact with blood. Interaction between the NC and the blood can lead to a formation of a protein corona[50, 51], aggregation, degradation, or inducing a premature drug release[52]. The stability of NCs is crucial for a successful delivery process and if the NC suffers a drug leakage during the transportation in the blood vessel system it can be harmful to healthy tissue. Therefore, studying NCs in blood is important to understand how the NC behaves in contact with blood. Commonly utilized characterization techniques like dynamic light scattering, size exclusion chromatography, or scanning electron microscopy cannot be applied in blood, due to the high concentration of cells and blood plasma proteins. Therefore, an experimental FCS approach for NCs characterization in whole blood samples is presented in Chapter 4. The new approach enables FCS blood measurements with small blood volumes (~ 50 µL) and without the need for further sample preparation, thus allowing *ex vivo* monitoring of the fate of drug NCs in the blood stream over long periods of time.

Furthermore, cooperative projects as part of the collaborative research center (CRC) 1066 utilizing the FCS technique are presented in Chapter 5. The objective of the CRC1066 is to develop multi-functional NCs for the effective treatment of malignant melanoma. The developed PNPs which are used as NCs can be monitored with the FCS technique regarding the size, investigation of the stability in e.g. blood plasma, drug loading efficiency, and tracking of the kinetic of reactions.[53] Here, the role of FCS for the publication will be outlined.

2. Physical Phenomena and Methods

2.1. Fluorescence

Luminescence describes the physical phenomena of light emission from an electronically excited state.[54] Luminescence can be divided into two categories, namely fluorescence and phosphorescence. The process of emitting photons from a singlet state is called fluorescence and it is called phosphorescence if photons are emitted from a triplet state. Absorption and emission processes can be illustrated and explained with a Jablonski diagram (Figure 1). The Jablonski diagram schematically shows the underlying fundamental physical processes which can occur when a fluorophore absorbs light.[54, 55]

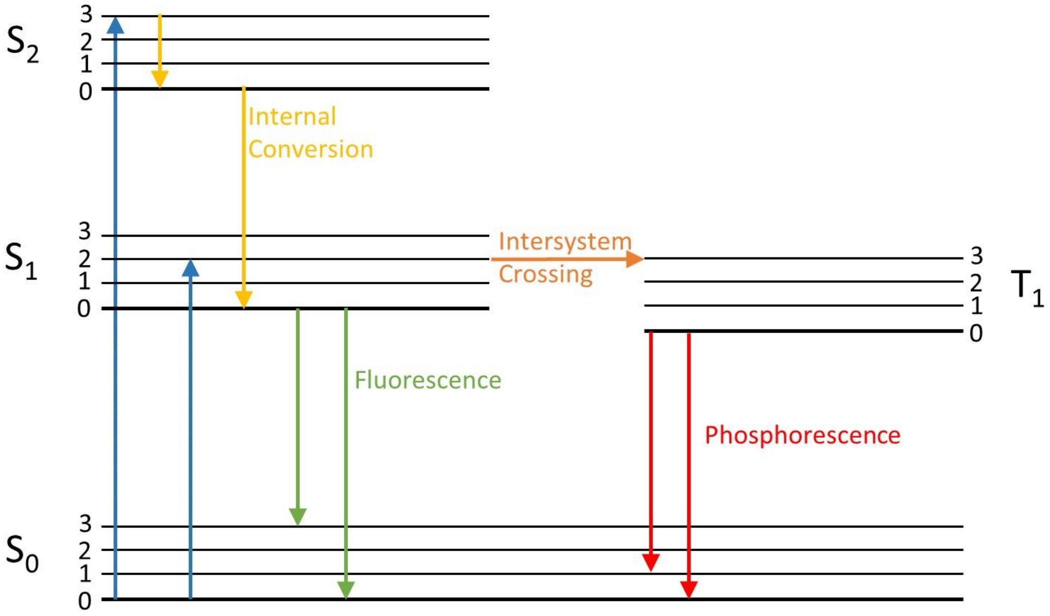

Figure 1: Schematic Jablonski diagram, illustrating the absorption and emission processes of a fluorophore. The absorption (blue arrow) takes place from the ground state $S_{0,0}$ into an electronically excited state ($S_{1,x}$, $S_{2,x}$) with a respective vibrational state x = 0, 1, 2, …. Via internal conversion (yellow arrow), the lowest vibrational state in the excited state $S_{1,0}$ is reached. From there the molecule can emit a photon to reach the ground state (green arrow). This process is called fluorescence. Another pathway is to enter the triplet state $T_{1,x}$ by an intersystem crossing (orange arrow). Emitted photons from this state are called phosphorescence (red arrow).

Figure 1 shows schematically the electronic states ($S_{0,x}$, $S_{1,x}$, …) with their respective vibrational states (x = 0, 1, 2, …). Generally, fluorophores are excited into a higher vibrational state after absorption of a photon with suitable energy. Through a relaxation process, the so-called internal conversion (~ 10^{-12} s), the lowest vibrational state of the excited state is reached. From here, the molecule has different possibilities first it can reach the ground state $S_{0,x}$, through emitting photons. The process of emitting photons from a singlet state is called fluorescence. Another pathway is that the excited molecule can undergo a spin conversion called intersystem crossing and the molecule enter the triplet state $T_{1,x}$. The process of emitting photons from a triplet state is called phosphorescence. The time the molecule stays in the $S_{1,0}$ without undergoing an intersystem crossing or emitting a photon is defined as fluorescence lifetime τ. In general, the fluorescence lifetime is around 10 ns.[54] The lifetime of triplet states is typically around 10^{-3} s to 1 s[54], due to a spin-forbidden transition from singlet to triplet state and vice versa. The fluorescence lifetime can be influenced by the environment, for example by the solvent, polarity, or viscosity. Besides environmental influences on the fluorescence lifetime, molecules can influence the fluorescence lifetime of a fluorophore too. Molecules which influence directly the lifetime of a fluorophore are called quencher molecules.

Fluorescent dyes are commercially available on the market, with emission wavelengths reaching from 350 nm up to 800 nm.[56] Common fluorescent dyes for fluorescence correlation spectroscopy (FCS) and fluorescence microscopy are sold under the names Alexa Fluor, Atto Fluor, Rhodamine dyes, and Cyanine dyes to name a few. Common for these dye classes is a large conjugated double bond system with aromatic rings. These conjugated systems can be functionalized to optimize the absorption and emission spectra of the dyes. Besides the commonly used fluorescent dyes like Alexa Fluor and Atto Fluor dyes, another class of dyes will be presented in the next section.

2.2. Fluorescent Molecular Rotors

Fluorescent molecular rotors can undergo a twisted intramolecular charge transfer (TICT) after excitation.[57, 58] Typically structural motifs for molecular rotors are the linking of an electron-donating group and electron-accepting group through a sigma bond. The absorption of a photon leads to a charge transfer between the electron donor group and the electron acceptor group. Electrostatic forces arise through the charge transfer process in the planar ground state. The molecular rotor can reduce these electrostatic forces by undergoing a twisting around the bridging sigma bond to enter a twisted state. From there two relaxation processes are available for the molecular rotor to reach the ground state: the molecular rotor can emit a photon (Figure 2) or reach the ground state through a non-radiative process.[57] These processes are influenced by the environment because the intramolecular rotation is vigorously influenced by the local viscosity. In a high viscosity environment, the rotational motion is hindered and therefore a stronger fluorescence activity can be observed because the high viscosity prevents the relaxation through the non-radiative pathway from the TICT state. Under these circumstances, the Jablonski diagram presented in Figure 1 can be modified to describe the situation for fluorescent molecular rotors (Figure 2).

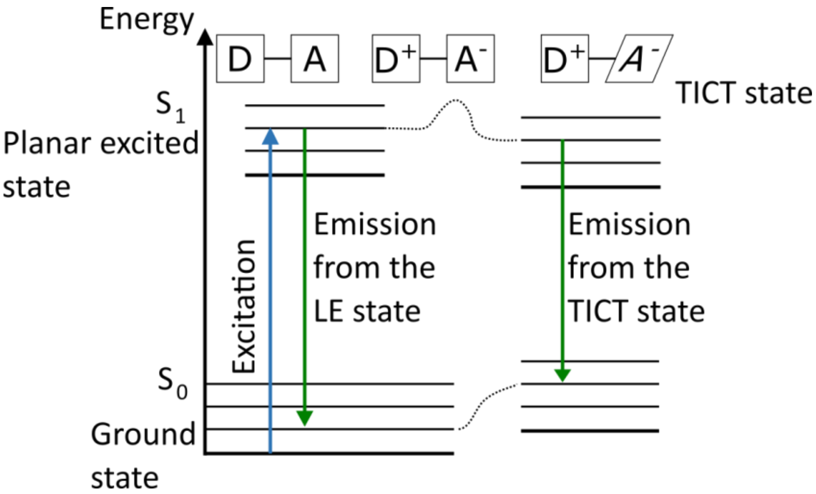

Figure 2: Modified Jablonski diagram for a fluorescent molecular rotor. Presented is the radiative pathway for the molecular rotor. In the ground state, the donor (D) and the acceptor (A) are in a planar conformation. After excitation, charge separation occurs, which could lead to the formation of the TICT state to reduce occurring electrostatic forces. The TICT state possesses lower energy in the excited state, but higher energy in the ground state. The molecule could relax to the ground state by either emitting a photon from the locally excited state or the TICT state.

Besides the viscosity, other factors can influence the fluorescence behavior of the molecular rotor. Solvent polarity, pH, or hydrogen bonds can stabilize or destabilize the excited state and influence the rate between the non-radiative and radiative relaxation pathways. Nonetheless, the viscosity possesses the largest influence on the formation of the TICT state and its relaxation processes.[57, 58]

Typical representatives for molecular rotors are shown in Figure 3A-C. Illustrated are the 9-(dicyanovinyl) julolidine (Figure 3A), *p*-(dimethylamino) stilbazolium (Figure 3B), and 1,4-dimethylamino benzonitrile (Figure 3C). In Figure 3D the molecular rotor AzeNaph1 is shown, which was used as a tailored fluorescent molecular rotor to probe the formation process of nanoparticles described in Chapter 3.

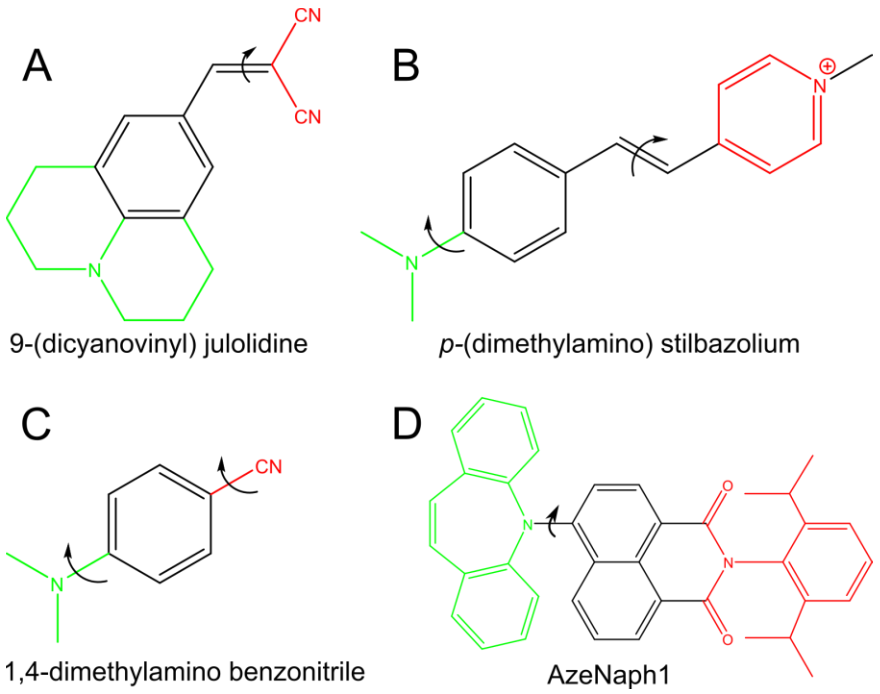

Figure 3: Overview of different types of fluorescent molecular rotors. Donor groups are marked in green, the spacer groups in black, and the acceptor units are marked in red. The arrows indicate the sigma bond around the intramolecular rotation takes place. A) 9-(dicyanovinyl) julolidine, B) *p*-(dimethylamino) stilbazolium, C) 1,4-dimethylamino benzonitrile, D) AzeNaph1.

Fluorescent molecular rotors can be utilized for monitoring the formation of micelles[59], tracking polymerizations[60], or observing conformational changes from proteins.[20, 61] Further, they can be utilized as probes for detecting the local viscosity or as sensors for organic vapor.[62-64] Fluorescent molecular rotors are also applied in biological research fields like probing the viscosity inside cells[65] or cell membrane imaging.[66, 67]

The fluorescent molecular rotor used in chapter 3 is shown in Figure 3D. The electron-rich dibenzo[b,f]azepine acts as an electron donor for the electron-poor naphthalene imide unit after absorbing a photon. Both groups are connected through a C-N sigma bond that allows an intramolecular rotation. The change in the fluorescence lifetime of AzeNaph1 is independent of the solvent polarity, therefore the viscosity possesses the main influence on the fluorescence lifetime of the molecular rotor.[59] Therefore, AzeNaph1 is a suitable candidate to track the viscosity changes inside the emulsion droplets during the SEED and MEP and can monitor the formation process of the nanoparticle. The technique used to record the fluorescence lifetime is presented in the following section.

2.3. Time-Correlated Single-Photon Counting

Time-resolved measurement techniques are powerful techniques to characterize different systems in all-natural science disciplines. The fluorescence decay of a fluorophore is the most direct parameter which gives insights into the interaction of the fluorophore with its direct environment.[64, 68] Technically time-correlated single-photon counting (TCSPC) experiments are realized by shooting repeatedly a short laser pulse on fluorescent molecules. The emitted photons are detected and counted (Figure 4A). Hereby, the short laser pulses function as a start signal, from there on the time is recorded until a photon is detected by the detector. This cycle is repeated many times to count the arriving photons. The arriving photons are then sorted into a histogram depending on their arrival time or a specific time range (bin) (Figure 4B and C).

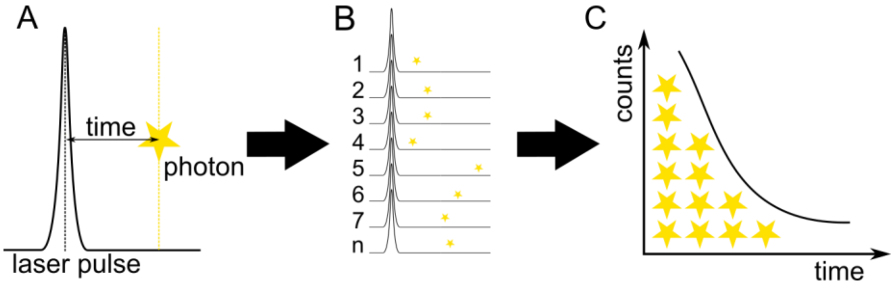

Figure 4: Principle of a TCSPC measurement. A) Repetitive excitation of a fluorophore by short laser pulses. The time is measured between every laser pulse and the respective first arriving photon. B) Step A) is repeated many times to count the number of arriving photons. C) Sorting of the photons into a histogram either by their respective arrival time or by a specific time range.

To analyze the obtained data from the measurements the intensity I can be plotted against the arrival time from the photons t. If the population of the excited states is homogeneous, the recorded decay can be described with a single exponential expression. The fluorescence lifetime τ of the sample can be then determined by the slope of the curve (equation 1).[54]

$$I_{\mathrm{t}} = I_0 \cdot e^{-\frac{t}{\tau}} \qquad \text{equation 1}$$

If the measured sample possesses two or more different fluorescence lifetimes the decay curve is the sum of two or more decay curves (equation 2). These decay curves can be fitted with the following analytical expression:

$$I_{\mathrm{t}} = \sum_{i=1}^{n} A_{\mathrm{i}} \cdot e^{-\frac{t}{\tau_{\mathrm{i}}}} \qquad \text{equation 2}$$

In equation 2 the amplitude is represented by A_{i} to account for the different fractions of the fluorescence lifetime. In a system with more than one fluorescence lifetime, a weighted average fluorescence lifetime τ_{Av} can be defined (equation 3). This fluorescence lifetime takes the single lifetime's τ_{i} and their respective amplitudes A_{i} into account.

$$\tau_{\mathrm{Av}} = \frac{\sum_{i=1}^{n} A_{\mathrm{i}} \cdot \tau_{\mathrm{i}}}{\sum_{i=1}^{n} A_{\mathrm{i}}} \qquad \text{equation 3}$$

The timing precision of a TCSPC experiment is described by the so-called instrument response function. Different aspect influences the IRF, e.g. the pulse shape, the characteristics of the electronics, and the detector.[69] In an optimal system the instrument response function is infinitely narrow, due to an infinitely narrow excitation pulse and accurate electronics and detector. Every deviation from the ideal systems leads to a broadening of the IRF and therefore to a timing imprecision of the TCSPC experiment.

2.4. Fluorescence Correlation Spectroscopy

FCS was first introduced by Magde, Elson, and Webb in the 1970s.[70] Over the past decades, FCS became more and more interesting for researchers in physical chemistry and biophysics. The wide applicability of FCS allows the studying of fluorescent species in different solvents, e.g. aqueous solution[36, 71, 72], biofluids[52, 72-75], or cells.[76, 77] Samples can be characterized regarding size, concentration, fluorescence brightness, and stability.

The differentiation of FCS from other conventional fluorescence-based spectroscopy studies is the principle of investigation of small statistical fluctuations of the light intensity of fluorophores.[55] The statistical intensity fluctuations arise from the Brownian motion of the fluorophores through a very small observation volume. These intensity fluctuations are then analyzed by an autocorrelation function. The fitting of the autocorrelation function can provide information regarding the diffusion coefficients, aggregation behavior, and chemical reactions.[19, 36, 78, 79] Due to the small observation volume (~ 1 µm^3) FCS is very sensitive, even capable to detect a single fluorescent molecule. Advantageous of FCS is, that only fluorescent molecules or labeled molecules are detected.

In Figure 5 a schematic FCS setup and the data procession are shown. In the schematic in Figure 5A, the excitation laser beam is reflected by a dichroic mirror into the objective. The objective focuses the light into the sample. The fluorescent molecules which are diffusing through the observation volume become excited and emit light. The fluorescence light is collected by the same objective and directed to the dichroic mirror. Due to a bathochromic shift, the fluorescence light can pass the dichroic mirror and is focused on a pinhole. The pinhole blocks all light, which is not generated from the focal plane. After passing the pinhole the light reaches the detector. The detected intensity fluctuations (Figure 5B) can be correlated with an autocorrelation function to obtain the autocorrelation curve (Figure 5C).

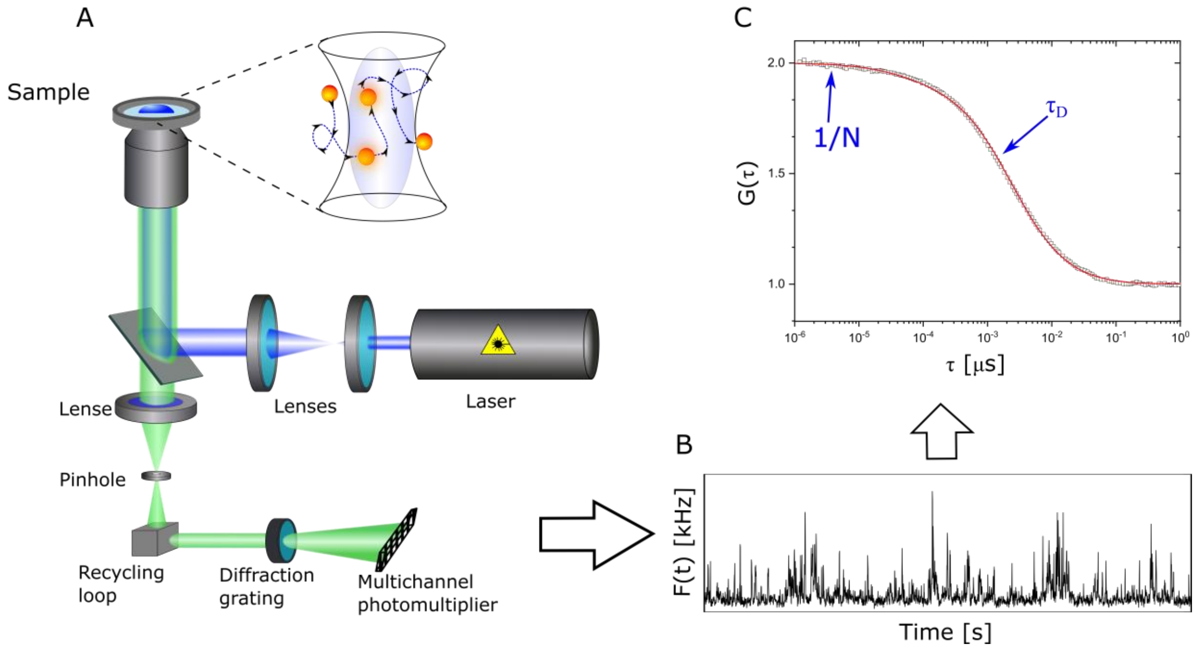

Figure 5: Schematic FCS setup overview with data procession. A) Schematic beam path for a confocal FCS setup. B) Typical recorded intensity pattern during an FCS experiment. C) Normalized autocorrelation function derived from the intensity pattern of B). In red is shown the fitting of the autocorrelation function. Further, the diffusion time and the average number of particles are marked in blue in the graph. Reprinted and adapted from Biomacromolecules 2019, 20, 3786−3797; https://doi.org/10.1021/acs.biomac.9b00868. Copyright 2019 American Chemical Society.

The observation volume V_{obs} possess a Gaussian profile and can be described with the following equation.[55]

$$V_{\text{obs}} = \pi^{\frac{3}{2}} \cdot r_0^2 \cdot z_0 \qquad \text{equation 4}$$

Here, r_0 represents the radial and z_0 the axial dimensions. The diffusion of the fluorescent molecules through V_{obs} causes intensity fluctuations, which fluctuate around a temporal average. The fluorescence intensity signal $F(t)$ can be described as:

$$F(t) = \langle F(t) \rangle + \delta F(t) \qquad \text{equation 5}$$

Here, $\langle \dots \rangle$ denotes to the time average. The intensity signal at a time point t can be autocorrelated with a delay time τ to obtain the normalized fluctuation autocorrelation function $G(\tau)$.

$$G(\tau) = \frac{\langle \delta F(t) \cdot \delta F(t+\tau) \rangle}{\langle F(t) \rangle^2} \qquad \text{equation 6}$$

For fitting the autocorrelation function with an analytical expression, the observation volume is approximated by a Gaussian function described in equation 4. Through the analytical fitting of the autocorrelation function parameters like the diffusion coefficient D or the concentration c can be obtained. If the fluorescence arises only from one type of molecule, which is significantly smaller than V_{obs} and the molecules can diffuse freely in three dimensions the analytic equation can be formulated as followed:

$$G(\tau) = 1 + \frac{1}{N} \frac{1}{\left(1 + \frac{\tau}{\tau_{\text{D}}}\right)} \frac{1}{\sqrt{1 + \frac{\tau}{S^2 \tau_{\text{D}}}}} \qquad \text{equation 7}$$

Here, N denotes the average number of molecules in V_{obs} and S the structural parameter, which is the quotients of z_0 and r_0, and τ_{D} is the diffusion time. If the fluorescence originates from more than one specie the autocorrelation curve is a sum of the different species and can be expressed as followed:

$$G(\tau) = 1 + \frac{1}{N} \sum_{i=1}^{m} \frac{f_i}{\left(1 + \frac{\tau}{\tau_{\text{D,i}}}\right)} \frac{f_i}{\sqrt{1 + \frac{\tau}{S^2 \tau_{\text{D,i}}}}} \qquad \text{equation 8}$$

Here f_{i} denotes the fraction of the i-th species and $\tau_{\text{D, i}}$ is the respective diffusion time of the i-th component. If the fluorophores show significant triplet contributions an additional term needs to be introduced to equation 8. In the newly introduced term, f_{T} is the triplet fraction and τ_{T} is the decay time of the triplet state (equation 9).

$$G(\tau) = 1 + \left[1 + \frac{f_T}{1 - f_T} e^{-\tau/\tau_T}\right] \frac{1}{N} \sum_{i=1}^{m} \frac{f_i}{\left(1 + \frac{\tau}{\tau_{\text{D,i}}}\right)} \frac{f_i}{\sqrt{1 + \frac{\tau}{S^2 \tau_{\text{D,i}}}}} \qquad \text{equation 9}$$

The diffusion coefficient D of the i-th species can be calculated with the diffusion time $\tau_{\text{D, i}}$ and the width of the observation volume r_0.

$$D = \frac{r_0^2}{4\tau_{\text{D}}} \qquad \text{equation 10}$$

With the diffusion coefficient, the hydrodynamic radius R_{H} can be calculated using the Stokes-Einstein equation 11. In equation 11, k_{B} is the Boltzmann constant, T the temperature, and η the viscosity of the solvent.[55, 78]

$$R_{\text{H}} = \frac{k_{\text{B}} T}{6\pi\eta D} \qquad \text{equation 11}$$

3. Chapter: Monitoring the Formation of Polymer Nanoparticles with Fluorescent Molecular Rotors[1]

Due to their unique properties polymeric nanoparticles (PNPs) have attracted considerable interest over the past decades. The term polymeric nanoparticle referred to any type of nanoparticle derived from polymers. The most common approach to synthesizing PNPs is based on using emulsion droplets as templates including solvent evaporation from emulsion droplets (SEED) and miniemulsion polymerization (MEP). Despite a vast research effort, a complete understanding of the transition from the initial liquid droplet to the final particle dispersion is still missing. A major reason is the lack of experimental techniques for probing the transition directly inside the nanoparticle.

Therefore, this chapter presents an experimental approach that uses molecular rotors as fluorescent reporters and combines time-correlated single-photon counting (TCSPC) and fluorescence correlation spectroscopy (FCS) to follow the change in the inner structure of nanoparticles and simultaneously track the size evolution of the nanoparticles. The aforementioned synthesis approach, SEED, and MEP will be investigated and are discussed in sections 3.1.1 and 3.1.2. Section 3.3.1 will then present the fluorescence behavior of the molecular rotor AzeNaph1. The formation process of PNPs during the SEED and the MEP reaction will be presented in section 3.3.3 and section 3.3.5, respectively.

---

[1] This chapter “Monitoring the formation of polymer nanoparticles with fluorescent molecular rotors” is based on a manuscript which is still in preparation.

3.1. Introduction

3.1.1. Solvent Evaporation from Emulsion Droplets

The SEED process was first proposed in the early 1980s by Gurny et al.[80] to produce poly(lactide) nanoparticles. As the first step water containing a surfactant was mixed with an organic phase, containing a pre-synthesized polymer (Figure 6). This macroemulsion was then emulsified by e.g. high pressure or ultrasonication, creating a miniemulsion. This miniemulsion is then heated to start the evaporation process. Creating nanoparticles using the SEED method has some major advantages such as the absence of toxic residual monomers, unreacted agents, or catalysts.[12]

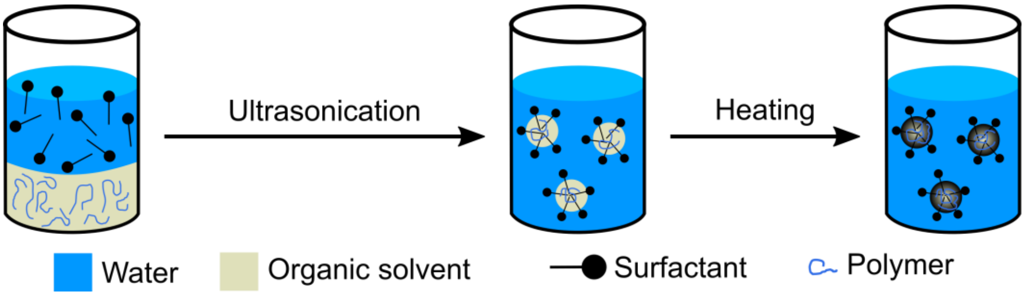

Figure 6: Schematic overview of the SEED process. The first step is creating a macroemulsion by stirring a water phase, containing a surfactant, and an organic phase. The organic phase contains the fluorescent probe and the pre-synthesized polymer. The macroemulsion is then ultrasonicated to create a miniemulsion. By heating the obtained miniemulsion the evaporation process is started.

The size of the particle can be well controlled through the emulsification process. By varying the power and time of sonication, surfactant concentration, or oil/water ratio the size of the particles can be controlled.[42, 81] In 2003 Desgouilles and co-workers[82] conducted zeta potential measurement during the SEED process to observe if every nanodroplet forms one nanoparticle in the final particle dispersion. The zeta potential measurements remain unchanged during the SEED process. Therefore, the authors concluded that no size increase occur during the formation process. This observation was further investigated in 2013 by Staff et al.[39]. The authors observed with fluorescence cross-correlation spectroscopy which role coalescence plays in the final size distribution. The authors found no evidence for coalescence during their fluorescence cross-correlation spectroscopy experiments and concluded that coalescence plays only a minor role. Another study focused on the evaporation kinetics of the dispersed phase. Wang and Schwendeman[83] observed the evaporation of different organic solvents during the

SEED process. They demonstrated that the mass transport of the organic solvent through the continuous phase depends on the properties of the solvent. Here, the diffusion coefficient of the organic solvent and the saturation solubility in the continuous phase plays an important role.[84]

The SEED process can be conducted with different types of polymers including polystyrene, poly(L-lactide), poly(methyl methacrylate), or poly(vinyl acetate) to name a few.[85] Further, SEED is capable of synthesizing complex structures including Janus particles[86, 87] or nanocapsules with a hydrophobic liquid core[85, 88].

3.1.2. Miniemulsion Polymerization

The MEP process is conducted in an emulsified system and the steps to produce the miniemulsion are comparable to the preparation for the SEED process described in section 3.1.1. For the MEP reaction the monomer, which functions as the organic phase, is mixed with an initiator and an ultra-hydrophobic reagent to stabilize the miniemulsion against Ostwald-ripening.[89] The organic phase is then mixed with an aqueous SDS phase and stirred for obtaining a macroemulsion. Through an ultrasonication step, a miniemulsion is obtained. By heating the miniemulsion, the polymerization is started through the thermal decomposition of the initiator.

In contrast to conventional emulsion polymerization, the initiation of the polymerization can be influenced by selecting an oil-soluble initiator. In the case of an oil-soluble initiator, the initiation process of polymerization takes place inside the nanodroplets (droplet nucleation). In the case of a water-soluble initiator, which can be added after the ultrasonication process, the radicals are produced in the water phase and delivered to the micelles containing the monomer.[90, 91] The emulsion droplet size can be influenced by the ultrasonication or the concentration of the surfactant[92] and the MEP reaction is capable of polymerizing different monomers e.g. styrene, methyl methacrylate, or acrylonitrile.[40, 89] However, the MEP is not limited to only one monomer. König et al. reported the successful synthesis of polyurethane-block-polystyrene particles through the MEP reaction.[93] In 2009 Guo and co-workers reported the copolymerization of ethylene and vinyl acetate.[94] Also the inverse miniemulsion polymerization process is reported in the literature. The inverse MEP was used to produce magnetic nanoparticles by encapsulating nickel inside the nanoparticles[95] and can also be utilized to prepare nanocapsules[96] or nanogels[97].

3.2. Experiments and Materials

3.2.1. Materials

Chloroform (≥ 99.8 %) and toluene (≥ 99.8 %) were purchased from Fisher Scientific. Anhydrous hexadecane and the radical initiator Azobisisobutyronitrile (AIBN, ≥ 98.0 %) were bought from Sigma Aldrich. The solvents chloroform, toluene, and hexadecane were used without further purification. Styrene (≥ 99.5 %) was purchased from Carl Roth and was purified using a column packed with neutral aluminum oxide (Al_2O_3, 50-200 µm, 60 Å, Acros Organics). AIBN and Styrene were stored in a dark and cooled environment. The surfactant sodium dodecyl sulfate (SDS, 99 %) was purchased from Acros Organics. The fluorescent dye Atto425 was bought from ATTO-TEC GmbH (Siegen, Germany). J. Thiel (MPIP-P) provided the polystyrene (PS, $M_w = 60$ kg mol^{-1}). The molecular rotor AzeNaph1 was provided by the group of Roberto Simonutti (Department of Materials Science, University of Milano-Bicocca, Italy) as a $5 \cdot 10^{-4}$ M solution in toluene.

3.2.2. Time-Correlated Single Photon Counting Experiments

A confocal setup was used to record the TCSPC data. A pulsed diode laser (405 nm) from PicoQuant was coupled into a commercially available LSM880 microscope (Carl Zeiss, Jena, Germany). For the coupling, an MBS405 dichroic mirror (Carl Zeiss, Jena, Germany) was used. A Zeiss C-Apochromat 40×/1.2 W water immersion objective was used for focusing the light into the sample. The emitted fluorescence light was collected with the same objective, passed through a pinhole, a band-pass filter EM525/50 (Chroma Technology, Vermont, USA), and was detected by a PDM SPAD (Micro Photon Devices, Bolzano, Italy). The recorded data were processed using a TimeHarp 260 (PicoQuant, Berlin, Germany). As a sample holder, an eight-well polystyrene chambered cover glass (Laboratory-Tek, Nalge Nunc International) was used for aqueous samples. For organic and dry samples an Attofluor™ cell chamber (Invitrogen, Paisley, UK) was used. If not otherwise stated, the focus of the laser beam was positioned 20 µm deep into the sample above the glass surface. The recorded TCSPC data were analyzed using the PicoQuant SymPhoTime 64 software. With the same software, the instrument response function was reconstructed by directly evaluating the onset of the decay.

All TCSPC experiments were conducted with 250 µL of the undiluted sample in a Nunc chamber at room temperature. 250 µL sample volume was used to slow down evaporation of the discontinuous phase during the SEED reaction. The measurement duration for one measurement was set to 180 s with a laser current of 80 % and a pulse rate of 20 MHz. An OD (optical density) filter was used to adjust the intensity of the excitation light. The decay curves were fitted using equation 2 with either $n = 1$ or $n = 2$.

3.2.3. Fluorescence Correlation Spectroscopy

Fluorescence correlation spectroscopy measurements were conducted on the same setup described for TCSPC. The emitted fluorescence light was detected by a 32-channel GaAsP photomultiplier, after passing the pinhole and spectrally separated by a diffraction grating. The detection band width was set to 500-553 nm to match the same spectral range as for the TCSPC experiments. Calibration of the observation volume for FCS experiments was done using Atto425 as a reference dye ($D = 438\ \mu m^2\ s^{-1}$ in water at 25 °C)[98]. The observation volume was positioned 20 µm deep in the sample (above the glass surface). The obtained FCS data were analyzed by the ZEN software (Carl Zeiss, Jena, Germany) using the analytical expression in equation 8.

FCS experiments during the SEED process were conducted with 250 µL in a Nunc chamber at room temperature. A typical measurement duration for FCS was recording the intensity fluctuations for 200 s (20 x 10 s). The samples were used without further dilution. The laser current was set to 80 % in continuous wave mode and the count rate was adjusted using optical density filters. The FCS data were analyzed with the analytical equation described with equation 8 ($m = 1$ or 2). Hydrodynamic radii were calculated using equation 11 with the obtained diffusion time.

The samples for FCS experiments during the MEP reaction were diluted with water to adjust the concentration. FCS measurements were conducted with 200 µL using a Nunc chamber as a sample holder. All samples were measured for 200 s (20 x 10 s) with a laser current of 80 % in continuous wave mode. The count rate was adjusted using optical density filters. The recorded data were analyzed using equation 8 with either $m = 1$ or $m = 2$. Hydrodynamic radii were calculated using equation 11 with the obtained diffusion time.

3.2.4. Synthesis of Nanoparticles using the Solvent Evaporation from Emulsion Droplets with Toluene

For the SEED reaction pre-synthesized PS (50 mg, $M = 60$ kg mol^{-1}) was dissolved in 1.44 mL toluene containing the molecular rotor AzeNaph1 ($c = 5 \cdot 10^{-6}$ M). A water phase containing the surfactant SDS (20 g, $c = 1$ g L^{-1}) was added to the organic phase and stirred at room temperature for 1 h at 500 rpm in a closed vessel creating a macroemulsion. After the stirring, the macroemulsion was ultrasonicated (Branson Digital Sonifier W450-D) with a ½-inch tip, for 120 s and 90 % amplitude under ice-cooling. The obtained miniemulsion was transferred to a 50 mL round flask and stirred for 6 h at 500 rpm at 40 °C. 250 µL samples were taken at specific time intervals and directly ice-cooled to stop the evaporation of the toluene.

3.2.5. Synthesis of Nanoparticles using the Solvent Evaporation from Emulsion Droplets with Chloroform

Pre-synthesized PS (50 mg, $M = 60$ kg mol^{-1}) was dissolved in 0.84 mL chloroform containing the molecular rotor AzeNaph1 ($c = 5 \cdot 10^{-6}$ M). A water phase containing the surfactant SDS (20 g, $c = 1$ g L^{-1}) was added to the organic phase and stirred at room temperature for 1 h at 500 rpm in a closed vessel creating a macroemulsion. After the stirring, the macroemulsion was ultrasonicated (Branson Digital Sonifier W450-D) with a ½-inch tip, for 120 s and 90 % amplitude under ice-cooling. The obtained miniemulsion was transferred to a 50 mL round flask and stirred for 6 h at 500 rpm at 40 °C. 250 µL samples were taken at specific time intervals and directly ice-cooled to stop the evaporation of the chloroform.

3.2.6. Synthesis of Nanoparticles using the Miniemulsion Polymerization

6 g Styrene containing the molecular rotor ($c = 10^{-6}$ M) was mixed with 300 mg hexadecane and 100 mg of AIBN. To the organic phase, 24 g of an aqueous SDS solution ($c = 3$ mg L^{-1}) was added and stirred for 1 h at room temperature to create a macroemulsion. After the stirring, the macroemulsion was ultrasonicated (Branson Digital Sonifier W450-D) with a ½-inch tip, for 120 s and 90 % amplitude under ice-cooling. The obtained miniemulsion was transferred to

a 100 mL round flask and was stirred at 500 rpm at 72 °C for 12 h. At specific time intervals, 250 µL samples were taken and quenched by ice-cooling.

3.2.7. Preparation of AzeNaph1 in Solutions of Polystyrene in Toluene or Styrene

PS (M = 60 kg mol^{-1}) fractions reaching from 10 wt% to 50 wt% were dissolved independently in toluene or styrene containing the molecular rotor (c = 10^{-6} M). The solution was stirred for one day before the TCSPC measurement. Solution with a polystyrene fraction upwards of 50 wt%, viscosity was too high to obtain a homogenous solution through stirring. Therefore, samples with higher polymer fractions were obtained by removing toluene or styrene from a 50 wt% sample. The evaporation of the toluene or styrene was accomplished by drying the sample in an oven at 70 °C. The actual polystyrene fraction was then calculated by weight loss. By repeating this process, samples with a polymer content up to 95 wt% could be obtained. Samples were measured in an Attofluor™ cell chamber at room temperature and the recorded decay curves were fitted with equation 2 (n = 2).

3.2.8. Preparing Solutions of Chloroform, Styrene, and Hexadecane Containing AzeNaph1

50 µL of toluene containing the molecular rotor AzeNaph1 (c = 10^{-4} M) was dried and re-dissolved in chloroform, styrene, or hexadecane with the respective amount of solvent. For the TCSPC measurements, the samples were diluted with the respective solvent to a final concentration of AzeNaph1 to c = 10^{-7} M. The measurements were done in an Attofluor™ cell chamber at room temperature and the obtained decay curves were fitted with equation 1.

3.2.9. Preparing Drop-Casted and Spin-Coated Polystyrene Film

Drop-casted PS films were prepared by dissolving 50 mg PS in 200 µL toluene containing the molecular rotor AzeNaph1 (c = 10^{-6} M). The solution was stirred at 300 rpm at room temperature for 2 h. After obtaining a homogenous solution, the solution was deposited on a cover slide and subsequently heated at 80 °C for 24 h.

Spin-coated PS films were prepared by dissolving 15.6 mg PS in 282 µL toluene containing the molecular rotor AzeNaph1 ($c = 10^{-5}$ M). For a film thickness of around 500 nm, 150 µL of the previously prepared solution was spin-coated on a glass slide (30 s at 2000 rpm) and subsequently dried for 24 h under reduced pressure at 80 °C.

3.3. Results and Discussion

3.3.1. Fluorescence Lifetime Measurement in Different Organic Solvents

The tailored fluorescent molecular rotor AzeNaph1 was selected due to its negligible water solubility.[59] Commercially available molecular rotors like BODIPY[99], 9-(dicyanovinyl)-julolidine[100], or thioflavin[101] are mostly designed for an aqueous environment and therefore not suitable to monitor the formation process during the SEED or MEP reaction. Indeed, it was crucial that the molecular rotor possesses a negligible water solubility and is only dissolvable in the organic phase of the emulsion to provide information about the local viscosity inside the nanodroplets. Further, AzeNaph1 offers a high Stokes shift (~ 70 nm), stability, and a fluorescence lifetime that strongly depends on the viscosity and ranges from less than 1 ns in pure organic solvents to 5-8 ns in solid polymer films.[59]

At first, the molecular rotor AzeNaph1 was studied in different organic solvents to gain insights into the fluorescence behavior. Here, only organic solvents were selected with relevance to either the SEED or the MEP reaction. The fluorescence decay curves of AzeNaph1 in toluene, chloroform, hexadecane, styrene, and polystyrene films are shown in Figure 7.

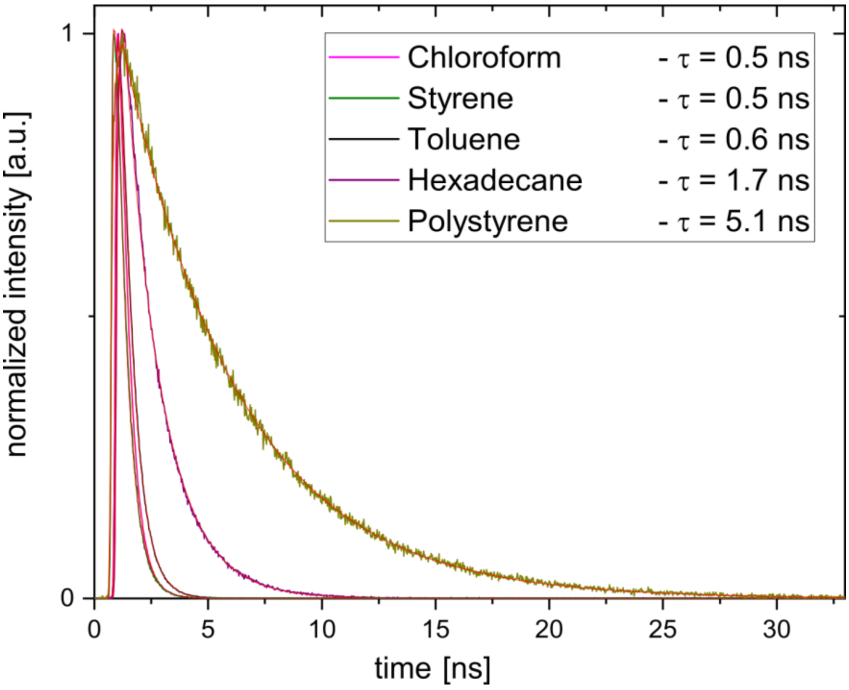

Figure 7: Typical fluorescence decay curves for AzeNaph1 in chloroform (magenta), styrene (green), toluene (black), hexadecane (purple) and polystyrene (dark yellow). The inset provides the obtained lifetimes recorded in the respective solvent.

Toluene and chloroform are the relevant solvents for the SEED reaction (section 3.3.3 and section 3.3.4) and styrene and the osmotic pressure agent hexadecane are relevant for the MEP reaction (section 3.3.5). The illustrated curves in Figure 7 were fitted with a one-component fit using equation 2 ($n = 1$) and the yielded fluorescence lifetimes of AzeNaph1 are shown in the inset in the top right corner. Comparable short lifetimes are observed in toluene, chloroform, and styrene of around $\tau = 0.5$ ns. In comparison, longer lifetimes are observed in hexadecane $\tau = 1.7$ ns and polystyrene film $\tau = 5.1$ ns. The differences in the observed fluorescence lifetime can be attributed to the different viscosities, reaching from chloroform (0.52 cP)[102], toluene (0.52 cP)[102], styrene (0.70 cP)[103], to hexadecane (3.03 cP)[104] with the highest viscosity of the tested organic solvents. The fast decay times were observed in low viscosity environments (chloroform, toluene, and styrene). In these solvents, the internal rotation of AzeNaph1 is not restricted by the viscosity. This results in an unhindered population of the twisted intramolecular charge transfer (TICT) state and consequently leads to short measured lifetimes. Contrary, hexadecane possesses an influence on intramolecular rotation, due to the higher viscosity. Here, the measured lifetime is larger than in the other solvents. Hexadecane is used as an osmotic pressure agent in the MEP reaction, but only at very small volume fractions and therefore possess a negligible influence on the fluorescence lifetime of AzeNaph1.

The final obtained nanoparticles from SEED and MEP are made of PS, and therefore PS films containing AzeNaph1 were prepared. The detected fluorescence lifetime in pure drop-casted polystyrene films is $\tau_{PS} = 5.1$ ns and is around one order of magnitude larger than lifetimes found in toluene, chloroform, or styrene. Since the polystyrene films were produced using the drop-casting method remaining solvent inside the polymer film cannot be excluded, due to the thickness of the polymer film and could not be removed by heat and reduced pressure. To further observe the possibility of entrapped solvent in drop-casted films, polymer films with thicknesses of around 500 to 1500 nm were prepared. But even in the spin-coated films, the fluorescence lifetime of AzeNaph1 remained identical to the previously measured fluorescence lifetimes. Therefore, no further enhancement of the produced polystyrene films by decreasing the thickness could be achieved. Interestingly, the recorded decay curves could be adequately fitted using a one-component fit (equation 2; $n = 1$) indicating that all molecular rotor molecules experience a similar environment possessing similar local viscosities. This finding suggests that the molecular rotors are embedded in a homogeneous environment.

3.3.2. Recording the Fluorescence Lifetime of AzeNaph1 in Polystyrene Containing Toluene or Styrene Solutions

During the SEED and MEP reactions, the molecular rotor AzeNaph1 is embedded in a toluene-polystyrene mixture or styrene-polystyrene mixture, respectively. These mixtures are changing from a low polystyrene percentage in the freshly prepared nanodroplet to a higher polystyrene percentage in the final nanoparticles. Therefore, as a reference, the fluorescence behavior of AzeNaph1 was studied in polymer solutions with well-defined concentrations. Figure 8 illustrates the monitored AzeNaph1 of polystyrene in toluene, whereas the measurements of polystyrene in styrene are shown in Figure 9.

Figure 8A show normalized recorded TCSPC decay curves of AzeNaph1 of polystyrene in toluene. Fitting these curves with equation 2 ($n = 2$) and calculating the average fluorescence lifetime with equation 3 leads to the graph in Figure 8B. With increasing polystyrene fraction, the decay curves in Figure 8A show a clear shift to longer decay times, reflecting the increasing local viscosity of the environment. This trend of the increasing decay times is also reflected in the calculated average fluorescence lifetime shown in Figure 8B. Additionally, in Figure 8B, two further points were added, a brown symbol representing measurements done in pure toluene and a blue symbol for monitoring AzeNaph1 in dry polystyrene films. The additionally shown data points could be fitted with equation 2 ($n = 1$), meaning that all of the rotor molecules are embedded in a similar local environment. The fluorescence lifetime values of AzeNaph1 were yielded to $\tau_{\text{tol}} = 0.6$ ns in toluene and $\tau_{\text{PS}} = 5.1$ ns in dry polystyrene films. Contrary, the fluoresce decay curves measured in the polymer solutions (Figure 8A) required a two-component fit yielding two decay times τ_1 and $\tau_{2,}$ and their respective amplitudes A_1 and A_2 are shown in Figure 8C and D.

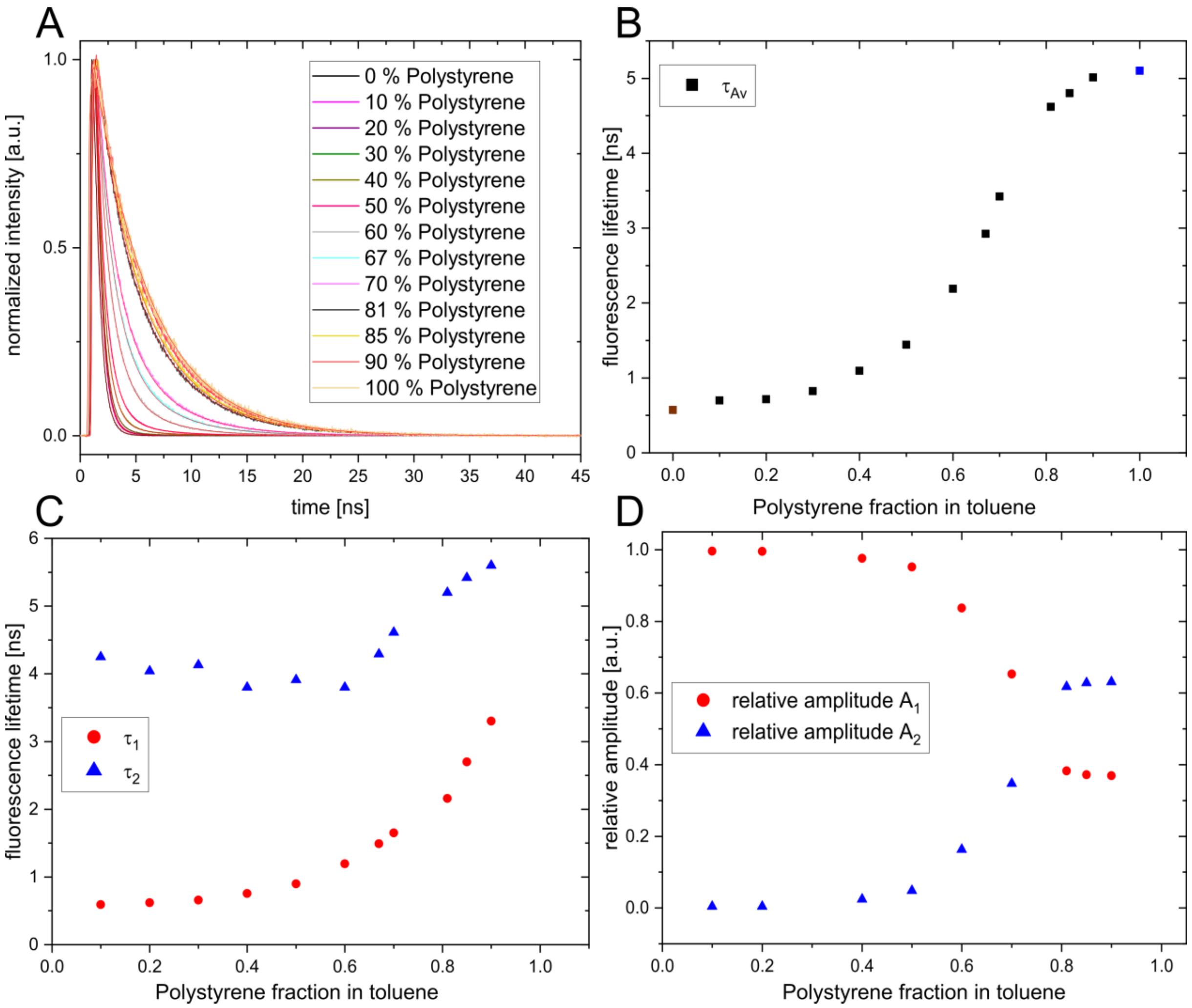

Figure 8: Illustration of the fluorescence behavior of AzeNaph1 in toluene solutions of polystyrene. A) Typical recorded fluorescence decay curves of AzeNaph1 versus the polystyrene concentration with their respective fits. B) Weighted average fluorescence lifetimes calculated with equation 3 of AzeNaph1 versus the polystyrene fraction in toluene. The data point at 0 % polystyrene (brown symbol) was done in pure toluene and the data point at 100 % polystyrene (blue symbol) in a dry polystyrene film. C) Short (red symbols) and long fluorescence lifetime (blue symbols) versus the polystyrene fraction in toluene obtained from the fitted decay curves in A). D) Respective relative amplitudes of the short (red symbols) and long (blue symbols) fluorescence lifetime in C) polystyrene fraction in toluene.

The short fluorescence lifetime τ_1 at low polymer concentration is similar to the fluorescence lifetime measured in pure toluene, whereas the long fluorescence lifetime τ_2 is considerably longer and at higher polymer concentration similar to the one measured in polymer films. This further indicates that during a TCSPC experiment some of the AzeNaph1 molecules are located in toluene-rich environments and other rotor molecules are located in a polymer-rich environment. The fractional amount of AzeNaph1 in the respective environment is indicated by their relative amplitudes shown in Figure 8D. The relative amplitude A_1 is decreasing, while the relative amplitude A_2 is increasing with increasing polystyrene concentration. In contrast, their respective fluorescence lifetime τ_1 and τ_2 are both increasing. This indicates that the local viscosity is increasing in both environments, the polymer-rich environment and also to a lesser extent in the solvent-rich environment. Furthermore, neither the solvent-rich environment nor the polymer-rich environment represents a completely homogeneous environment. A two-component fit is the simplest possible representation of the studied environments. This discrepancy points out the nonhomogeneous nature of the polystyrene in toluene solutions on a length scale of the molecular rotor molecules of around 1 nm. Therefore, τ_1 and τ_2 are hence the average fluorescence lifetime of various lifetimes that the molecular rotor possesses in the solvent-rich and polymer-rich environment.

Similar fluorescence behavior of AzeNaph1 could be observed for recorded decay curves of polystyrene in styrene solution. Figure 9A shows the recorded decay curves of AzeNaph1 of polystyrene in styrene solution, whereas Figure 9B shows the calculated average fluorescence lifetime. In Figure 9B are added two further data points, one at 0 % polystyrene as a brown symbol representing the recorded fluorescence lifetime in pure toluene and at 100 % polystyrene as a blue symbol representing the recorded fluorescence lifetime in dry polystyrene films. The recorded decay curves in Figure 9A are fitted with a two-component fit (equation 2, $n = 2$) yielding a short fluorescence lifetime τ_1 and a long fluorescence lifetime τ_2 and their respective amplitudes A_1 and A_2. These data are shown in Figure 9C and D. The discussion of the recorded fluorescence lifetime of AzeNaph1 in polystyrene containing styrene solution is identical to the previously discussed detected lifetimes of AzeNaph1 in polystyrene containing toluene solution.

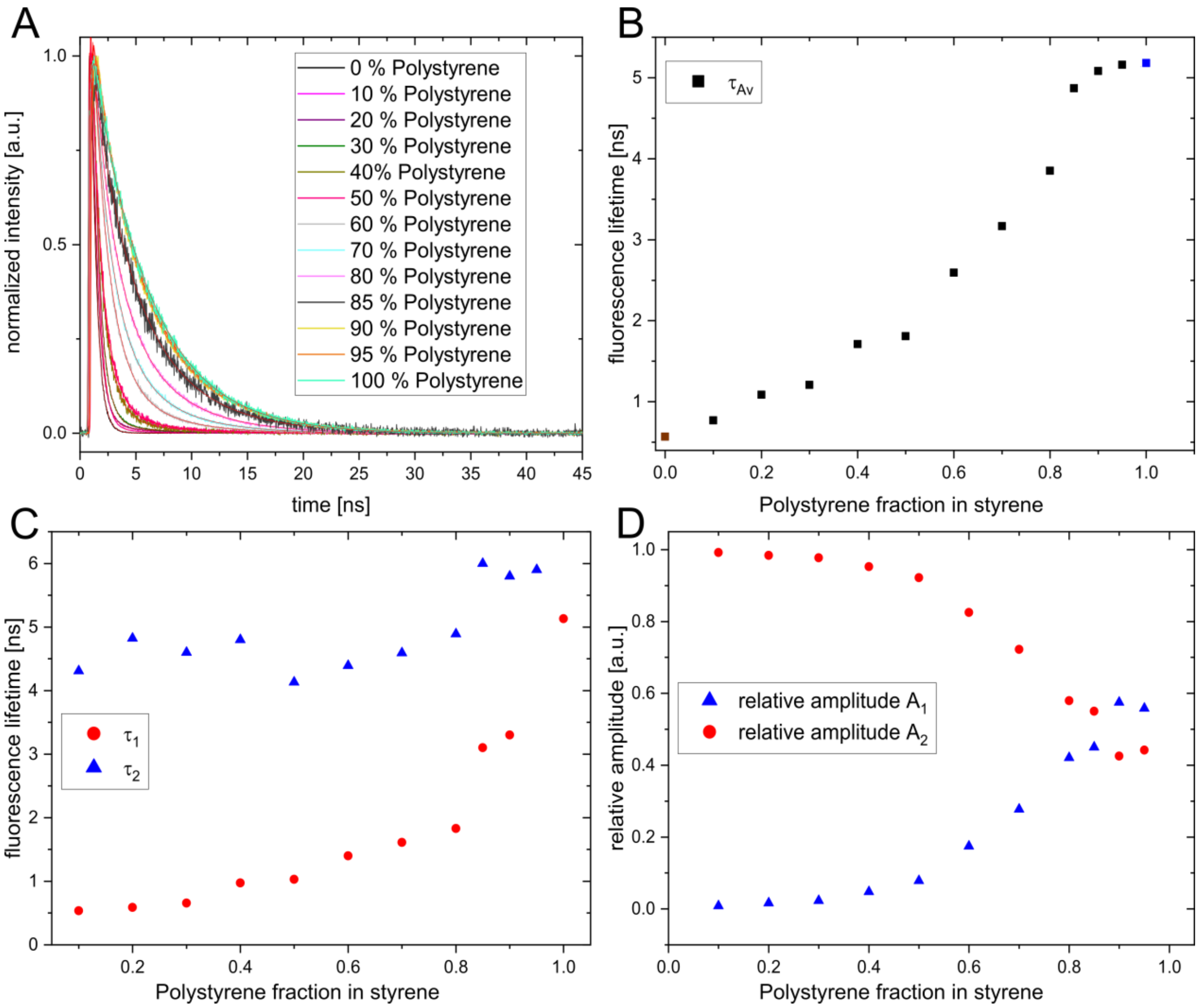

Figure 9: Illustration of the fluorescence behavior of AzeNaph1 in styrene solutions containing polystyrene. A) Typical recorded fluorescence decay curves of AzeNaph1 versus the polystyrene concentration with their respective fits. B) Weighted average fluorescence lifetimes calculated with equation 3 of AzeNaph1 versus the polystyrene fraction in styrene. The data point at 0 % polystyrene (brown symbol) was done in pure toluene and the data point at 100 % polystyrene (blue symbol) in a dry polystyrene film. C) Short (red symbols) and long fluorescence lifetime (blue symbols) obtained from the fitted decay curves in A) versus the polystyrene fraction in styrene. D) Respective relative amplitudes of the short (red symbols) and long (blue symbols) fluorescence lifetime in C) versus the polystyrene fraction in styrene.

3.3.3. Solvent Evaporation from Emulsion Droplets in Toluene

The first process to study was the SEED process. Here, the toluene acts as the organic phase and contains the molecular rotor. The process was carried out as described in section 3.2.4. Small samples (~ 200 µL) were taken at regular time intervals of 0, 1, 2, 2.5, 3, 3.5, 4, 4.5, 5, and 6 h after starting the evaporation process by heating the solution. In Figure 10A the working principle of the combination of TCSPC and FCS is schematically presented. For recording TCSPC decay curves the emitted fluorescence photons of the individual rotor molecules are utilized, whereas for FCS the fluorescence of the whole polystyrene particle is utilized to record the autocorrelation curve. For the TCSPC experiment, the arrival time of the emitted photons from the molecular rotor embedded inside the nanoparticles was recorded to obtain the decay curves shown in Figure 10B. In difference, if the intensity fluctuation of the fluorescence of the whole nanoparticle is recorded (caused by the NP diffusion through the confocal volume) an FCS autocorrelation could be obtained and is shown in Figure 10C.

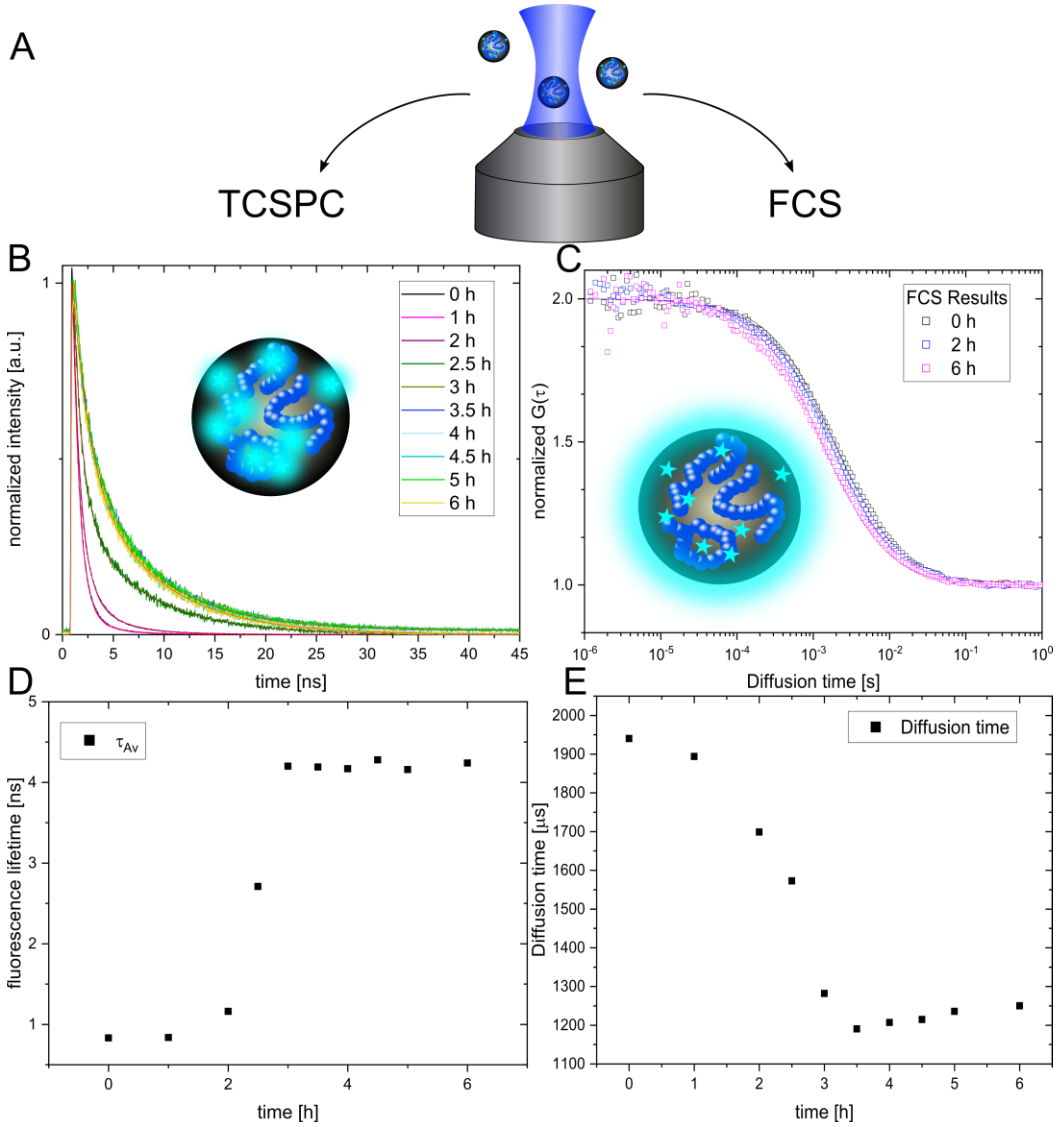

Figure 10: Overview of the recorded data from the SEED reaction with TCSPC and FCS. A) Working principle of the combination of TCSPC and FCS method. The molecular rotor was used as a probe to provide information about the local viscosity from inside the nanodroplets and the size of the polystyrene nanoparticle during the formation process. For TCSPC the fluorescence photons of the individual rotor molecules were utilized to record the TCSPC curves (B), whereas the fluorescence of the whole nanoparticle was utilized to record FCS autocorrelation curves (C). D) Here, the calculated average fluorescence lifetime versus the heating time is presented obtained from the TCSPC curves in B) after fitting these curves with a two-component fit. E) Yielded diffusion times of the polystyrene nanoparticles from the FCS curves in C) versus the heating time.

The decay curves in Figure 10B exhibit a clear shift towards longer decay times. This shift can also be observed in the average fluorescence lifetime shown in Figure 10D. For obtaining the fluorescence lifetime of the molecular rotor the decay curves shown in Figure 10B were fitted with a two-component fit (equation 2) and calculated using equation 3. An increase in the fluorescence lifetime of AzeNaph1 could be observed from $\tau_{\mathrm{Av,\,SEED,\,0h}} = 0.8\ \mathrm{ns}$ to $\tau_{\mathrm{Av,\,SEED,\,6h}} = 4.2\ \mathrm{ns}$ with increasing heating time. This increase originates from advancing evaporation of toluene from the nanodroplets and therefore an increasing polystyrene fraction. The increasing polystyrene fraction leads to an overall increased viscosity in the nanodroplets. Simultaneously, to the recording of the TCSPC decay curves, FCS autocorrelation curves were recorded (Figure 10E). The FCS autocorrelation curves shown in Figure 10E were fitted with equation 8 to yield their corresponding diffusion times. The diffusion times in Figure 10E experienced a decrease with increasing evaporation time. The decrease reflects the shrinkage of the nanodroplets with subsequent evaporation of the toluene from the nanodroplets through the water phase. The smaller nanoparticles possess a faster diffusion and therefore a shorter diffusion time is recorded with FCS.

By combining the results from the TCSPC experiment and FCS measurements a broad picture of the kinetics of the formation process can be obtained. In Figure 11 the evolution of the hydrodynamic radius and the estimated polymer content are illustrated. The hydrodynamic radius was calculated using equation 11 and the diffusion times yielded from the FCS measurement. The polymer content was estimated by comparing the average fluorescence lifetime with the previously presented lifetimes measured for AzeNaph1 in polystyrene containing toluene solutions (see Figure 8).

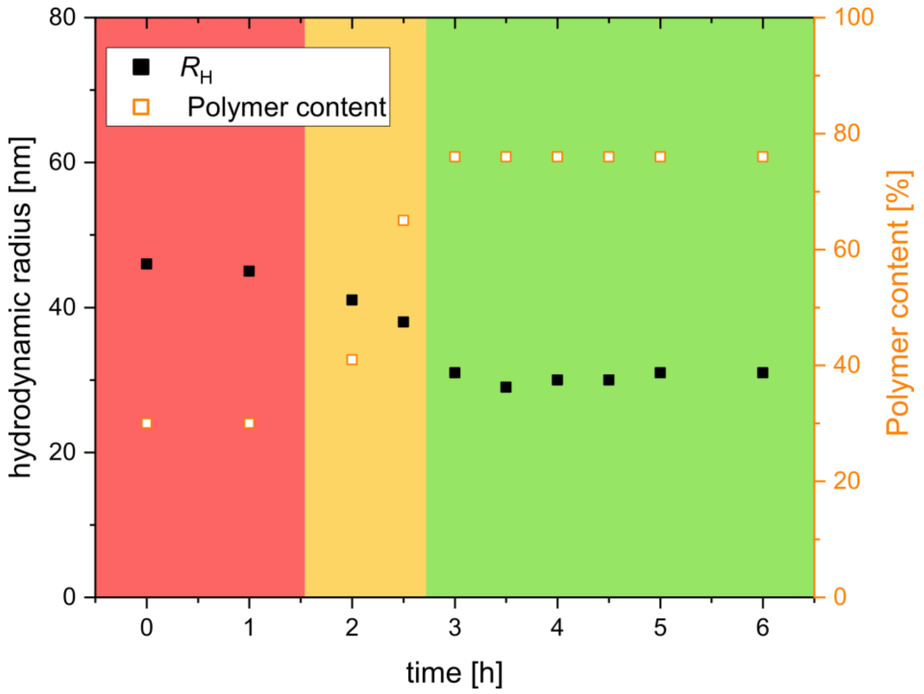

Figure 11: Combination of the results from the TCSPC and FCS experiments. Shown is the dependence of the hydrodynamic radius (black symbols) versus the progressive heating time. Further, the estimated polymer content (hollow orange symbols) versus the heating time is shown. Three stages are marked in the graph: the solution state (red), the gel state (dark yellow), and the glassy state (green).

The formation process of the nanoparticles by the SEED process can be divided into three stages.[12, 105, 106] The first stage is referred to as the "solution stage" (red region in Figure 11). In this state, the polymer content in the nanodroplets is around 20 %, and they possess a hydrodynamic radius of $R_H \approx 46$ nm. Dominant in this stage is a slow evaporation of toluene through the water phase. The plateau is arising from the slow evaporation process and lasts up to 1.5 h. With ongoing evaporation of toluene from the nanodroplet, the second stage, the "gelation stage" is reached (yellow region in Figure 11). This stage can be characterized by a fast evaporation of toluene from the nanodroplets through the continuous water phase. In this stage, the polymer content experienced a fast increase from ~ 20 % to almost 80 %, while the hydrodynamic radius of the particle decreased to around 33 nm. The particles start to stabilize and the polymer chains tend to become entangled. The entanglement concentration of PS with a molar mass of 60 kg mol^{-1} can be estimated to be around 40 %.[107] The third stage, the "glassy state" of the SEED process is reached by further solvent evaporation (green region in Figure 11). The glassy regions are most likely to form in the outer area of the nanoparticles and hinder the remaining solvent diffusion into the continuous phase and evaporating from the reaction system.[12] This results in a slowdown of the evaporation process. The formation of a polymer "skin" in form of the glassy region at the outer regions of the nanoparticles resulting from evaporation of the solvent in a confined geometry was observed in the literature.[108] In the third stage plateaus in the hydrodynamic radius and by the polymer content could be observed. From the slow down or hindrance of the solvent evaporation from the outer glassy regions arises that the polymer content is still at ~ 80 % after 6 h of heating the solution.To gain a more in-depth picture of the SEED process, the short and long lifetime and their respective relative amplitudes of the formation process of the particle during the SEED reaction can be studied. The short and long fluorescence lifetime and their respective amplitudes are shown in Figure 12A and B.

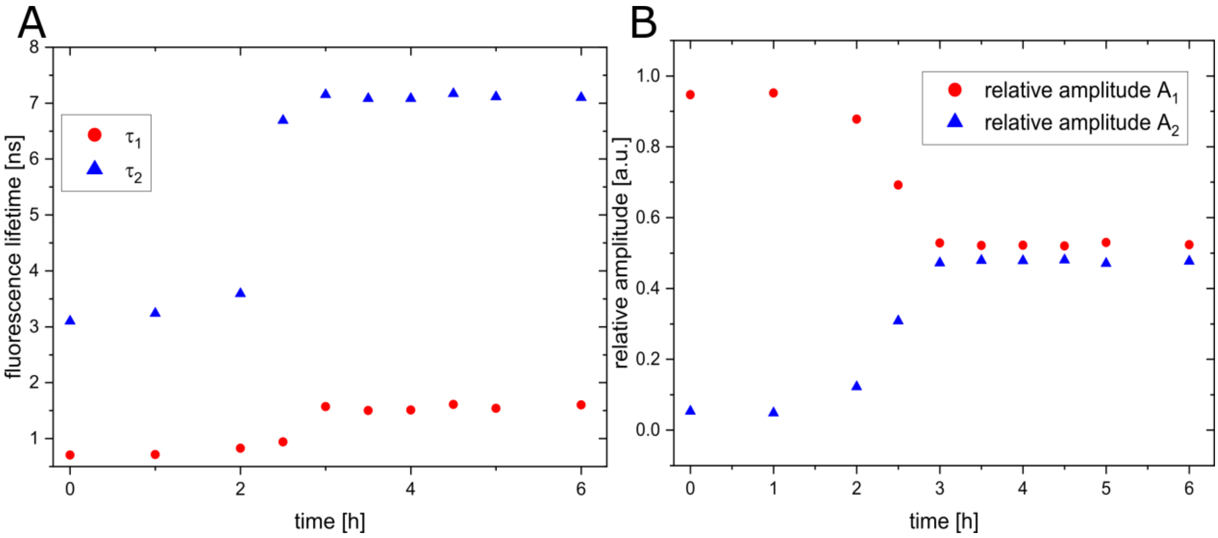

Figure 12: A) Recorded short (red symbols) and long (blue symbols) fluorescence lifetime of AzeNaph1 during the SEED reaction versus the heating time. B) Respective relative amplitudes of the short and long fluorescence lifetime from A) versus the heating time.

The two recorded fluorescence lifetimes of AzeNaph1 arise from two different environments, a solvent-rich environment, and a polymer-rich environment. The molecular rotors located in the solvent-rich environment increase from $\tau_{1,\,0\,\mathrm{h}}$ = 0.7 ns to $\tau_{1,\,6\,\mathrm{h}}$ = 1.6 ns after 6 h of solvent evaporation. The respective relative amplitude decrease in the same time decreases from $A_{1,\,\mathrm{rel}}$ = 95 % to around $A_{1,\,\mathrm{rel}}$ = 52 %. Molecular rotor molecules located in the polymer-rich environment experienced an increase in their fluorescence lifetime from $\tau_{2,\,0\,\mathrm{h}}$ = 3.1 ns to around $\tau_{2,\,6\,\mathrm{h}}$ = 7.1 ns. The respective relative amplitudes are increasing from $A_{2,\,\mathrm{rel}}$ = 5 % to around $A_{2,\,\mathrm{rel}}$ = 48 % in the same time range. The changing of the relative amplitudes and the increase of the fluorescence lifetimes of AzeNaph1 were caused by the continuous solvent evaporation. This leads to an increase in the polymer concentration in the nanodroplets and therefore an increase in the viscosity. During the whole SEED process, two fluorescence lifetimes were observed, even after 6 h of evaporation time. Fluorescence lifetime measurements in bulk polymer solution at a high polymer concentration of the long fluorescence lifetime τ_2 are around 6 ns (compare section 3.3.2 and Figure 8C). Fluorescence lifetime measurements of AzeNaph1 in nanoparticles revealed a long fluorescence lifetime of $\tau_{2,\,6\,\mathrm{h}}$ = 7 ns after 6 h of heating the SEED process. Such values were observed in multiple independently performed experiments. These values can be attributed to the formation of very dense polymer regions in the nanoparticles. These dense regions restrict the intramolecular rotation of the molecular rotor even stronger, than in bulk polystyrene films. In literature, the fluorescence behavior of molecular rotors is often discussed related to available free volume.[109, 110] This free volume can affect the rotational mobility of the molecular rotor. The previously presented fluorescence lifetime data indicate that some of the molecular rotors in polystyrene particles are located in regions with less free volume than in dry polystyrene films. Further, in dry polystyrene films, only one fluorescence lifetime could be observed. This indicates that the molecular rotor is embedded in a homogeneous environment, whereas the molecular rotor in the nanoparticle experienced a non-homogeneous environment leading to two detected fluorescence lifetimes. The relative amplitudes of the final particles suggest that the final particle still consists of around 50 % of a solvent-rich environment, but this value does not provide any information regarding the amount of the remaining solvent inside the nanodroplets. The relative amplitudes are not changing even after heating the SEED solution for 24 hours at 40 °C. The remaining solvent could only be removed by drying the whole solution on a glass slide and an annealing step to dry the nanoparticles at 70 °C for 2 h. Recorded TCSPC decay curves of this film could be fitted with a one-component fit (equation 2, $n = 1$) and are comparable to dry polystyrene films prepared as in section 3.2.9 described. The fluorescence lifetime was yielded to $\tau_{\mathrm{PS\ film}}$ = 5.2 ns. Commonly, the SEED process is carried out with low boiling solvents, e.g. chloroform, dichloromethane, or ethyl acetate.[12] By replacing these solvents with toluene a slowdown of the evaporation process is reached. The slow down of the SEED process was necessary to follow the kinetics of the reaction and prevent the evaporation of the discontinuous phase during the measurements. Nevertheless, SEED experiments with chloroform as solvent were carried out and are presented in the following section.

3.3.4. Solvent Evaporation from Emulsion Droplets in Chloroform

Commonly used solvents for the SEED process are chloroform, dichloromethane, or ethyl acetate[12], therefore chloroform was selected as a further solvent to study the SEED process. Samples (~ 200 µL) were taken after regular time intervals of 0, 10, 25, 30, 40, 45, 50, 60, 70, and 90 min after starting the heating process. To slow down the evaporation of chloroform during TCSPC and FCS measurements, 200 µL was used and the coverage of the sample holder was necessary to slow down the solvent evaporation. The decay curves were fitted with a two-component fit (equation 2; $n = 2$) and are illustrated in Figure 13A. The obtained short and long fluorescence lifetimes were used to calculate τ_{Av} (equation 3) and are presented in Figure 13B. Recording FCS data with chloroform as the discontinuous phase was not possible because undiluted samples were too concentrated, and dilution of the samples led to disruption of the already formed emulsion droplets.

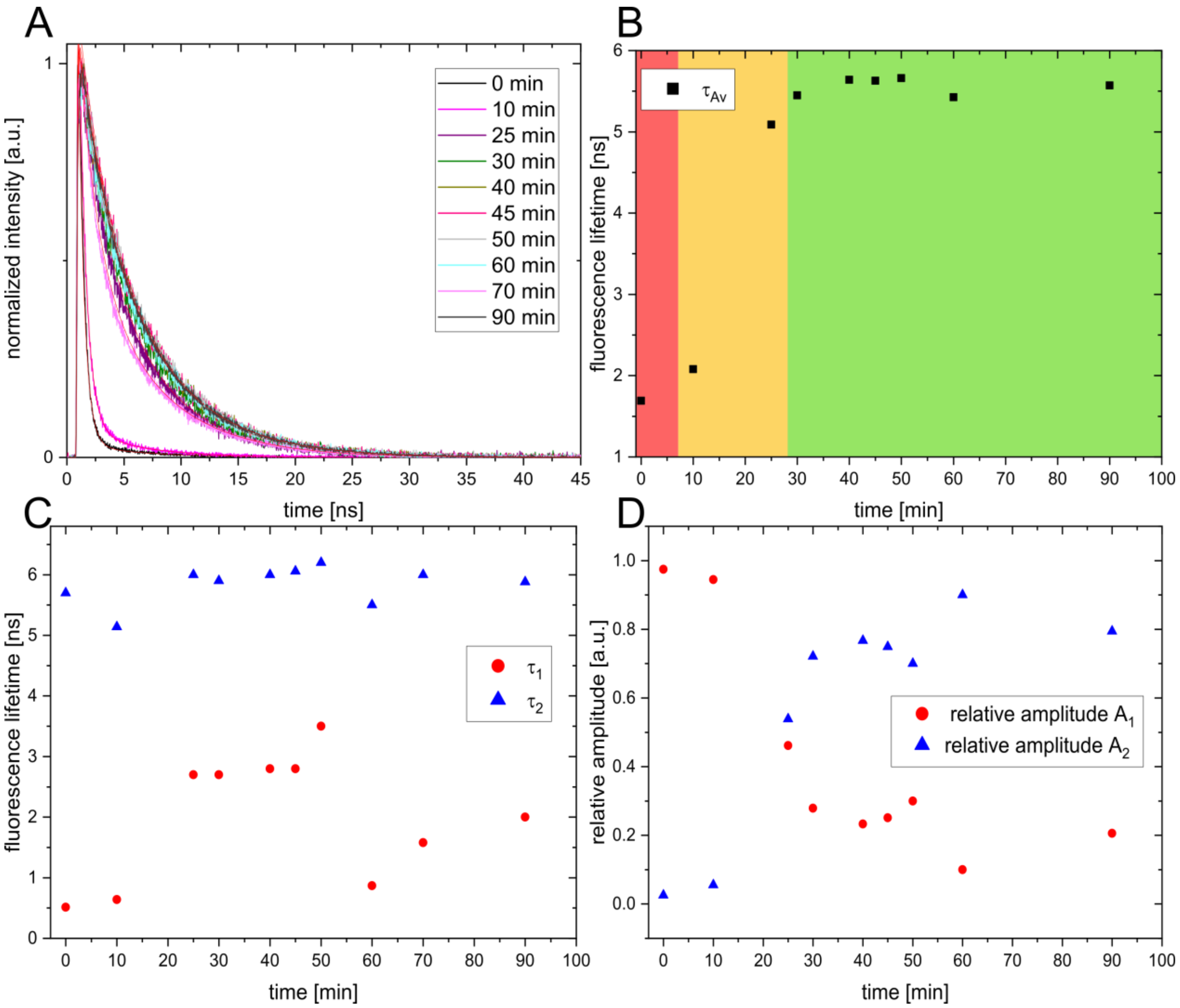

Figure 13: Overview of the SEED process done with Chloroform as the organic phase. A) Recorded decay curves from the SEED reaction with chloroform. The decay curves were fitted using equation 2 ($n = 2$). B) Average fluorescence lifetime versus the heating time. Further, three regions are marked: the solution phase (red), the gel phase (yellow), and the glassy state (green). C) Short (red symbols) and long (blue symbols) fluorescence lifetime versus the heating time. D) Respective relative amplitudes A_1 (red symbols) and A_2 (blue symbols) from the short and long fluorescence lifetime in C) versus the heating time.

The recorded TCSPC curves in Figure 13A show a clear shift observable after 10 min. Upwards 25 min after starting the heating process only slight changes are observable. The calculated average lifetime of AzeNaph1 is changing from $\tau_{0\ \text{min, chloroform}} = 1.7$ ns measured before the heating started to $\tau_{90\text{ min, chloroform}}$ = 5.6 ns after 90 min of heating the miniemulsion. Similar, to the SEED process done with toluene, increase fluorescence lifetimes are detected with proceeding evaporation time. The vanishing solvent leads to a progressively confined environment where the molecular rotor is embedded. This causes a stronger restriction for intramolecular rotation movements and shifts the fluorescence lifetimes to larger values.

Similar to the SEED reaction done with toluene, three phases can be assigned to the SEED process with chloroform. In Figure 13B the red region represents the solution phase, the yellow region displays the gel state and in green is marked the glassy state of the SEED process. In the first stage, the solution state persists from 0 min to ~ 10 min and is much shorter compared to the solution state found for toluene (0 h to 3 h) as an organic solvent. Chloroform possesses a lower boiling point than toluene ($T_{\text{b, chloroform}}$ = 61 °C; $T_{\text{b, toluene}}$ = 110 °C) and evaporates faster. Further, the average lifetime at 0 min, $\tau_{0\text{ min, chloroform}}$ = 1.7 ns, is higher than the lifetime found for the SEED reaction conducted with toluene, $\tau_{0\text{ min, toluene}}$ = 0.8 ns. This arises from two reasons: first, the initial volume of chloroform was smaller compared to toluene. In both experiments, the same mass fraction was used and toluene possesses a lower density than chloroform, more toluene was needed initially. Therefore, the initial nanodroplets possess a higher polymer content than the emulsion droplets in the toluene experiments. Further, evaporation from the emulsion droplets during the stirring to obtain the macroemulsion cannot be excluded. Furthermore, sonification experiments were conducted under ice-cooling, but this does not prevent completely the evaporation of chloroform during the sonication process. With ongoing heating of the SEED reaction, the next phase is reached, the gel phase, which occurs from ~ 10 min to ~ 30 min. In this phase, the evaporation of the chloroform from the reaction solution takes place. During this phase, the fluorescence lifetime of AzeNaph1 is increasing due to an increase in the local viscosity. After ~ 30 min the last stage, the glassy state is reached. In this state, no significant change in the measured fluorescence lifetime of AzeNaph1 is observed, indicating that the SEED process has reached its final state. The average fluorescence lifetime after 90 min is yielded to $\tau_{90\text{ min, chloroform}}$ = 5.6 ns and is higher than the value found for toluene, $\tau_{6\text{ h, toluene}}$ = 4.2 ns, and even the fluorescence lifetime in pure polystyrene films, $\tau_{\text{polystyrene film}}$ = 5.1 ns. The recorded lifetime of 5.6 ns arises from the formation of a polymer "skin" similar to the observed dense polymer region for the SEED process with toluene.

To gain a more in-depth picture of the SEED process with chloroform, the short and long fluorescence lifetime (Figure 13C) and their respective relative amplitudes (Figure 13D) can be studied. The two recorded fluorescence lifetimes arise from two different environments. The short lifetime can be attributed to a solvent-rich environment, whereas the long lifetime originates from a polymer-rich environment. The short lifetime is increasing from $\tau_{1,\,0\,\mathrm{min}}$ = 0.5 ns to $\tau_{1,\,90\,\mathrm{min}}$ = 2.0 ns after 90 min of heating the solution. The respective relative amplitude decreases in the same time span from $A_{1,\,\mathrm{rel}}$ = 97 % to around $A_{1,\,\mathrm{rel}}$ = 21 %. The fluorescence lifetime detected in polymer-rich regions is increasing from $\tau_{2,\,0\,\mathrm{min}}$ = 5.7 ns to around $\tau_{2,\,6\,\mathrm{h}}$ = 5.9 ns. The respective relative amplitude is increasing in the same time span from $A_{2,\,\mathrm{rel}}$ = 3 % to around $A_{2,\,\mathrm{rel}}$ = 79 %. Both lifetimes, the short and the long fluorescence lifetime, are increasing caused by the continuous solvent evaporation. The trend of the short and long lifetime and their respective relative amplitudes is similar to the trend observed during the SEED process with toluene as the discontinuous phase. However, the relative amplitude of the polymer-rich lifetime after 90 min of $A_{2,\,\mathrm{rel}}$ = 79 % indicates that around 79 % of the molecular rotor molecules are located in these regions. In comparison, for toluene as a discontinuous solvent, the relative amplitude after 6 h was around 50 %. The detected 79 % for chloroform indicates that more solvent has evaporated from the nanoparticles than in the SEED process with toluene. The increased evaporation of chloroform was expected due to the smaller boiling temperature of chloroform.

Overall, the SEED process with chloroform occurs on a much faster time scale (90 min compared to 6 h) than the SEED process with toluene. The faster evaporation of the chloroform leads to difficulties in the measurements, first FCS autocorrelation curves could not be observed and the recorded TCSPC fluctuate as can be seen in the short and long lifetime and their respective relative amplitudes (Figure 13C and D). The recorded relative amplitudes indicate that more solvent evaporated from the nanodroplets and polymer-rich regions in the particles are more pronounced than in the nanoparticles produced with toluene as the discontinuous phase. Therefore, the use of chloroform or the utilization of solvents with a low boiling point is advantageous for the SEED process, due to a shorter reaction time and the increased evaporation from the nanodroplets.

3.3.5. Monitoring AzeNaph1 During the Miniemulsion Polymerization

After studying the formation process of nanoparticles produced by the SEED reaction, the next process to observe was the MEP reaction. Here, the molecular rotor AzeNaph1 was dissolved in styrene and mixed with the radical initiator and hexadecane. The process was carried out as in section 3.2.6 described. Samples of around 250 µL were taken after 0, 5, 10, 20, 30, 40, 60, 90, 120, 150, 180, 240, 300, 360, and 1440 min after starting the polymerization through heating. The samples were immediately cooled in an ice bath to prevent further polymerization of styrene. The samples were then observed using the combination of TCSPC with FCS. The normalized TCSPC curves are shown in Figure 14A. Fitting of the recorded fluorescence decay curves was done using equation 2 (n = 2) and with equation 3 the average fluorescence lifetime was calculated. The average fluorescence lifetime and the estimated polymer content are shown in Figure 14B. The polymer content was estimated by comparing the average fluorescence lifetime with the measured lifetime of AzeNaph1 in polystyrene containing styrene solution (see Figure 9). During the MEP reaction, no significant change in the diffusion time of the nanoparticles could be observed by FCS measurements. The identical size of the nanodroplets could also be observed in literature by comparing the size prior to the polymerization and afterward.[38] The size during the MEP reaction was determined through FCS measurements to ~ 35 nm.

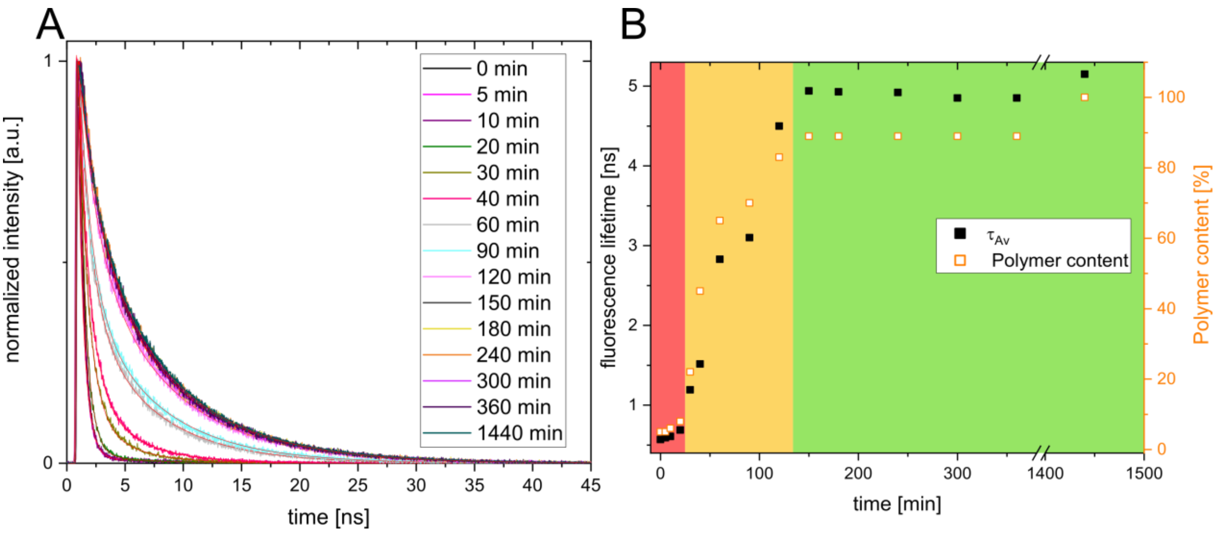

Figure 14: Typical recorded TCSPC decay curves during the MEP reaction. A) Normalized fluorescence decay curves were recorded during the TCSPC experiments after certain time intervals. B) Calculated average fluorescence lifetime (black symbols) versus the heating time. Further, the polymer content (hollow orange symbols) versus the heating time is shown. Three regions are marked in the graph: the initiation stage in red, the polymerization stage in yellow, and the glassy state in green.

The decay curves in Figure 14A experience an early shift towards longer decay times after ~ 30 min. Upwards 120 min no further change in the decay curves could be observed. In Figure 14B the calculated average fluorescence lifetime and the polymer content summarize the provided information by the molecular rotor. Even, if a size change during the MEP with FCS was not observed, the internal structure was changing and was probed by the rotor molecules. This change is reflected in the increase in the average fluorescence lifetime and the polymer content. In the beginning, a low viscosity was observed in form of a small average fluorescence lifetime and at later stages of the polymerization, a high fluorescence lifetime was observed originating from the conversion of styrene into polystyrene. The polymer content is also reflecting this trend, by increasing from ~ 5 % to ~ 90 % after 340 min.

Similar to the particle formation process using the SEED reaction, three stages could be observed in the MEP reaction. The first stage is called the initiation stage (red region in Figure 14B) and lasts for the first 20 min of the MEP reaction. The recorded fluorescence lifetime in this region was around 0.6-0.7 ns. The recorded fluorescence lifetimes in this stage are similar to the recorded fluorescence lifetimes of AzeNaph1 in pure styrene (compare Figure 7). Mechanistically in this stage, radicals are formed through thermal decomposition induced by heating the solution to 72 °C. The produced radicals initiate the polymerization of styrene and induce through this the transition to the second stage, the polymerization stage (yellow region in Figure 14B). This stage occurs from around 30 min to ~ 120 min and can be characterized by an increased viscosity, reflected by an increased recorded fluorescence lifetime of AzeNaph1 from $\tau_{\mathrm{Av,\,30\,min}}$ = 1.2 ns to $\tau_{\mathrm{Av,\,120\,min}}$ = 4.5 ns after 120 min. In this stage, the polymer content of the nanoparticles increased from around 5 % to more than 80 %. The last observed stage is the glassy state (green region in Figure 14B) and begins upwards of 120 min. Here, the monitored fluorescence lifetime of AzeNaph1 remains at a plateau value of around $\tau_{\mathrm{Av,\,360\,min}}$ = 4.9 ns. This repeatedly measured lifetime of 4.9 ns indicates the completion of the polymerization of styrene to polystyrene. Compared to the recorded fluorescence lifetime in dry polystyrene films $\tau_{\mathrm{PS\,film}}$ = 5.1 ns the plateau value of $\tau_{\mathrm{Av,\,360\,min}}$ = 4.9 ns suggested that still, unpolymerized styrene is present in the nanoparticle after 340 min. TCSPC measurements after further heating of the MEP reaction for 1440 min revealed a fluorescence lifetime in the final nanoparticles of $\tau_{\mathrm{Av,\,1440\,min}}$ = 5.1 ns. If this value is compared to the fluorescence lifetime recorded in pure polystyrene films of τ_{PS} = 5.1 ns, the lifetime measured after 1440 min suggested a complete conversion of the styrene into polystyrene. As discussed below this 100% are an overestimation, because the average fluorescence lifetime measured in NPs cannot be directly compared to that in PS film.

All recorded fluorescence decay curves were fitted with a two-component fit yielding two fluorescence lifetimes and their respective relative amplitudes. This indicates that the molecular rotor was still distributed in two different environments, a solvent-rich environment, and a polymer-rich environment. By analyzing the short and long fluorescence lifetime (Figure 15A) and their respective relative amplitudes (Figure 15B) this distribution could be observed in more detail.

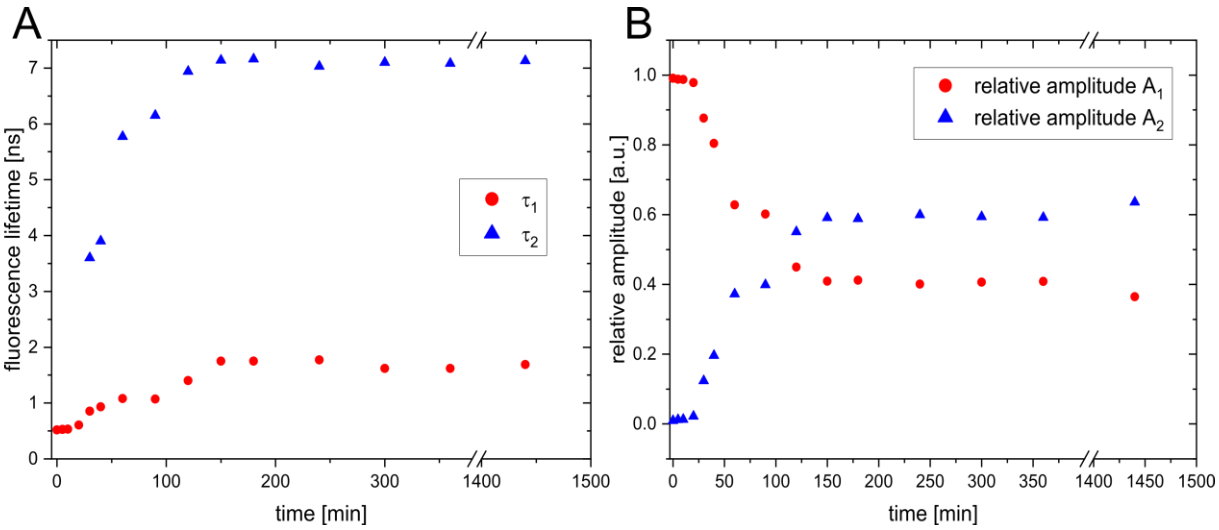

Figure 15: A) Short (red symbols) and long fluorescence lifetime (blue symbols) versus the heating time. D) Respective relative amplitudes from the short lifetime (red symbols) and long lifetime (blue symbols) from the graph in A) versus the heating time.

Both detected fluorescence lifetimes start increasing after the short initiation stage from 0-20 min. The detected increase lasted until 120 min and upwards 120 min both detected lifetimes reached a plateau value. The short lifetime increased from 0.5 ns to about 1.7 ns, while the long lifetime increased from ~ 3.6 ns to about 7 ns. The detected 7 ns for the long fluorescence lifetime was higher than the recorded lifetime in dry polystyrene films $\tau_{\text{PS film}}$ = 5.1 ns. This indicates that molecules of the molecular rotor are embedded in a region with a very high local viscosity. The relative amplitude of the long lifetime is increasing from roughly 0 % to around 60 % at the end of the polymerization process. Correspondingly to this, the relative amplitude of the short lifetime is decreasing from ~ 100 % to around 40 %. This indicates that in the final nanoparticle around 40 % of the molecular rotor molecules can be located in a low viscosity environment. A similar finding was reported by Nölle and co-authors[60] by studying the fluorescence lifetime of BODIPY-C12 during a bulk polymerization of methyl methacrylate. The distribution of around 50 % of the molecular rotor BODIPY-C12 in a low viscosity environment was also found after several days. This finding can be influenced by an uneven distribution of the respective molecular rotor between solvent-rich and polymer-rich environments. Nevertheless, the here presented study of the fluorescence lifetime in nanoparticles with AzeNaph1 and the observed bulk polymerization with BODIPY-C12[60] indicates a significant inhomogeneity on the molecular length scale. The fluorescence lifetime of molecular rotors critically depends on the available free volume in their local environment. Therefore, the results indicate that a significant variation of free volume is present in polystyrene nanoparticles with a diameter of ~ 100 nm produced by the SEED process and the MEP reaction.

3.4. Summary and Outlook

This chapter outlined that simultaneous measurements of TCSPC and FCS could be achieved by using a tailored fluorescent molecular rotor. Two different synthesizing processes were observed using the molecular rotor AzeNaph1, the SEED, and the MEP reaction. The utilization of the molecular rotor enables to follow the evolution of the inner structure of the nanodroplets into solid nanoparticles and simultaneously tracking the size of the nanoparticles. The evolution of the inner structure was followed by detecting the changing fluorescence lifetime of the molecular rotor due to increased viscosity. In both reactions, three stages could be identified during the formation process. In both reactions, in the first stage, the viscosity was low, increased during the second stage due to the solvent evaporation of polymerization, and ended in a glassy stage of the nanoparticles. In the third stage, the detected fluorescence lifetime reached a plateau value of $\tau_{\text{Av, SEED}}$ = 4.2 ns for the SEED process and $\tau_{\text{Av, MEP}}$ = 4.9 ns for the MEP reaction. Analyzing the short and long fluorescence lifetime and their respective amplitudes indicates that the molecular rotor is distributed between solvent-rich and polymer-rich environments.

The here presented experimental approach enables to estimate of the polymer content during the SEED process and the MEP reaction and gives valuable information about the transition from a nanodroplet to the final solidified nanoparticle. Further, it is possible to obtain information about structural heterogeneities on the molecular length scale. The presented concept of combining TCSPC and FCS measurements can be extended to study e.g. the internal phase separation of polymer blocks during the synthesis of block copolymers or to follow the formation of nanocapsules.

3.5. Appendix

This section provides further data sets for the SEED and MEP reactions. Information is provided in form of tables and graphs.

Table 1: Average fluorescence lifetime, short and long fluorescence lifetime, and their respective relative amplitudes of AzeNaph1 in polystyrene containing toluene solutions (section 3.3.2).

Polystyrene content [%]	**τ_{Av} [ns]**	**τ_1 [ns]**	**τ_2 [ns]**	**A_1**	**A_2**
10	0.7	0.6	4.3	1.00	0.00
20	0.7	0.6	4.0	1.00	0.00
30	0.8	0.7	4.1	0.00	0.00
40	1.1	0.8	3.8	0.98	0.02
50	1.4	0.9	3.9	0.95	0.05
60	2.2	1.2	3.8	0.84	0.16
67	2.9	1.5	4.3	0.00	0.00
70	3.4	1.7	4.6	0.65	0.35
81	4.6	2.2	5.2	0.38	0.62
85	4.8	2.7	5.4	0.37	0.63
90	5.0	3.3	5.6	0.37	0.63

Table 2: Average fluorescence lifetime, short and long fluorescence lifetime, and their respective relative amplitudes of AzeNaph1 in polystyrene containing styrene solutions (section 3.3.2).

Polystyrene content [%]	**τ_{Av} [ns]**	**τ_1 [ns]**	**τ_2 [ns]**	**A_1**	**A_2**	**Polystyrene content [%]**	**τ_{Av} [ns]**	**τ_1 [ns]**	**τ_2 [ns]**	**A_1**	**A_2**
10%	0.8	0.5	4.3	0.99	0.01	**70%**	3.2	1.6	4.6	0.72	0.28
20%	1.1	0.6	4.8	0.98	0.02	**80%**	3.9	1.8	4.9	0.58	0.42
30%	1.2	0.7	4.6	0.98	0.02	**85%**	4.9	3.1	6.0	0.55	0.45
40%	1.7	1.0	4.8	0.95	0.05	**90%**	5.1	3.3	5.8	0.43	0.58
50%	1.8	1.0	4.1	0.92	0.08	**95%**	5.2	3.6	5.9	0.44	0.56
60%	2.6	1.4	4.4	0.83	0.17						

Table 3: Weighted masses for the presented SEED processes. S1-SEED was presented in section 3.3.3, sample S2 and sample S3 are only presented in the appendix.

Sample	**V(Toluene) [mL]**	**m(SDS) [mg]**	**m(H_2O) [mL]**
S1-SEED	1.45	10.5	10
S2	1.45	10.1	10
S3	1.45	10.3	10

Table 4: Average fluorescence lifetime, short and long fluorescence lifetime, their respective relative amplitudes, estimated polymer content, diffusion times, and the respective hydrodynamic radius of AzeNaph1 during the SEED reaction with toluene as the discontinuous phase described in section 3.3.3.

Time [h]	**τ_{Av} [ns]**	**τ_1 [ns]**	**τ_2 [ns]**	**A_1**	**A_2**	**Polymer content [%]**	**τ_{Diff} [µs]**	**R_H [nm]**
0	0.8	0.7	3.1	0.95	0.05	30	1940	46
1	0.8	0.7	3.2	0.95	0.05	30	1894	45
2	1.2	0.8	3.6	0.88	0.12	41	1699	41
2.5	2.7	0.9	6.7	0.69	0.31	65	1572	38
3	4.2	1.6	7.2	0.53	0.47	76	1282	31
3.5	4.2	1.5	7.1	0.52	0.48	76	1191	29
4	4.2	1.5	7.1	0.52	0.48	76	1207	30
4.5	4.3	1.6	7.2	0.52	0.48	76	1215	30
5	4.2	1.5	7.1	0.53	0.47	76	1236	31
6	4.2	1.6	7.1	0.52	0.48	76	1250	31

Table 5: Average fluorescence lifetime, short and long fluorescence lifetime, and their respective relative amplitudes of AzeNaph1 during the SEED reaction with chloroform as the discontinuous phase described in section 3.3.4.

Time [h]	**τ_{Av} [ns]**	**τ_1 [ns]**	**τ_2 [ns]**	**A_1**	**A_2**	**Time [h]**	**τ_{Av} [ns]**	**τ_1 [ns]**	**τ_2 [ns]**	**A_1**	**A_2**
0	1.7	0.5	5.7	0.97	0.03	**45**	5.6	2.8	6.1	0.25	0.75
10	2.1	0.6	5.1	0.94	0.06	**50**	5.7	3.5	6.2	0.30	0.70
25	5.1	2.7	6.0	0.46	0.54	**60**	5.4	0.9	5.5	0.10	0.90
30	5.5	2.7	5.9	0.28	0.72	**70**	5.1	1.6	6.0	0.50	0.50
40	5.6	2.8	6.0	0.23	0.77	**90**	5.6	2.0	5.9	0.21	0.79

Table 6: Additional data set of the S2-SEED process with toluene. Average fluorescence lifetime, short and long fluorescence lifetime, their respective relative amplitudes, estimated polymer content, diffusion times, and the respective hydrodynamic radius of AzeNaph1 during the SEED reaction.

Time [h]	**τ_{Av} [ns]**	**τ_1 [ns]**	**τ_2 [ns]**	**A_1**	**A_2**	**Polymer content [%]**	**τ_{Diff} [µs]**	**R_H [nm]**
0	0.9	0.7	2.8	0.93	0.07	30	2288	52
1	0.9	0.8	2.9	0.94	0.06	30	2278	52
2	0.9	0.7	3.1	0.95	0.05	30	2330	53
3	0.9	0.7	3.1	0.95	0.05	30	2046	47
3.5	2.7	0.9	6.8	0.70	0.30	65	1620	38
4	4.3	1.6	7.2	0.52	0.48	74	1424	34
5	4.2	1.4	7.1	0.51	0.49	74	1388	33
6	4.2	1.5	7.1	0.52	0.48	74	1339	32

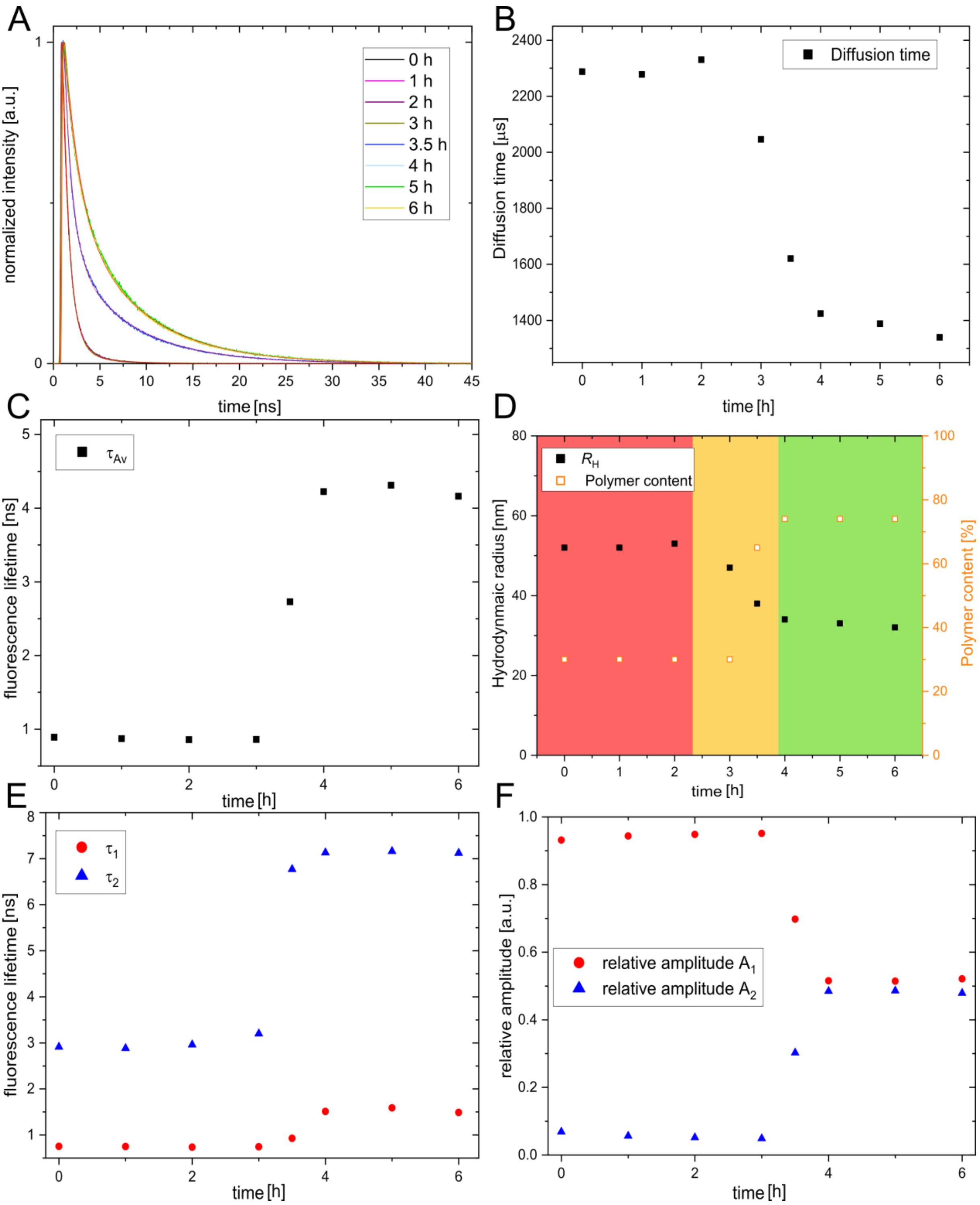

Figure 16: Overview of the S2-SEED reaction with toluene as the discontinuous phase. A) Normalized recorded decay curve. Curves were fitted with a two-component fit (equation 2; $n = 2$). B) Diffusion times versus the heating time. The diffusion times were obtained from fitting FCS autocorrelation curves. C) Calculated average fluorescence lifetime versus the heating time. D) Calculated hydrodynamic radius and polymer content versus the heating time. The hydrodynamic radius is calculated with the diffusion times shown in B). The polymer content was estimated by comparing the average fluorescence lifetime in C) with the measured values of AzeNaph1 in polystyrene containing toluene solutions. E) Single fluorescence lifetime, τ_1 (red symbols) and τ_2 (blue symbols) versus the heating time. F) Respective relative amplitudes of the short and long lifetime presented in graph E) versus the heating time. The graphs in B-F) are prepared with the presented values in Table 6.

Table 7: Additional data set of the S3-SEED process with toluene as the discontinuous phase. Average fluorescence lifetime, short and long fluorescence lifetime, their respective relative amplitudes, estimated polymer content, diffusion times, and the respective hydrodynamic radius of AzeNaph1 during the SEED reaction.

Time [h]	**τ_{Av} [ns]**	**τ_1 [ns]**	**τ_2 [ns]**	**A_1**	**A_2**	**Polymer content [%]**	**τ_{Diff} [µs]**	**R_H [nm]**
0	0.9	0.8	2.9	0.94	0.06	35	2398	54
1	0.9	0.7	2.9	0.94	0.06	35	2278	52
2	0.9	0.7	3.0	0.95	0.05	35	2199	53
3	0.9	0.7	3.2	0.95	0.05	35	1985	46
3.5	2.7	0.9	6.8	0.69	0.31	65	1598	37
4	4.2	1.5	7.1	0.52	0.48	74	1366	32
5	4.3	1.6	7.2	0.51	0.49	75	1396	33
6	4.2	1.5	7.1	0.53	0.47	74	1463	34

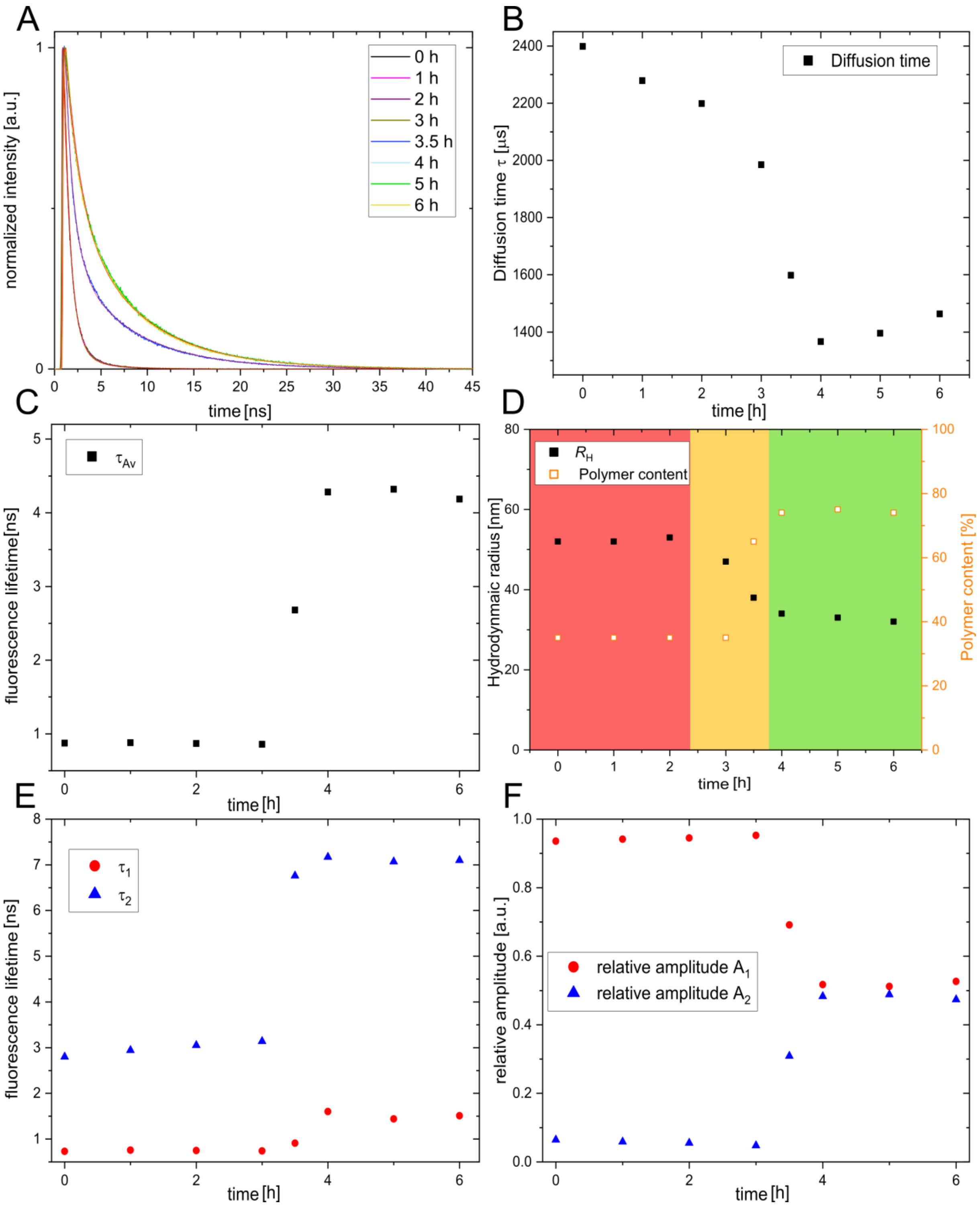

Figure 17: Overview of the S3-SEED reaction with toluene as the discontinuous phase. A) Normalized recorded decay curve. Curves were fitted with a two-component fit (equation 2; *n* = 2). B) Diffusion times versus the heating time. The diffusion times were obtained from fitting FCS autocorrelation curves. C) Calculated average fluorescence lifetime versus the heating time. D) Calculated hydrodynamic radius and polymer content versus the heating time. The hydrodynamic radius is calculated with the diffusion times shown in B). The polymer content was estimated by comparing the average fluorescence lifetime in C) with the measured values of AzeNaph1 in polystyrene containing toluene solutions. E) Single fluorescence lifetime, τ_1 (red circle), τ_2 (blue triangles) versus the heating time. F) Respective relative amplitudes of the short and long lifetime presented in graph E) versus the heating time. The graphs in B-F) are prepared with the presented values in Table 7.

Table 8: Average fluorescence lifetime, short and long fluorescence lifetime, their respective relative amplitudes, estimated polymer content, diffusion times, and their respective hydrodynamic radius of AzeNaph1 during the MEP reaction described in section 3.3.5.

Time [min]	**τ_{Av} [ns]**	**τ_1 [ns]**	**τ_2 [ns]**	**A_1**	**A_2**	**Polymer content [%]**	**τ_{Diff} [µs]**	**R_H [nm]**
0	0.6	0.5	5.9	0.99	0.01	5	1279	30
5	0.6	0.5	6.0	0.99	0.01	5	1493	35
10	0.6	0.5	6.4	0.99	0.01	6	1540	36
20	0.7	0.6	4.4	0.98	0.02	8	1530	36
30	1.2	0.9	3.6	0.88	0.12	22	1672	39
40	1.5	0.9	3.9	0.80	0.20	45	1920	44
60	2.8	1.1	5.8	0.63	0.37	65	1695	39
90	3.1	1.1	6.2	0.60	0.40	70	1409	33
120	4.5	1.4	6.9	0.45	0.55	83	1386	33
150	4.9	1.8	7.1	0.41	0.59	89	1457	34
180	4.9	1.8	7.2	0.41	0.59	89	1354	32
240	4.9	1.8	7.0	0.40	0.60	89	1523	36
300	4.9	1.6	7.1	0.41	0.59	89	1365	32
360	4.9	1.6	7.1	0.41	0.59	89	1445	34
1440	5.2	1.7	7.1	0.36	0.64	100	1455	34

Table 9: Weighted masses for the MEP reaction. M1-MEP was presented in section 3.3.5. Sample M2 and sample M3 are presented in the Appendix.

Sample	**V(Styrene) [mL]**	**m(AIBN) [mg]**	**V(HD) [µL]**	**m(H_2O) [mL]**	**m(SDS) [mg]**
M1-MEP	6.55	100.2	325	24	71.8
M2	6.50	104.4	325	24	73.1
M3	6.53	101.6	325	24	72.5

Table 10: Additional data set of the M2-MEP reaction. Average fluorescence lifetime, short and long fluorescence lifetime, their respective relative amplitudes, estimated polymer content, diffusion times, and their respective hydrodynamic radius of AzeNaph1 during the MEP reaction.

Time [min]	**τ_{Av} [ns]**	**τ_1 [ns]**	**τ_2 [ns]**	**A_1**	**A_2**	**Polymer content [%]**	**τ_{Diff} [µs]**	**R_H [nm]**
0	0.6	0.5	5.8	0.99	0.01	8	1609	40
10	0.6	0.5	6.4	0.99	0.01	8	1555	39
20	0.6	0.6	6.3	0.99	0.01	9	1668	41
30	0.6	0.6	5.6	0.99	0.01	9	2283	55
50	1.0	0.7	6.3	0.95	0.05	15	2336	56
60	1.3	0.8	6.4	0.92	0.08	30	2063	50
90	2.3	1.2	6.2	0.78	0.22	62	2134	52
120	3.3	1.5	6.4	0.64	0.36	72	1453	36
150	3.9	1.6	6.6	0.53	0.47	81	1768	44
180	4.3	1.6	6.9	0.49	0.52	84	2256	54
240	4.0	1.7	6.6	0.54	0.46	82	2022	49
300	3.8	1.6	6.4	0.53	0.47	80	1964	48
360	3.8	1.9	6.0	0.54	0.46	80	1644	41

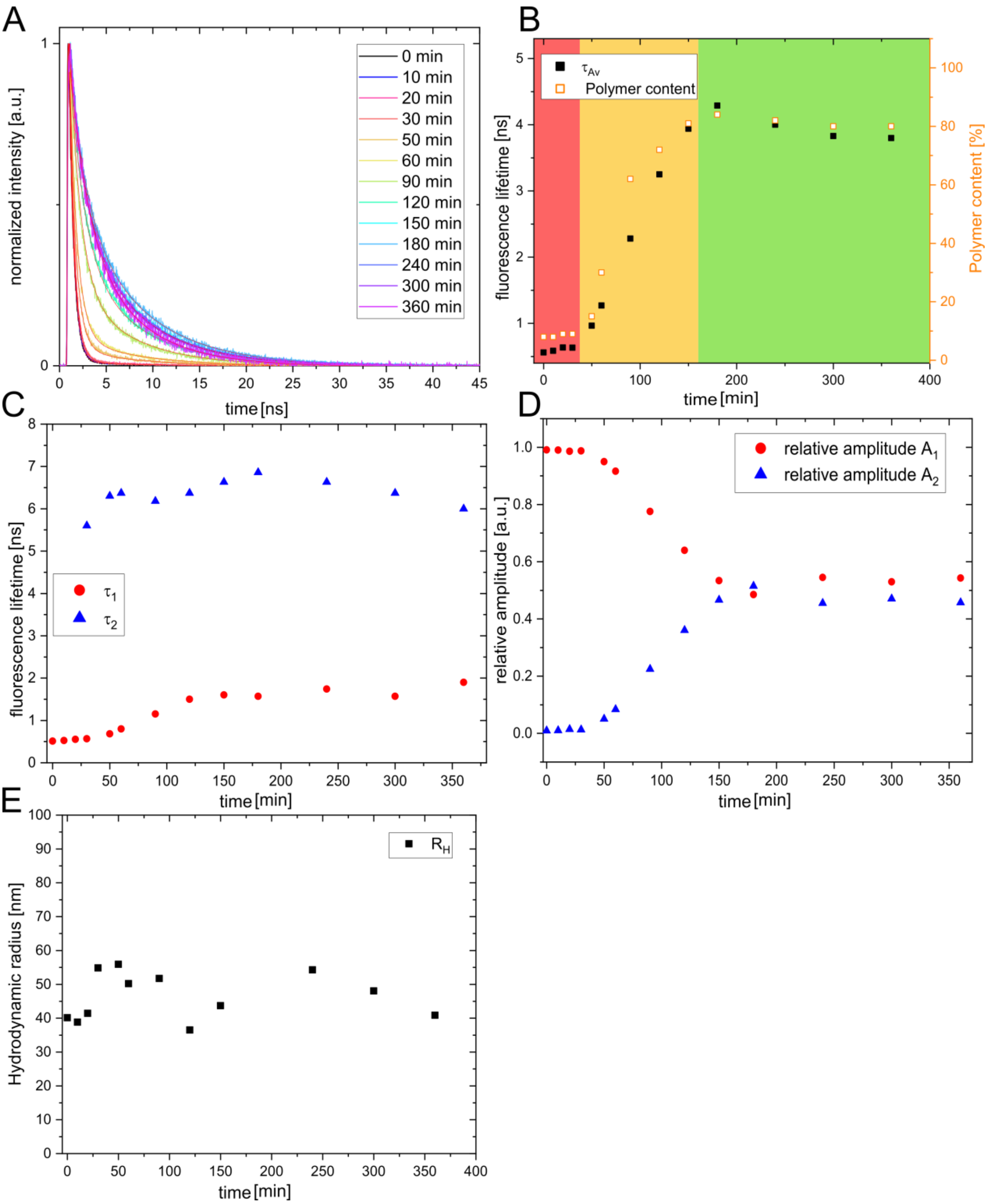

Figure 18: Overview of the M2-MEP reaction. A) Normalized recorded decay curve. Curves were fitted with a two-component fit (equation 2; $n = 2$). B) Calculated average fluorescence lifetime (black symbols) and polymer content (hollow orange symbols) versus the heating time. C) Single fluorescence lifetime, τ_1 (red symbols), τ_2 (blue symbols) versus the heating time. D) Respective relative amplitudes of the short and long lifetime presented in graph C) versus the heating time. E) Hydrodynamic radius versus the heating time. The graphs in B-E) are prepared with the presented values in Table 10.

Table 11: Additional data set of the M3-MEP reaction. Average fluorescence lifetime, short and long fluorescence lifetime, their respective relative amplitudes, estimated polymer content, diffusion times, and their respective hydrodynamic radius of AzeNaph1 during the MEP reaction.

Time [min]	**τ_{Av} [ns]**	**τ_1 [ns]**	**τ_2 [ns]**	**A_1**	**A_2**	**Polymer content [%]**	**τ_{Diff} [µs]**	**R_H [nm]**
0	0.5	0.5	5.5	0.99	0.01	8	1634	38
10	0.6	0.5	6.3	0.99	0.01	8	1923	44
20	0.6	0.5	5.9	0.98	0.02	9	2457	55
30	0.9	0.6	6.6	0.94	0.06	9	2572	57
50	1.2	0.8	6.2	0.92	0.08	30	1799	42
60	1.8	1.1	5.5	0.83	0.17	50	2386	54
90	3.0	1.3	5.9	0.62	0.38	69	1585	37
120	4.4	1.5	6.8	0.46	0.54	83	1609	38
150	5.1	1.6	7.1	0.36	0.64	100	1599	37
180	5.3	1.7	7.2	0.36	0.64	100	1614	38
240	4.9	1.6	7.2	0.40	0.60	87	1480	35
300	4.8	1.5	7.0	0.41	0.59	85	1443	34
360	4.7	1.5	7.0	0.41	0.59	84	1487	35

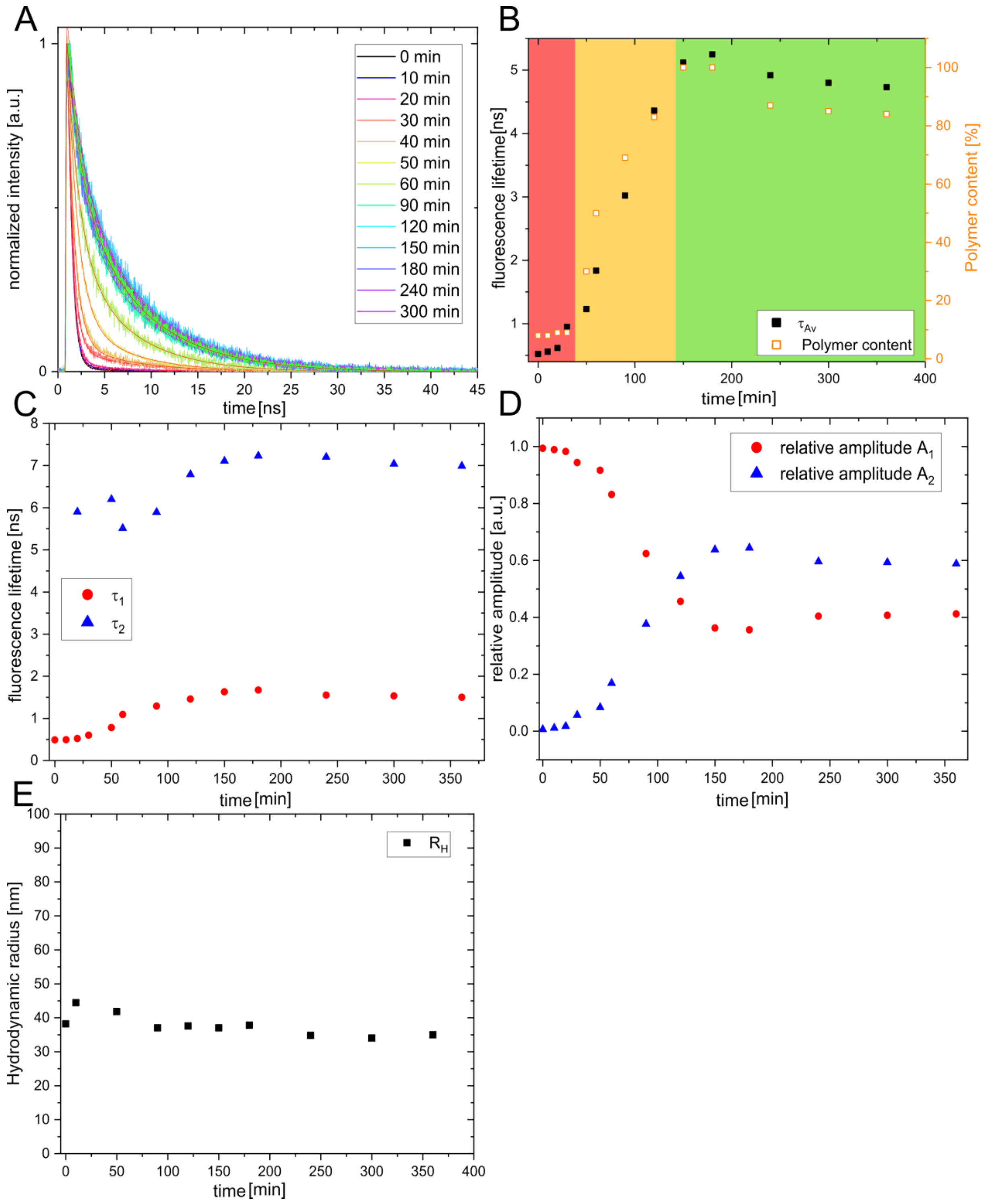

Figure 19: Overview of the M3-MEP reaction. A) Normalized recorded decay curve. Curves were fitted with a two-component fit (equation 2; $n = 2$). B) Calculated average fluorescence lifetime (black symbols) and polymer content (hollow orange symbols) versus the heating time. C) Single fluorescence lifetime, τ_1 (red symbols), τ_2 (blue symbols). D) Respective relative amplitudes of the short and long lifetime presented in graph C). E) Hydrodynamic radius versus heating time. The graphs in B-E) are prepared with the presented values in Table 11.

4. Chapter: Fluorescence Correlation Spectroscopy for Monitoring the Fate of Degradable Nanocarrier in the Blood Stream[2]

Nanocarrier (NC) mediated transportation of sensible or toxic drug molecules to their target site is a promising therapeutic approach. For a successful transportation of the cargo to the intended target site, it is necessary for the NC to circulate for a prolonged period of time in the blood vessel system. During the circulation time, interaction of NCs and blood plasma proteins, blood cells, or the experienced shear forces can lead to an alteration in the properties of the NC. The characterization of the alternated NCs properties is a challenging task due to the high concentration of blood cells and plasma proteins. Nonetheless, it is necessary to monitor the properties of NC in whole blood for the development of efficient NC-based therapies.

Therefore, the following chapter presents a newly developed approach that enables NC characterization in whole blood samples. The composition of blood will be presented in section 4.1.1, followed by section 4.1.2, which deals with the interaction between NCs and blood. In section 4.1.3 techniques are presented to monitor NCs from an aqueous environment to *in vivo* conditions. In section 4.3.1 the fluorescence correlation spectroscopy (FCS) blood measurement approach will be introduced and initial tests will be discussed. Section 4.3.3 will deal with the monitoring of the fate of NCs inside living mice.

---

[2] The chapter **Fluorescence Correlation Spectroscopy for Monitoring the Fate of Degradable Nanocarrier in the Blood Stream** is based on the publication published in Biomacromolecules “Fluorescence Correlation Spectroscopy Monitors the Fate of Degradable Nanocarriers in the Blood Stream” by Sascha Schmitt, Anne Huppertsberg, Adrian Klefenz, Leonard Kaps, Volker Mailänder, Detlef Schuppan, Hans-Jürgen Butt, Lutz Nuhn, Kaloian Koynov (https://pubs.acs.org/doi/10.1021/acs.biomac.1c01407). Figures in this section are adapted and reproduced by the permission American Chemical Society (ACS).

4.1. Introduction

4.1.1. Blood

The main function of blood is the transportation of nutrients, metabolites, and respiratory gases like oxygen and carbon dioxide and their distribution over the whole body. Further, it maintains homeostasis and plays an important role in the counteraction of bleeding by coagulation and the immune defense.[111, 112] Blood is also considered as connective tissue.

An adult body possesses around 5 L of blood, which makes up 6 % to 8 % of the body weight, whereby the cellular fraction is around 42 % for women and 47 % for men.[111] The cellular fraction is called hematocrit and is composed of the red blood cells erythrocytes, white blood cells the leucocytes, and the platelets also called thrombocytes. A healthy adult possesses around $5\cdot10^{12}$ red blood cells (erythrocytes) per liter of blood. The red blood cells contain large amounts of hemoglobin, which are responsible for oxygen transportation. Oxygen can bind to the free coordination site of an iron ion, which is part of the protoporphyrin ring of the hemoglobin. Depending on the oxygen saturation of the blood, the color of blood can be a darker or brighter red. The leucocytes (white blood cells) are the second cellular fraction and a healthy adult possesses around $7\cdot10^{9}$ leucocytes per liter of blood. Leucocytes play an important role in specific and unspecific immune defense. Depending on their origin the leucocytes can be divided into three subgroups: the granulocytes, monocytes, and lymphocytes. The granulocytes possess an important role in the unspecific immune defense. The monocytes and the tissue macrophages are responsible for the phagocytic system of the body and can encapsulate foreign particles and neutralize them. The specific immune system is formed by the third fraction, the lymphocytes. The thrombocytes are the third cellular fraction of blood. A healthy adult possesses around $250\cdot10^{9}$ thrombocytes per liter of blood and they are responsible for the initiation of blood coagulation.[111]

The remaining part of the blood (58 % for women; 53 % for men) consists of blood plasma. The aqueous blood plasma contains a large number of proteins, the so-called plasma proteins ($\sim$ 70 g L^{-1})[111], nutrients, and metabolites. The most abundant plasma proteins are albumin, α1-, α2-, β-, and γ-globulin and are mostly synthesized in the liver. Albumin, the most abundant blood plasma protein, is mostly responsible for the transportation of bilirubin, urobilin, and fatty acids. Further, the albumin proteins are responsible for around 80 % of the osmotic pressure of blood. The globulins are mainly responsible for the binding and transportation of vitamins, hormones, lipids, and minerals.[111, 112] Furthermore, the blood plasma proteins contribute to the buffer capacity of the blood. Blood plasma is generated by removing the red blood cells from whole blood samples, whereas blood serum is produced by removing the red blood cells and the coagulation proteins.

4.1.2. The Fate of Nanocarrier Inside the Blood Stream

After intravenous injection of NCs into a patient's body, the first environment encountered by the NC is blood. The blood stream will bring the NCs to their specific target site inside the body. Therefore, the fate of the NCs critically depends on the stability of the NCs inside the blood stream.[113, 114] After intravenous injection of NCs interactions between the NCs and the biological environment take place, as the interaction with blood plasma proteins and blood cells. Therefore, it is essential to ensure that NCs possess a prolonged circulation time inside the blood stream without undergoing aggregation, decomposition, or a premature loss of the drug cargo.

A prolonged circulation time inside the blood stream from NCs is counteracted by rapid clearance from the blood stream. The clearance can be induced by the adsorption of blood plasma proteins, commonly referred to as protein corona. Positively charged particles with a hydrophobic surface tend to attract more plasma proteins than neutral or negatively charged particles with a hydrophilic surface.[115, 116] Immunoglobins and fibrinogen are among the abundant plasma proteins and are commonly referred to as opsonins.[117] The protein corona of nanoparticles containing opsonic proteins can be recognized and phagocytosis by immune cells. The immune cells, which are a part of the mononuclear phagocyte system can be found in organs such as the liver, spleen, lung, and bone marrow.[118, 119] Therefore, NCs with a protein corona containing opsonic proteins are cleared from the blood stream mainly by the spleen and liver.[120] Besides being recognized by the mononuclear phagocyte system, the protein corona possesses also an influence on the size[121, 122], surface charge[123-125], can induce aggregation[126, 127] and can hinder the active targeting of ligands[128-131].

Nevertheless, several strategies are available to increase the blood circulation time of NCs by reducing the adsorption of proteins and the recognition by the mononuclear phagocytosis system. These strategies can prolong the resident time inside the blood stream and therefore also increase the probability to reach their target site. One strategy relies on giving the NC a pre-coating of specific proteins. Here, a pre-incubation of NCs in blood plasma with a reduced concentration of opsonic proteins showed a reduced cellular uptake by macrophages.[132-135] Besides controlling the size, surface charge, or shape of the NC, modifying the surface is another strategy for increasing the circulation time of NCs in the blood vessel system. Therefore, the NCs surface can be coated with so-called "stealth" polymers including polyethylene glycol[136-139], polysarcosine[140-143], or zwitterionic polymers[144-146]. NCs which are modified with the aforementioned polymers show a prolonged circulation time inside the blood stream by reducing the adsorption of proteins or by promoting the adsorption of proteins of a specific type.[137, 147]

One important aspect is that the observed protein corona of NCs from *in vitro* experiments differ from protein coronas observed during *in vivo* experiments.[117, 131] Therefore, investigation of the interaction between NCs and plasma proteins is only limited transferable between *in vitro* and *in vivo* experiments. Hence, is it necessary to observe the behavior of NCs directly under *in vivo* conditions to gain a complete understanding of the fate of the NC inside the blood stream.

4.1.3. Techniques to Study Nanocarrier: From Aqueous Environment to *In Vivo*

NCs are characterized after the synthesis in regards to size, dispersity, surface properties, stability, and purity. Especially, NCs designed for the drug delivery process needed to be characterized in different environments. Here, the complexity of the environment is increasing starting from the aqueous buffer condition for storage and preparation to a more complex environment like blood serum, blood plasma, and whole blood. To characterize NCs under aqueous conditions a vast toolbox of measurement techniques is available for determining the aforementioned properties like size and stability. Commonly applied characterization techniques to study NCs are dynamic light scattering (DLS), FCS, transmission electron spectroscopy (TEM), nanoparticle tracking analysis, size exclusion chromatography, zeta potential, and nuclear magnetic resonance.[14, 15, 23, 45, 46] However, most of these techniques cannot be easily adapted to more complex environments like blood plasma or whole blood samples.

For studying NCs in blood serum or blood plasma characterization methods are needed which tolerate high protein concentrations. One possible characterization method is the DLS technique. DLS is based on measuring the scattering intensity arising from the Brownian motion of the solutes. The intensity fluctuation, similar to FCS (compare section 2.4), is autocorrelated and could be fitted by an exponential function. In difference to FCS, the DLS techniques do not rely on fluorescence and therefore the technique is not limited to fluorescently labeled samples only. As a consequence, a multi-exponential fitting function is a necessity to take into account the different contributions arising from the blood proteins and lipids. Nevertheless, DLS was successfully applied to measure PEGylated poly-L-lysines (PEG: polyethylene glycol) nanoparticles and polystyrene particles in blood serum and blood plasma.[135, 148] Another method, which tolerates high protein concentrations is the FCS technique. FCS has been widely used to study NCs in an aqueous environment[36, 72, 149, 150] in regards to drug loading efficiency[150-152], stability[153, 154], and drug release[155]. Furthermore, FCS can also be conducted in blood serum and blood plasma[75, 156] and was also applied to follow the size change after a protein corona formation[157].

After studying the properties of NCs in blood serum and blood plasma, the influence of whole blood on NCs needed to be investigated. Therefore, NCs can be incubated in blood followed by a subsequent sample work-up to remove the blood cells. The blood cells possess a disruptive influence on the aforementioned characterization techniques like DLS, TEM, or size exclusion chromatography. Removing the cellular fraction of the blood can be achieved by centrifugation, dialyzing, or precipitation. For example, Tiiman et al.[158] studied with FCS the presence of amyloidogenic oligomeric aggregates in blood serum from Alzheimer's patients. Herefore, Tiiman and co-workers used a centrifugation step prior to the FCS measurements to remove the blood cells and found with FCS that the size and the concentration of these aggregates are higher than in a control group. However, these measurement conditions differ from the biological environment in which the incubation takes place. Further, during a centrifugation step, strong shear forces occur which can harm the sample in regards to decomposition, loss of cargo, or induce aggregation. Moreover, large blood volumes (~ mL) are needed for a sample work-up, which cannot be obtained for example from rodents at regular time intervals. In 2018 a study was published where the authors applied FCS directly in whole blood samples.[52] They used NCs labeled with a near-infrared (NIR) dye to reduce light absorption and studied the size, stability, and premature drug release of NCs incubated at 4 °C in blood for a total time of 30 hours. Therefore, they applied a very slow continuous flow to the blood sample inside a microchannel. This procedure ensures that the FCS observation volume is not blocked by blood cells the whole measuring time.

After measuring the properties of NCs, *ex vivo* in whole blood samples, the next step is to measure the properties of the NCs *in vivo*. Besides the disturbing influence of the blood, the biological tissues like the skin possess a disturbing influence, too. Optical methods, operating in the visible light region, suffer from a reduced penetration depth due to scattering and absorption. For example, hemoglobin and oxyhemoglobin show strong absorption in the visible wavelength range ($\lambda < 600$ nm), whereas the absorption of water increases around $\lambda > 1100$ nm. This leads to an absorption minimum in the NIR region, the so-called biological window (700 nm to 1100 nm). Measurement techniques operating in this NIR region profit from the reduced absorption.[159] For example, the NIR fluorescence imaging technique uses very sensitive detectors in the NIR region to visualize the distribution of fluorescent species in the NIR region inside the body.[34, 160-164] The FCS technique can be adapted to the NIR range as already presented by the work from Negwer and co-workers[52] and is also able to measure NCs directly *in vivo* as demonstrated by Fu and co-workers[73]. The authors used multi-photon FCS to quantify with fluorescent nanoparticles the *in vivo* cerebral blood flow in thinned-skulled live mice. Besides the quantification of the blood flow, the authors were able to obtain some qualitative information on changes in the nanoparticle concentration and on the dissociation of fluorophores from the nanoparticles. In addition to the techniques using the biological windows, visualization techniques for NCs *in vivo* are available which do not rely on the biological window. Techniques like computer tomography[45, 46, 165], or magnetic resonance imaging[45, 46, 166] are broadly applied to observe the biodistribution of NCs *in vivo*.

The aforementioned techniques are able to follow the biodistribution of NCs over time, but could not observe if the NCs aggregated, undergo a decomposition, or if they suffer from a premature loss of cargo. The aforementioned studies applying FCS in whole blood samples are not well-suited to follow the fate of NCs during the drug delivery process in a live rodent. The necessity for large blood volumes to apply the flowing blood method[52] makes this method impractical for monitoring the fate of NCs in a mouse model. Also, the method to record FCS through a thinned skull[73] lacks the quantitative accuracy needed for precise NCs characterization. This limitation arises from the high flow rates in the blood vessel system. Therefore, a newly developed characterization approach for NCs with the FCS technique in blood is presented and discussed in this chapter. The new approach enables FCS blood measurements with small sample volumes and without the need for further sample preparation.

4.2. Materials and Methods

4.2.1. Materials

Solvents (HPLC grade) were purchased from Acros Organics (Geel, Belgium) and Fisher Scientific. A MILLI-Q® Reference A+ System was used to obtain Millipore water. Fluorescent dyes (Alexa 488, OregonGreen cadaverine 488, Alexa 647) were bought from Thermo Fisher Scientific (Waltham, MA, USA). The Vivid™ plasma separation membrane GR grade was obtained from Pall Corporation (Port Washington, NY 11050). TEM grids (mesh size 100; Standardnetzchen “Pyser”) were purchased from Plano GmbH, Wetzlar, Germany.

The pH-responsive nanogel which acts as NCs were synthesized by Anne Huppertsberg, WG Nuhn MPIP following an earlier report.[19] Briefly, methacrylamides with squaric ester amides as functional groups were grafted under controlled radical polymerization conditions on linear PEG chains. These block copolymers self-assemble into precursor micelles which then could be sequentially functionalized with amine-bearing acid-sensitive ketal crosslinkers, drugs, dyes, and short oligo(ethylene glycol)s. For this project, the precursor micelles were labeled with OregonGreen 488 dye.

The guidelines of the ethics committee of the state medical association Rhineland-Palatinate were followed if human blood plasma and human blood were collected and handled. Human blood was obtained by a male volunteer donor and was collected in Li-Heparin coated tubes (Sarstedt, Nümbrecht, Germany) for preventing clotting. The collected blood was used immediately or stored at 4 °C for a maximum of two days.

4.2.2. Fluorescence Correlation Spectroscopy

A commercially available confocal microscope (LSM 880, Carl Zeiss, Jena, Germany) was used to perform the FCS experiments. The LSM880 was equipped with a C-Apochromat 40x/1.2 W (Carl, Zeiss, Jena, Germany) water immersion objective. Alexa 488, OregonGreen 488, and Alexa 647 were excited by an Argon laser (λ = 488 nm) and a HeNe laser (λ = 633 nm) respectively, which were coupled to the LSM by glass fiber. For Alexa 488 and OregonGreen 488, the spectral range of 508-562 nm, and for Alexa 647 the spectral range of 655-699 nm was detected using a spectral detection unit (Quasar, Carl Zeiss). This spectral detection unit comprises a multi-anode photomultiplier operating in photon counting mode. A stainless steel Attofluor™ chamber (Thermo Fisher Scientific, Waltham, MA, USA) was utilized as a sample holder, holding a coverslip. The studied sample, PBS buffer, and blood plasma (~ 50 µL) were placed directly on the coverslip and measured. The observation volume was placed ~ 15 µm above the coverslip. Such short penetration lengths are necessary to diminish spherical aberration effects, due to the higher refractive index of blood plasma.[52] For measuring whole blood samples, a round slice of the plasma separation membrane was placed in the Attofluor™ cell chamber. Between the plasma separation membrane and the coverslip was placed a TEM grid, which acts as a spacer. Before adding the blood sample on top of the plasma separation membrane, the TEM grid was localized in the reflection mode and the observation volume was placed next to it. Then carefully 30 µL of the blood sample was added on top of the plasma separation membrane. FCS autocorrelation curves were recorded for 200 seconds in repetitions of 10 seconds. The autocorrelation curves were fitted with the analytical expression of equation 8 using the ZEN software (Carl Zeiss, Jena, Germany). The Alexa 647 dye and the unimer were fitted with an additional triplet component with τ_T in the range of 2-4 µs (equation 9). This triplet component was not necessary for measuring other dyes or multiple labeled NCs. Calibration of the observation volume for FCS experiments was done before every measurement with either Alexa 488 or Alexa 647 dissolved in MilliQ-water.

4.3. Results and Discussion

4.3.1. Blood Measurement Approach for Enabling Fluorescence Correlation Spectroscopy Measurements

Positioning the confocal detection volume inside a blood droplet results in a partially or fully occupied FCS detection volume from blood cells. As a result, the blood cells inside the detection volume prevents the recording of FCS autocorrelation curves. Therefore, recording FCS autocorrelation curves in a static blood droplet is accompanied by a tedious search for a cell-free spot as already reported by Negwer and co-workers.[52] For realizing FCS measurements without a tedious search for a cell-free spot a porous structure is needed that allows only the liquid part of the blood and the NCs to pass through and therefore hinder the blood cells from entering the FCS detection volume (see Figure 20C). As a porous material, membranes are suitable candidates for separating blood cells from the liquid part of the blood and its solutes. Thus, several commercially available membranes were characterized and one suitable membrane was selected from Pall Cooperation. The selected Vivid plasma separation membrane possesses a high blood plasma recovery, low analyte binding, and a low tendency to induce hemolysis.[167] The selected membrane consists of an asymmetric porous polysulfone structure (see Figure 20D) with a thickness of around 330 µm ± 20 µm.

To utilize the selected plasma separation membrane for the blood measuring approach round slices of the plasma separation membrane with a diameter of ~ 10 mm were prepared. These slices were placed on top of a TEM grid (thickness ~ 20 µm) with a coverslip as support. An AttoFluor™ cell chamber functions as a sample holder for the coverslip. In Figure 20A the AttoFluor™ cell chamber with plasma separation membrane and blood is shown mounted on a confocal microscope. The utilized confocal FCS setup is shown schematically in Figure 20B and is described in more detail in section 2.4 and section 4.2.2. The setup discussed in section 2.4 differs from the setup shown here in regards to the sample holder. Here, the shown AttoFluor™ cell chamber containing the TEM grid and the plasma separation membrane with a blood droplet on top.

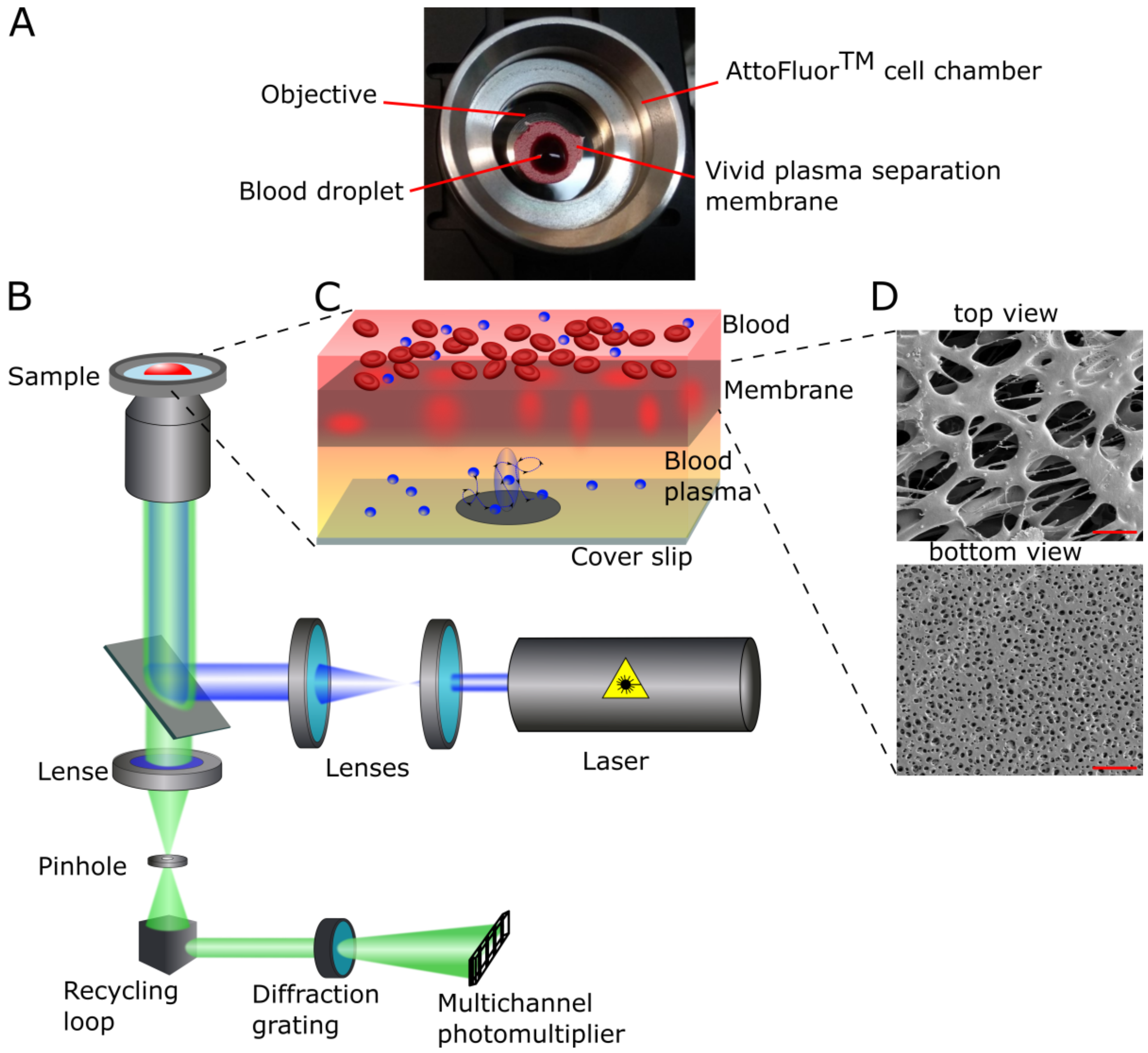

Figure 20: Schematic overview of the FCS setup optimized to enable blood measurements. A) Picture of the blood measuring setup. Marked are the objective, blood droplet, the AttoFluor™ cell chamber, and the plasma separation membrane. B) The illustrated optical setup differs from the setup discussed in section 2.4 in regards to the sample holder. Here, the AttoFluor™ cell chamber hosts the plasma separation membrane and the TEM grid. C) The inset illustrates schematically how the membrane prevents the blood cells from entering the confocal volume. By placing the blood droplet on top of the plasma separation membrane the liquid part of the blood and the NCs can diffuse into the membrane, whereas the blood cells are hindered to enter the plasma separation membrane. In the space between the membrane and the coverslip, the confocal detection volume is placed. This enables disturbance-free FCS measurements in the generated blood plasma. D) SEM pictures showing the top and bottom sides of the membrane (scale bar 50 µm). Reprinted and adapted from Biomacromolecules 2019, 20, 3786−3797; https://doi.org/10.1021/acs.biomac.9b00868. Copyright 2019 American Chemical Society.

The working principle of the blood measurement approach is illustrated in Figure 20C. After placing the blood on top of the plasma separation membrane, the liquid part of the blood is diffusing inside the membrane, whereas the blood cells are restrained to enter the plasma separation membrane, due to their larger size. The asymmetric nature of the plasma separation membrane is shown in Figure 20D in form of SEM pictures of the top side and bottom side of the membrane. The porous structure of the membrane is decreasing from a relatively open structure (Figure 20D, top view) with large hole diameter to a structure possessing only a small hole diameter (Figure 20D, bottom view). By continuous diffusion of the blood droplet towards the bottom of the membrane, the hole size (void volume) decreases leading to entrapping the cellular components of the blood. As a result, only the liquid part, the blood plasma, and its dissolved compartments e.g. the dissolved NCs can pass through the membrane and reach the free space between the coverslip and the membrane. The free space between the coverslip and the membrane is provided by the thickness of the TEM grid and is around 20 µm. In this region is placed the confocal detection volume and due to the restraining of the blood cells, disturbance-free FCS measurements are possible.

Experimentally the blood measurement approach was utilized as followed: Prior to the measurement, the TEM grid was localized in the reflection mode and the confocal detection volume was positioned directly next to the TEM grid. After positioning the detection volume next to the TEM grid, a blood droplet (~ 30 µL) was placed carefully on top of the plasma separation membrane. Next, the position of the detection volume was checked again and placed for all blood measurements 15 µm above the glass slide. Such short penetration lengths were necessary to avoid measuring inside the plasma separation membrane, due to the thickness of the TEM grid of ~ 20 µm. At this position, FCS measurements were conducted for 200 s in repetitions of 10 s.

Initial FCS measurements were performed with Alexa 647, a commonly used FCS dye with a well-known diffusion coefficient. Therefore, Alexa 647 was incubated for 30 min in either PBS buffer, human blood plasma, or heparin-treated human blood at a concentration of 10 nM L^{-1} (Figure 21).

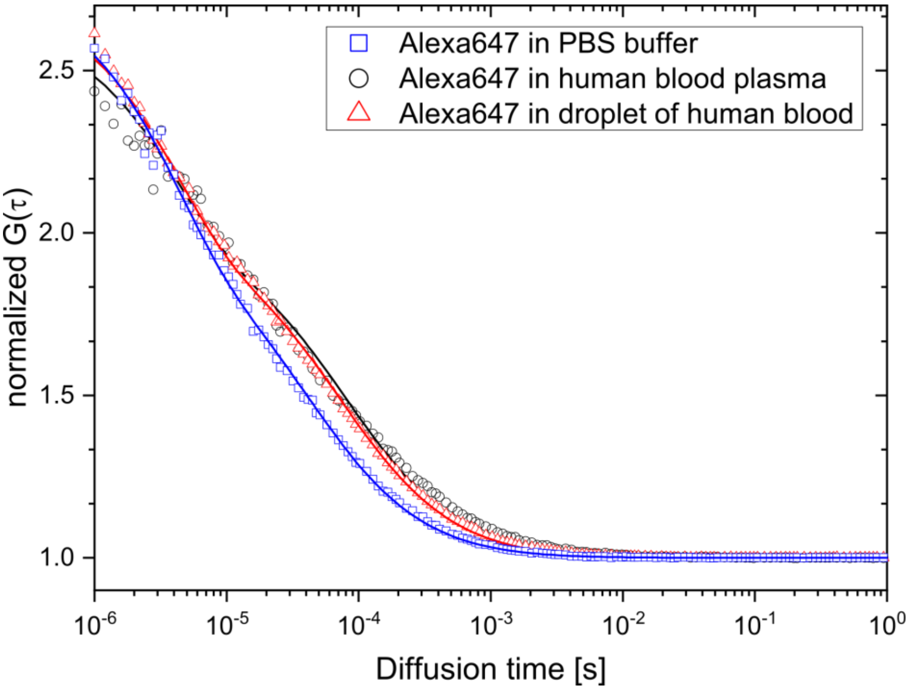

Figure 21: Normalized FCS autocorrelation curves of Alexa 647 in PBS buffer (blue symbols), human blood plasma (black symbols), and heparin-treated human blood (red symbols). The measurements in PBS and blood plasma were measured without the blood plasma separation membrane, whereas Alexa 647 in human blood was measured using the blood measurement approach with the plasma separation membrane. Reprinted and adapted from Biomacromolecules 2019, 20, 3786−3797; https://doi.org/10.1021/acs.biomac.9b00868. Copyright 2019 American Chemical Society.

The measurements in PBS buffer and blood plasma were done without using the blood plasma separation membrane. All curves were fitted with a one-component fit and a triplet term (equation 9; $m = 1$). Nearly indistinguishable autocorrelation curves were recorded in blood plasma and human blood. The diffusion times for both solvents were yielded to $\tau_{\text{plasma}} = 69 \pm 4$ µs and $\tau_{\text{blood}} = 71 \pm 4$ µs. The recorded diffusion time for Alexa 647 in PBS buffer was recorded to $\tau_{\text{PBS}} = 45 \pm 2$ µs. The difference in the recorded diffusion time for Alexa 647 in the tested solvents arises from an increased viscosity in blood plasma and is roughly 1.5-times[52] higher if compared to PBS buffer. Carefully considering the increased viscosity the hydrodynamic radius R_H can be calculated with the Stokes-Einstein relation (equation 11). For all three sets of experiments (PBS, blood plasma, whole blood) the hydrodynamic radius could be calculated to $R_H \approx 0.8$ nm. These experiments indicate several conclusions, first that the Alexa 647 dye molecules do not interact with blood plasma proteins[168] as shown by the diffusion times (hydrodynamic radius respectively) obtained from the blood plasma and whole blood measurements. Second and more importantly these results indicate that the developed blood measuring approach can be used to successfully monitor diffusion times in a nanomolar concentration range without influencing the observed species.

4.3.2. Characterization of the pH-responsive Squarogel Nanocarrier

After building and testing the developed blood measurement approach, a biodegradable drug NC with potential application for immunodrug delivery and sufficient blood circulation time was observed. For this purpose, a pH-degradable nanogel NCs were selected, which were provided by Anne Huppertsberg and Lutz Nuhn (MPIP). For a brief synthesis[19] description for the squarogel NCs see section 4.2.1. The squarogel NC possesses a high degree of PEGylation, which results in prolonged blood circulation time.[19] Further, as a crosslinking reagent for the NC squarogel a pH-responsive amine-bearing acid-sensitive ketal crosslinker was selected. The pH-responsive crosslinking of the squarogel NC was tested under acidic conditions and could be followed by FCS. To monitor the degradation of the squarogel NC with FCS, the NC was labeled with OregonGreen 488. In Figure 22 normalized FCS autocorrelation curves are shown for the pH degradation over time of the NCs within 480 min.

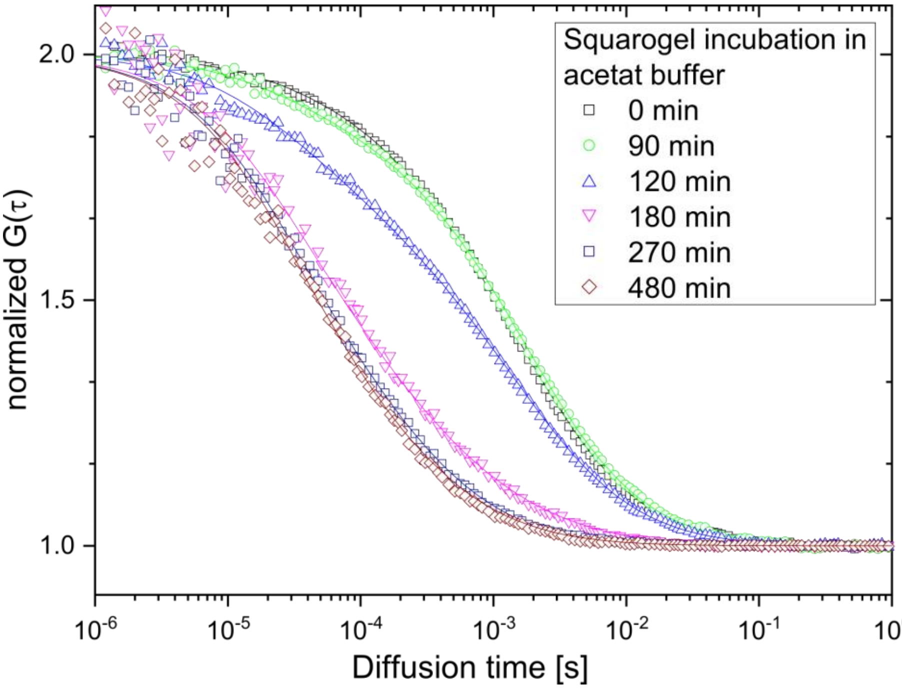

Figure 22: Monitoring of the degradation of the squarogel NCs followed by FCS measurements in an acidic environment (pH = 5.2) over a total time of 480 min. Adapted and reprinted with permission from J. Am. Chem. Soc. 2021, 143, 9872−9883; https://doi.org/10.1021/jacs.1c03772. Copyright 2019 American Chemical Society.

The autocorrelation functions shown in Figure 22 were either fitted with a two-component fit (equation 8, $m = 2$) reflecting a free dye fraction and the squarogel NC or a three-component fit (equation 8, $m = 3$). The third component and its origin will be discussed below. Within the first 90 min, no change in the detected diffusion time and the related hydrodynamic radius could be observed. First changes in the size, related to the degradation of the NCs, could be observed after 120 min. The ongoing degradation process and the associated decrease in the hydrodynamic radius could be observed until 270 min. During the incubation experiment, the calculated hydrodynamic radius of the NCs decreased from $R_{\mathrm{H,\,0\,min}} \approx 41$ nm to $R_{\mathrm{H,\,270\,min}} \approx 17$ nm. Even after one day of incubation under acidic conditions, no further change in the NC radius could be observed, indicating that no further degradation takes place. The degradation of the squarogel NC leads to the situation that the autocorrelation curves upwards of 270 min could not be well fitted with a two-component fit. Therefore, the third component was introduced to account for an increasing fraction of a third component. The third component could be identified as the respective building block, the unimer. The recorded diffusion time corresponds to a hydrodynamic radius of $R_{\mathrm{H,\,unimer}} = 5 \pm 1$ nm, and was confirmed through independent measurements with the unimer.

After observing the degradation of the pH-responsive crosslinking, the stability in PBS buffer, human blood plasma, human blood, and mouse blood was investigated. In Figure 23A normalized FCS autocorrelation curves are shown in PBS buffer (blue), human blood plasma (black), and heparin-treated human blood (red), whereas Figure 23B shows typical normalized FCS autocorrelation curves for the NCs incubated in mouse blood.

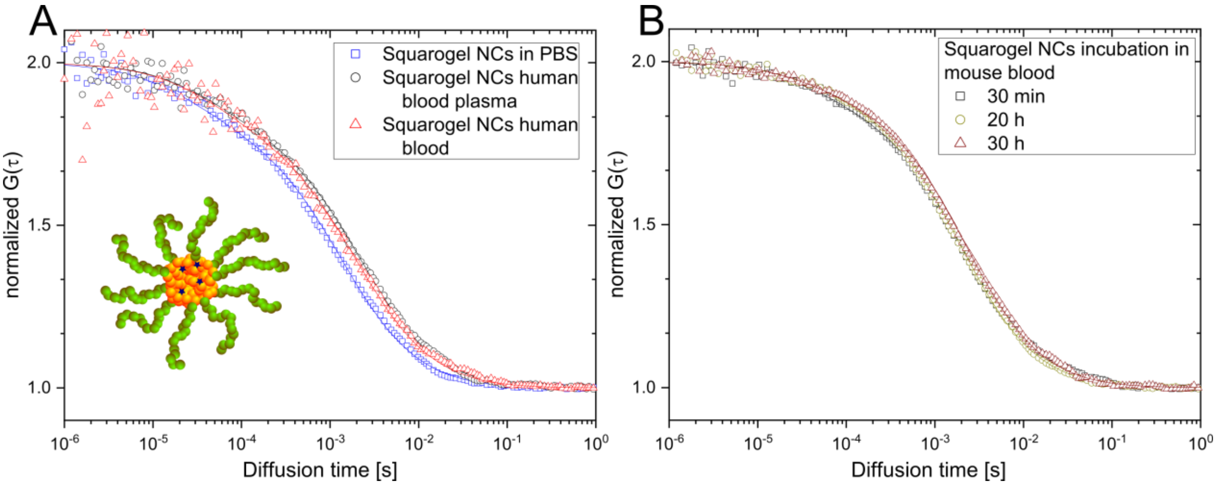

Figure 23: Squarogel NCs incubation in different media, including human blood and mouse blood. A) Normalized autocorrelation curves of the squarogel NCs in PBS (blue symbols), human blood plasma (black symbols), and heparin-treated human blood (red symbols). B) Normalized autocorrelation curves of incubation experiments of the squarogel NC in mouse blood for a total time of 30 h. Reprinted and adapted from Biomacromolecules 2019, 20, 3786−3797; https://doi.org/10.1021/acs.biomac.9b00868. Copyright 2019 American Chemical Society.

For all three sets of experiments in Figure 23A, the NCs were incubated for 30 min in the respective media. Fitting of the curves was done with a two-component fit (equation 8, $m = 2$) to obtain the respective diffusion time of the NCs and to account for a free dye fraction (~ 20 %). In PBS the NCs possess a diffusion time of $\tau_{\mathrm{PBS}} = 1400 \pm 60$ µs, in human blood plasma $\tau_{\text{plasma}} = 2200 \pm 160$ µs, and in human blood, $\tau_{\text{blood}} = 2100 \pm 250$ µs. With these diffusion times and accounting for the viscosity change in human blood plasma and human blood, the respective hydrodynamic radius could be calculated to $R_{\text{H, PBS, NCs}} = 32 \pm 3$ nm, $R_{\text{H, NCs, plasma}} = 33 \pm 3$ nm, and $R_{\text{H, NCs, blood}} = 31 \pm 4$. Further, the average number of particles in the observation volume during the FCS experiments was similar for PBS, human blood plasma, and human blood. This indicates that the plasma separation membrane does not affect the NCs by their passage through the membrane, in regards to the concentration or inducing degradation or aggregation. Another observation from these measurements is, that the NCs show no change in their hydrodynamic radius if measured in blood plasma or whole blood. This was also demonstrated in previous experiments by poor uptake by phagocytes and other cells, and long circulation times in the blood stream.[19]

The next step was to evaluate the properties of the NCs in mouse blood and observe the stability of the NCs during incubation experiments. Therefore, the NCs were incubated at 4 °C in heparin-treated mouse blood for a total time of 30 hours. Normalized FCS autocorrelation curves after 30 min, 20 h, and 30 h of incubation time are shown in Figure 23B. A two-component fit was necessary to properly fit the obtained autocorrelation curves. A fast component identified as freely diffusing OregonGreen 488 dye and a slow component identified as NC was present in the sample. During the incubation experiments, the diffusion time was yielded to $\tau_{30\text{ min}} = 2117 \pm 250$ µs and after 30 h to $\tau_{30\text{ h}} = 2288 \pm 250$ µs. The hydrodynamic radius could then be calculated to $R_{\text{H, 30min}} = 30 \pm 4$ nm, and $R_{\text{H, 30h,}} = 30.8 \pm 3$ nm. The stable hydrodynamic radius over 30 hours proves the stability of the NCs in whole blood over longer periods and indicates that no degradation or loss of cargo happens during the 30 hours of incubation in mouse blood.

4.3.3. Monitoring the Fate of Squarogel Nanocarrier in Live Mouse

For proving the applicability of the newly developed blood measurement approach, the previously tested and characterized NCs were injected into living mice. 8-10-week-old female BALB/c mice (body weight ~ 20-25 g) were injected with 100 µL of a 2 mg mL^{-1} NCs solution in PBS buffer. Further, two independent mice were injected with non-crosslinked polymers (unimer). After injection of the NCs or unimers small blood samples (~ 50 µL) were taken after 0, 6, 24, and 72 h via puncture of the submandibular vein. The blood samples were collected in heparin-coated Eppendorf vials to stabilize the samples against coagulation. FCS measurements were conducted within 1 h after blood collection. Figure 24A schematically shows the procedure and Figure 24B typical normalized FCS autocorrelation curves obtained from the blood measurements.

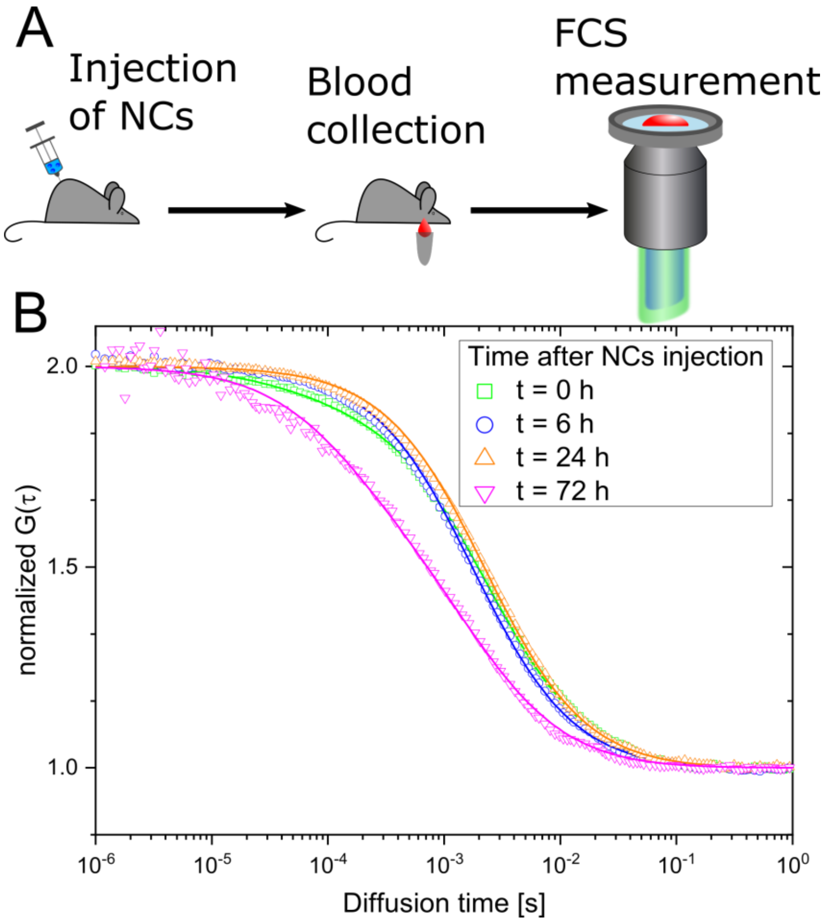

Figure 24: Following the fate of NCs after injection into live mice. A) Schematic overview of the procedure for following the fate of NCs in live mice. Illustrated is, from left to right, the injection, blood collection, and FCS measurement. B) Normalized FCS autocorrelation curves obtained from blood measurements after 0, 6, 24, and 72 h after NCs injection. Reprinted and adapted from Biomacromolecules 2019, 20, 3786−3797; https://doi.org/10.1021/acs.biomac.9b00868. Copyright 2019 American Chemical Society.

The kinetic of the NCs stability during circulation in the blood vessel system of live mice is shown in Figure 24B. The recorded curves after 0 h and 72 h were fitted with a two-component fit (equation 8, $m = 2$), whereas the recorded curves at 6 h and 24 h are fitted with a one-component fit (equation 8, $m = 1$). Due to a fast decay of the 0 h sample, a two-component fit was necessary to consider the fast component present in the sample. The fast component could be identified as non-bound OregonGreen 488 dye, which was still present even after several washing steps before the injection of the NCs. The slower component could be identified as the NCs. In difference, the recorded autocorrelation curves after 6 h and 24 h possess only a slow component and could be well fitted using a one-component fit. Species smaller than 5 nm, such as free dye molecules, are rapidly cleared from the blood vessel system by the kidney.[13] In the 6 h and 24 h samples, only a slow component could be observed, which is generated by the NCs. This confirms the rapid clearance of the small species, namely the unbound OregonGreen 488 dye, from the blood vessel system. From the first three samples (0, 6, and 24 h after NC injection) the diffusion time and the respective hydrodynamic radius of the NC remain unaffected by the blood and the circulation in the blood vessel system. The hydrodynamic radius of the NC could be calculated for the first three samples (0, 6, and 24 h) to $R_{\mathrm{H,\,NCs,\,mouse}} = 33 \pm 3$ nm. The unchanged hydrodynamic radius within the first 24 h indicated that neither aggregation nor degradation of the NCs occurred inside the blood vessel system of the mouse. Further, the average number of particle N remains unchanged within the first 24 h (see Figure 25D, open symbols), indicating indirectly that no NCs stick to blood cells or are endocytosed by macrophages or monocytes. However, partial degradation of the NCs could be observed 72 h after injection of the NCs. The degradation process causes a shift of the autocorrelation curve to smaller lag times (compare Figure 24B, magenta curve). For properly fitting the autocorrelation curve measured after 72 hours it was necessary to use a two-component fit. With the two diffusion times, the hydrodynamic radius can be calculated for the fast species and the slower species. The hydrodynamic radius for the slow fluorescent species was calculated to $R_{\mathrm{H,\,NCs,\,mouse,\,72h}} = 24 \pm 2$ nm (see Figure 25B), and the hydrodynamic radius of the species with the fast diffusion time to $R_{\mathrm{H,\,fast\,component,\,72\,h}} = 5 \pm 1$ nm. The occurrence of the fast component after 72 h with a hydrodynamic radius of 5 nm and the decreased hydrodynamic radius of the NCs indicates that the fast component arises from the respective building blocks of the NCs the unimer. The unimers originated from the degradation of the ketal crosslinks inside the NCs, similar to the observed degradation of the NC under acidic environments (see section 4.3.2). The hydrolysis of the ketal crosslinks inside the squarogel and with this the associated degradation of the NC leads to the freely unimers inside the blood vessel system. The degradation of the NCs leads to an increase of the overall number of fluorescent species present in the blood vessel system of the mouse (see Figure 25D, open symbols) and is also reflected by the respective fraction of the unimer and NCs (see Figure 25C). Within the first 24 h, the fraction of the NCs remains unchanged at around 100 % but decreases after 72 h to around 40 %. As a result, the unimer fraction is increasing with progressive degradation of the NCs and is increasing after 72 h to around 60 %. Additionally, these measurements allow estimating the loading efficiency of the OregonGreen 488 dye as a model for drug cargo. The estimation is shown in Figure 25D as dye per NC in green star symbols. Note that the estimation of the loading efficiency is an average value obtained from three independent sets of mouse experiments. The data indicates that the NCs were loaded on average with 7-8 cargo molecules. These loaded molecules remain at the NCs within the first 24 h of circulation in the blood stream. A decrease of loaded molecules could only be observed after 72 h of circulation time in the mouse. These values should be considered carefully, due to the slightly lower signal-to-noise ratio during the blood measurements. Blood possesses an autofluorescence of around 10 % of the total measured fluorescence intensity and at 0 h and 72 h, other species were present, like free dye and the unimer. This can lead to an over- or underestimation of the dye loading.

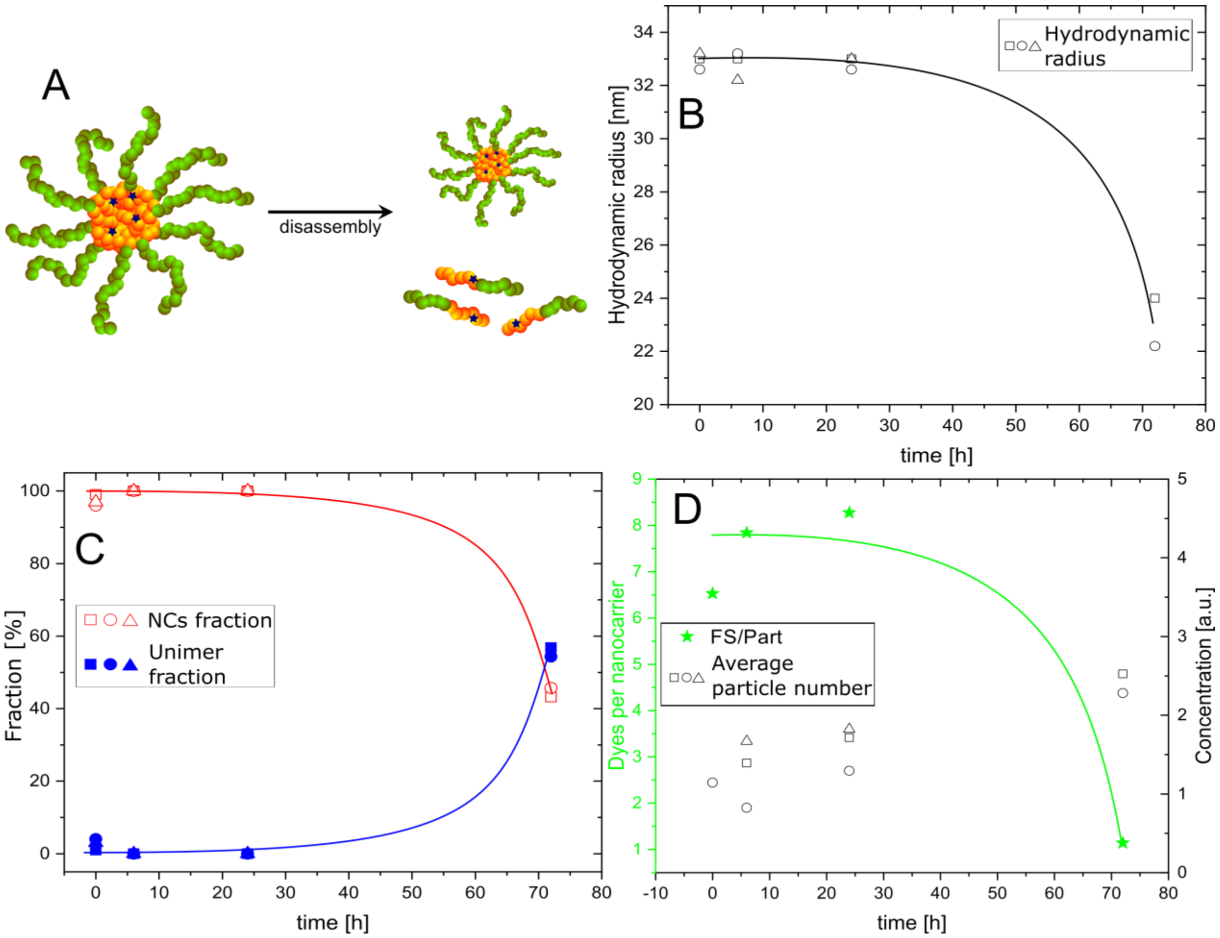

Figure 25: Overview of the results from the mice experiments obtained through blood FCS measurements. The presented results in B)-D) were obtained from three independent sets of mouse experiments represented by three different symbols: circle, square, and triangle. Each symbol stands for one mouse experiment. A) Schematic overview of the degradation process of the squarogel NCs. B) Calculated hydrodynamic radius obtained from three independent sets of mouse experiments. C) Fraction of the NCs (open red symbols) and the unimer fraction (closed blue symbols), and D) Dye per particle (green stars) and the overall concentration (open black symbols). The lines in the graphs B-D) are a guide to the eye. Reprinted and adapted from Biomacromolecules 2019, 20, 3786−3797; https://doi.org/10.1021/acs.biomac.9b00868. Copyright 2019 American Chemical Society.

Everything considered, 72 h after NCs injection into a living mouse the NCs are still circulating inside the blood vessel system and only partially degraded. The degradation was proven by measuring a smaller radius for the NCs and a second species of around $R_{\mathrm{H,\,unimer}} = 5$ nm.

Interestingly, these small species of around 5 nm are not cleared fully from the blood vessel system. To further investigate these findings, unimers were injected into the blood stream of a mouse. The normalized autocorrelation curves recorded after 6, 24, and 72 h after injection are shown in Figure 26.

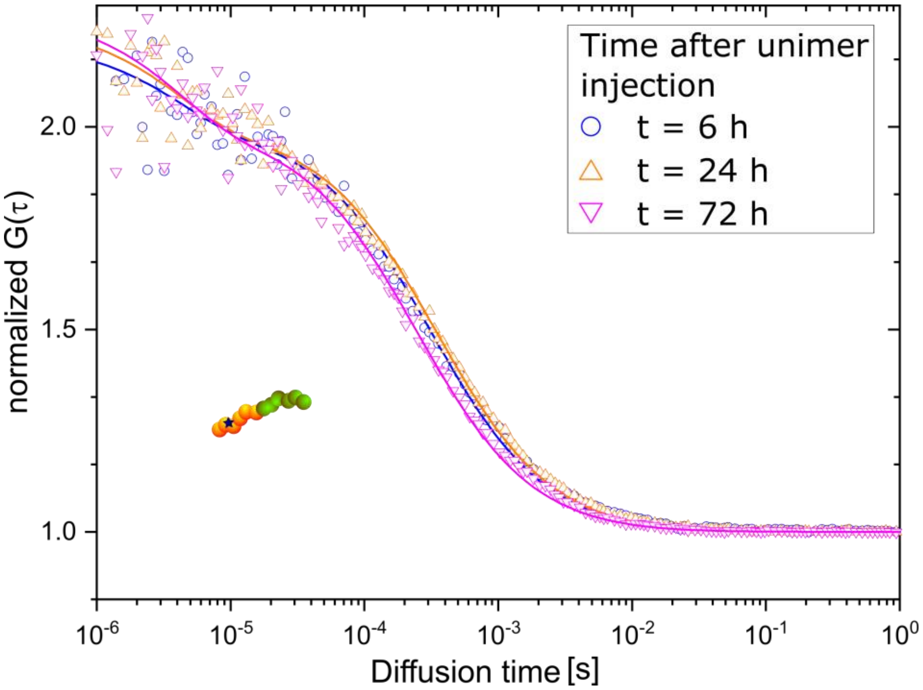

Figure 26: Monitoring the fate of non-crosslinked unimers during the circulation in the blood stream of a live mouse. Normalized autocorrelation curves were recorded after 6 h (blue symbols), 24 h (orange symbols), and 72 h (magenta symbols) after injection. Reprinted and adapted from Biomacromolecules 2019, 20, 3786−3797; https://doi.org/10.1021/acs.biomac.9b00868. Copyright 2019 American Chemical Society.

The diffusion times obtained from the 6, 24, and 72 h measurements are almost identical and were yielded to $\tau_{\text{unimer, mouse}} \approx 300 \pm 30$ µs. The diffusion time corresponds to a hydrodynamic radius of $R_{\text{H, unimer, mouse}} = 5.1 \pm 1$ nm. This finding is similar to the hydrodynamic radius obtained from PBS measurements $R_{\text{H, unimer, PBS}} = 5.8 \pm 1$ nm. These values indicate that the unimers are still circulating in the blood vessel system of the mouse, even after 72 h. The long circulation time of the unimers can only be explained by the high degree of PEGylation of the hydrophilic block copolymers.[169, 170]

The degradation of the NCs could be induced by different factors, such as the shear forces in the blood vessel system or the elevated temperature in comparison to normal storage conditions. Therefore, to fully understand this partial degradation of the squarogel NCs an incubation experiment over 72 h was conducted to exclude the influence of the shear forces on the degradation process. The squarogel NCs were incubated in either human blood, human blood plasma, or PBS buffer at both 4 °C and 37 °C. FCS measurements were conducted over a time range of 72 h, similar to the animal experiments (Figure 27).

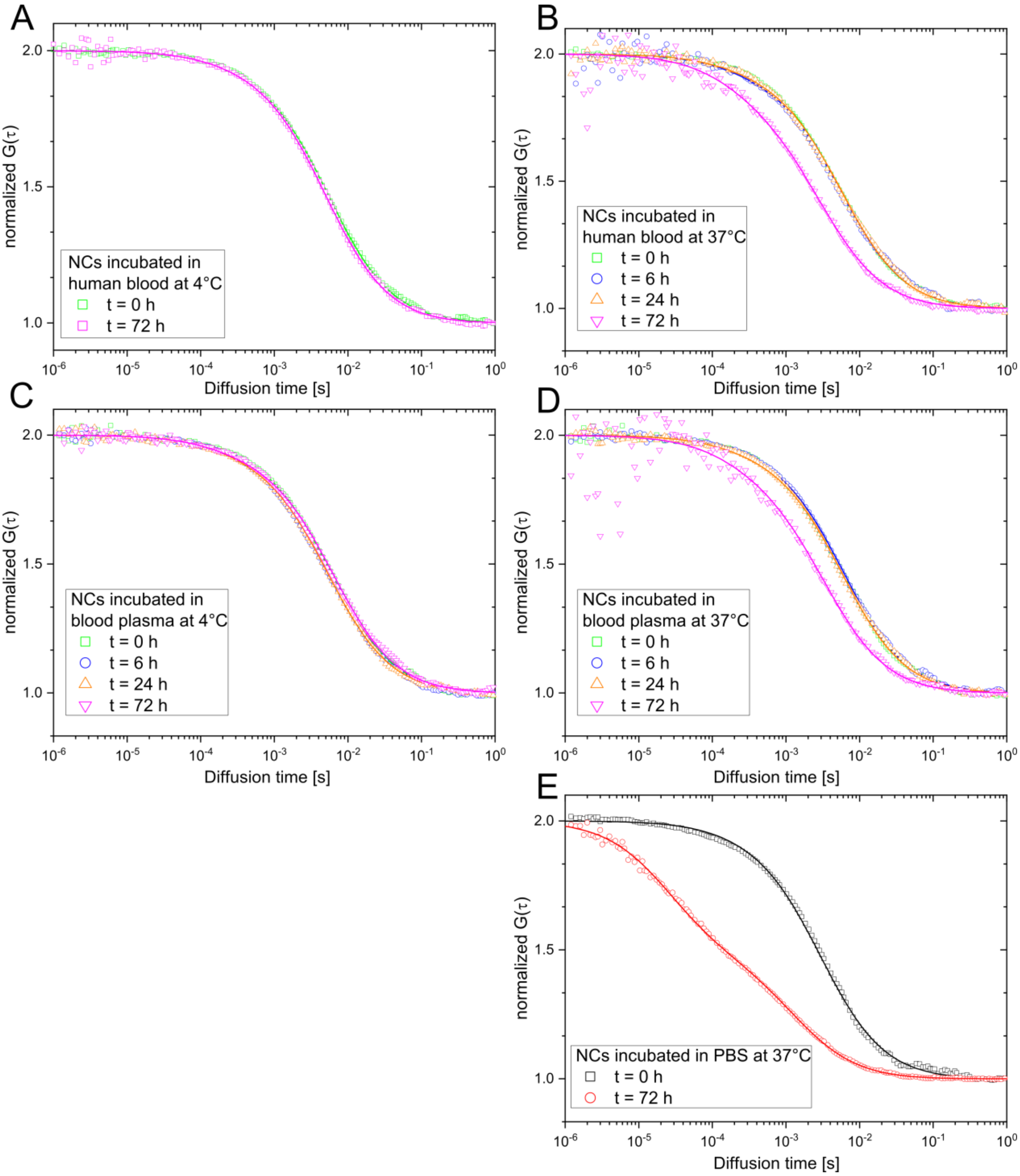

Figure 27: Normalized autocorrelation curves recorded during the incubation experiments of the squarogel NCs in either human blood, human blood plasma, or PBS buffer, at 4 °C and 37 °C. A) NCs in human blood at 4 °C and B) at 37 °C. C) NCs incubated in human blood plasma at 4 °C and D) at 37 °C. E) NCs incubated in PBS buffer at 37 °C. Reprinted and adapted from Biomacromolecules 2019, 20, 3786−3797; https://doi.org/10.1021/acs.biomac.9b00868. Copyright 2019 American Chemical Society.

In both media, human blood and human blood plasma, the NCs possess high stability at 4 °C over the whole observed time range of 72 h (Figure 27A and C). A similar trend is observed for the NCs in all three media within the first 24 h at 37 °C. The recorded autocorrelation curve after 72 h at 37 °C showed that the NCs are degraded (Figure 27B, D, and E). The recorded autocorrelation curve after 72 h in human blood and human blood plasma possesses a similar trend like the autocorrelation curve recorded during the life mouse model after 72 h (compare Figure 24). Interestingly, the NCs undergo also in PBS buffer a partial degradation process and not only in human blood and human blood plasma. This indicates that the ketal crosslinks provide sufficient stability under physiological pH and temperature within 24 hours. Only after 24 h, ketal crosslinks do undergo partial disassembly. The instability of the ketal group in aqueous environments is related to the hydrolytic sensitivity at 37 °C in PBS and during the blood circulation in live mice.

4.4. Summary and Outlook

In conclusion, a new approach has been developed to enable FCS measurements in whole blood, which allows following the fate of squarogel NCs injected into living mice. Advantageous of this method is the need for only a small amount of blood volume (~ 50 µL) and no need for further sample treatment before the measurement. During the circulation of the NCs in living mice, it was possible to monitor the size and the loaded cargo molecules for a total time range of 72 h. Besides the size and drug loading in the form of an OregonGreen 488 dye, following the concentration increase of the fluorescent species in the undiluted whole blood after the partial degradation of the sample was possible with the presented approach. These types of experiments can be performed with commercial FCS equipment and common fluorophores with any excitation wavelength reaching from the visible up to the near-infrared wavelength range.

It was further possible to quantify the stability of the ketal crosslinking in the nanogel system after intravenous injection and *in vitro* at 37 °C with incubation experiments. During the circulation experiments, the clearance of small non-conjugated dye molecules from the blood vessel system in less than 6 h could be observed. The NCs were stable within the first 24 h and only after 72 h a degradation process could be monitored with FCS measurements. This leads to an increase of fluorescent species in form of the unimer. These unimers were not cleared from the blood vessel system and this was further supported by independent injection of unimer in live mice.

This approach enables the accurate and quantitative monitoring of the fate of NCs with FCS in small drop samples (~ 50 µm). It provides new opportunities to follow the NCs during blood circulation and can contribute towards the development of more advanced NC-based therapeutics. The possibility to use dyes over the whole spectral range, from 400 nm up to the near-infrared range enables to follow the fate of the NCs inside the blood stream and the utilization of common monitoring techniques like fluorescence imaging. The combination of the newly developed FCS blood measurement approach and commonly used techniques to monitor NCs *in vivo* can contribute toward a broad understanding of the drug delivery process and the optimization of suitable NCs for immunodrug delivery processes.

5. Chapter: FCS Analysis for Cooperation Projects of the Collaborative Research Center1066

In the following chapter FCS experiments are presented that were performed in the framework of various cooperation between the sub-project Q2 “Optical methods to study endocytosis, intracellular trafficking, and cargo release” and other sub-projects, as a part of the collaborative research center (CRC) 1066 “Nanodimensional polymer therapeutics for tumor therapy”. Within the CRC1066 the Q-projects are the bridge between the A-projects and B-projects and are mainly focused on characterization. The A-projects deal with NCs development, whereas the B-projects are focusing on the application of the developed NCs for tumor immunotherapy. In these cooperations, FCS was utilized to study various polymer-based NC systems by monitoring diffusion times, hydrodynamic radii, stability in different solvents, and to monitor reaction kinetics. The following sections present the publications which arise from the cooperation projects and give a brief description of how FCS experiments help to characterize the polymer-based systems in these publications.

5.1. HPMA-Based Nanoparticles for Fast, Bioorthogonal iEDDA Ligation

In this study[79], the click reaction between 1,2,4,5-tetrazines with trans-cyclooctene was observed with FCS. The tetrazine unit was introduced to an amphiphilic copolymer made of 2-Hydroxypropylmethacrylat. The copolymer was used to form polymeric micelles covered with tetrazine groups (Figure 28A). To the core-cross-linked micelles, carrying the tetrazine groups, was then an antibody added, carrying a trans-cyclooctene, and the reaction between the tetrazine and the trans-cyclooctene was observed with FCS in buffer and human blood plasma (Figure 28). To follow the reaction with FCS the trans-cyclooctene antibody was labeled with the NIR-dye CW800 and the size increase was monitored. The binding of the trans-cyclooctene antibody to the micelle after the click reaction was accompanied by an increase in the hydrodynamic radius. Figure 28B shows typical normalized FCS autocorrelation function of the antibody (black symbols), the click reaction products in PBS (green symbols), and in blood plasma (blue symbols). The calculated hydrodynamic radius increased from 7 nm to 13 nm after the click reaction. In Figure 28C the fraction of the unbound antibody (black symbols) and the product of the click reaction (red symbols) are illustrated. The fractions were yielded from a two-component fit of the autocorrelation curves from Figure 28B. The yielded fractions from the analysis of the autocorrelation curves indicate that within 10 min around 80 % of the antibody had bound to the micelle.

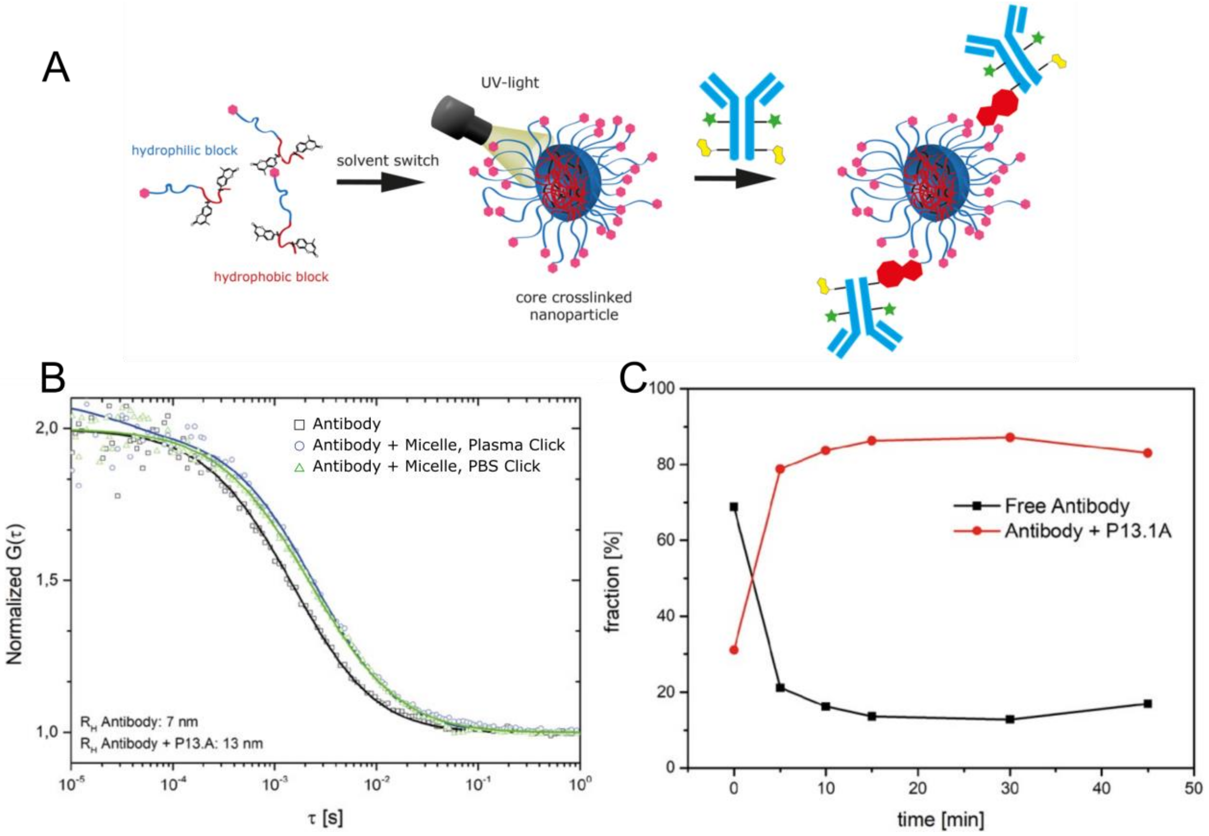

Figure 28: A) Schematic overview of the preparation of the particle with subsequently crosslinking and click reaction. B) Typical normalized autocorrelation curves of the antibody (black symbols), antibody + micelle in PBS (green symbols), and antibody + micelle in blood plasma (blue symbols). The measurements were recorded after incubating the antibody and the micelle for 1 h in the respective solvent. C) Evolution of the fraction from the free antibody (black symbols) and the click reaction product (red symbols) versus incubation time in blood plasma. The fractions were obtained from a two-component fit of the autocorrelation curves shown in B). Reprinted with permission from Biomacromolecules 2019, 20, 3786−3797; https://doi.org/10.1021/acs.biomac.9b00868. Copyright 2019 American Chemical Society.

This work “HPMA-Based Nanoparticles for Fast, Bioorthogonal iEDDA Ligation” was published in 2019 in the journal Biomacromolecules (2019, 20, 3786-3797; https://doi.org/10.1021/acs.biomac.9b00868) as a cooperation project of the CRC1066 together with Stefan Kramer, Dennis Svatunek, Irina Alberg, Barbara Grafen, Sascha Schmitt, Lydia Braun, Arthur H. A. M. van Onzen, Raffaella Rossin, Kaloian Koynov, Hannes Mikula, and Rudolf Zentel.

5.2. Core Cross-Linked Polymeric Micelles for Specific Iron Delivery: Inducing Sterile Inflammation in Macrophages

In this project[171] iron oxide nanoparticles were encapsulated in a polymeric micelle. These micelles were then delivered to macrophages to induce sterile inflammation. The micelles consist of polysarcosine-*block*-poly(*S*-ethylsulfonyl-L-cysteine) and were further functionalized to yield glutathione-responsive core cross-linked polymeric micelles. FCS experiments help to characterize these micelles in regards to the hydrodynamic radius and estimation of unbound dye (Figure 29). The hydrodynamic radius of the micelles was calculated for the micelle without encapsulated iron oxide to $R_{\text{H, micelle}} = 47$ nm and for the micelle with iron oxide to $R_{\text{H, micelle + iron oxide}} = 72$ nm. The autocorrelation curves in Figure 29 were fitted using a one-component fit, confirming that no unbound dye fraction was present.

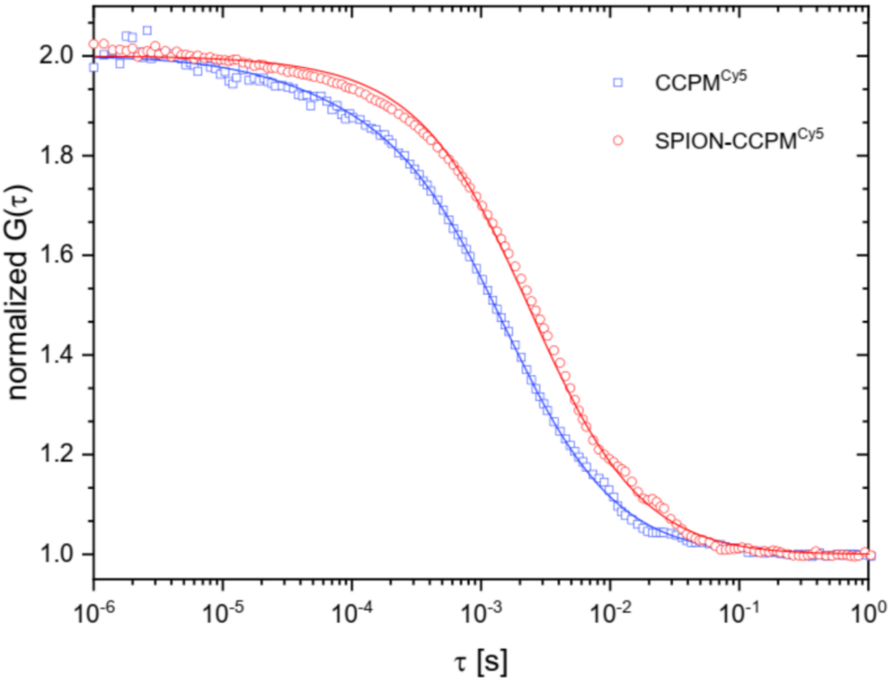

Figure 29: Normalized FCS autocorrelation curves of iron oxide carrying micelles (red symbols) and micelles without iron oxide (blue symbols) labeled with Cy5 measured in PBS buffer. The applied one-component fit (equation 8; $m = 1$) confirmed the absence of an unbound dye fraction. Reprinted with permission from Adv. Healthcare Mater. 2021, 2100385; https://doi.org/10.1002/adhm.202100385. Copyright 2021 Advanced Healthcare Materials published by Wiley-VCH GmbH.

This work “Core Cross-Linked Polymeric Micelles for Specific Iron Delivery: Inducing Sterile Inflammation in Macrophages” was published in 2021 in the journal Adv. Healthcare Mater (2021, 2100385; https://doi.org/10.1002/adhm.202100385) as a cooperation project of the CRC1066 together with Tobias A. Bauer, Natalie K. Horvat, Oriana Marques, Sara Chocarro, Christina Mertens, Silvia Colucci, Sascha Schmitt, Luca M. Carrella, Svenja Morsbach, Kaloian Koynov, Federico Fenaroli, Peter Blümler, Michaela Jung, Rocio Sotillo, Matthias W. Hentze, Martina U. Muckenthaler, and Matthias Barz.

5.3. Squaric Ester-Based, pH-Degradable Nanogels: Modular Nanocarriers for Safe, Systemic Administration of Toll-like Receptor 7/8 Agonistic Immune Modulators

This publication[19] deals with pH-responsive nanogels serving as drug nanocarriers for delivering TLR7/8-stimulating imidazoquinolines. Herefore, squaric ester amide block copolymers were used, which self-assemble into precursor micelles (Figure 30A). Their cores consist of amine-reactive groups, which can be reacted with dyes, crosslinkers, or imidazoquinolines. Figure 30B1 illustrates recorded normalized FCS autocorrelation in human blood plasma to investigate the hydrodynamic radius and stability of the pH-responsive nanogel over a total time range of 24 h. Further, Figure 30B2 shows FCS autocorrelation curves following the degradation of the pH-responsive cross-linking under acidic conditions over a total time of 480 min.

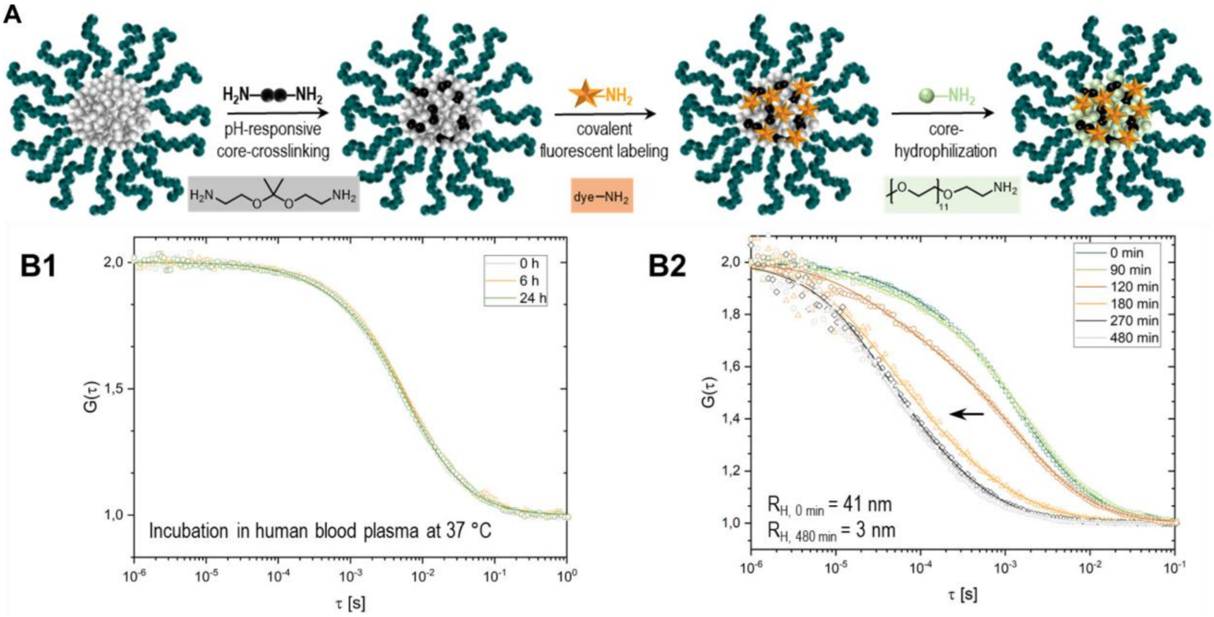

Figure 30: A) Schematic overview of the particle preparation. B1) Normalized FCS autocorrelation curves of incubated OregonGreen 488 labeled nanogels in an acidic environment (pH = 5.2) for a total time span of 480 min. B2) Normalized FCS autocorrelation curves of OregonGreen 488 labeled nanogels in human blood plasma after 0, 6, and 24 h incubation at 37 °C. Reprinted with permission from J. Am. Chem. Soc. 2021, 143, 9872−9883; https://doi.org/10.1021/jacs.1c03772. Copyright 2019 American Chemical Society.

This work “Squaric Ester-Based, pH-Degradable Nanogels: Modular Nanocarriers for Safe, Systemic Administration of Toll-like Receptor 7/8 Agonistic Immune Modulators” was published in 2021 in the journal J. Am. Chem. Soc. (2021, 143, 9872-9883; https://doi.org/10.1021/jacs.1c03772) as a cooperation project of the CRC1066 together with Anne Huppertsberg, Leonard Kaps, Zifu Zhong, Sascha Schmitt, Judith Stickdorn, Kim Deswarte, Francis Combes, Christian Czysch, Jana De Vrieze, Sabah Kasmi, Niklas Choteschovsky, Adrian Klefenz, Carolina Medina-Montano, Pia Winterwerber, Chaojian Chen, Matthias Bros, Stefan Lienenklaus, Niek N. Sanders, Kaloian Koynov, Detlef Schuppan, Bart N. Lambrecht, Sunil A. David, Bruno G. De Geest, and Lutz Nuhn.

5.4. pH-Degradable, Bisphosphonate-Loaded Nanogels Attenuate Liver Fibrosis by Repolarization of M2-type Macrophages

The following study[172] deals with pH-degradable squaric ester-based nanogel as an NC system to deliver bisphosphonate alendronate for the repolarization of macrophages. The delivery of bisphosphonate alendronate should reprogram profibrotic M2 towards antifibrotic M1-type macrophages. FCS experiments were conducted to evaluate the stability of the alendronate-loaded pH-degradable squaric ester-based NCs in human blood plasma (Figure 31). The alendronate-loaded NCs were incubated for a total time range of 24 h and FCS experiments confirmed the stability of the NC by detecting an unchanged hydrodynamic radius of R_H = 55 nm.

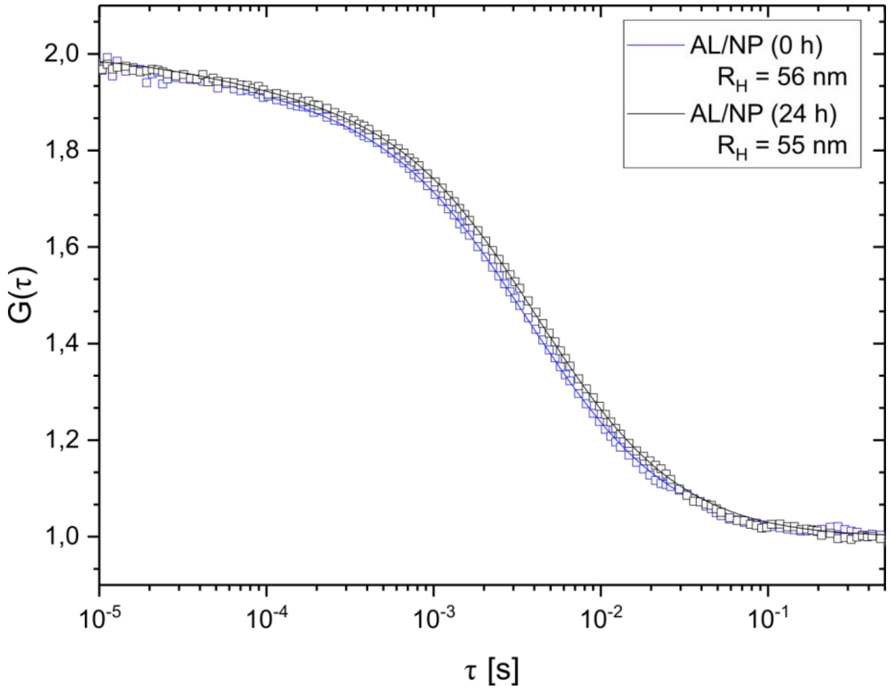

Figure 31: Normalized FCS autocorrelation curves of nanogel NC loaded with alendronate in human blood plasma incubated for a total time span of 24 h. Reprinted with permission from PNAS 2022 Vol. 119 No. 12; https://doi.org/10.1073/pnas.2122310119. Copyright 2022 by PNAS.

This work “pH-degradable, bisphosphonate-loaded nanogels attenuateliver fibrosis by repolarization of M2-type macrophages” was published in 2022 in the journal PNAS (2022, 119, No. 12; https://doi.org/10.1073/pnas.2122310119) as a cooperation project of the CRC1066 together with Leonard Kaps, Anne Huppertsberg, Niklas Choteschovsky, Adrian Klefenz, Feyza Durak, Babara Schrörs, Mustafa Diken, Emma Eichler, Sebastian Rosigkeit, Sascha Schmitt, Christian Leps, Alicia Schulze, Friedrich Foerster, Ernesto Bockamp, Bruno G. De Geest, Kaloian Koynov, Hans-Joachim Räder, Stefan Tenzer, Federico Marini, Detlef Schuppan, and Lutz Nuhn.

6. Concluding Remarks

In this thesis, two different experimental approaches were presented regarding the characterization of polymer-based nanocarriers. The first part concentrates on the monitoring of the formation process of nanoparticles with two different approaches, whereas the second part was concentrating on the characterization of nanocarriers in whole blood samples. For both approaches, the fluorescence correlation spectroscopy (FCS) technique was utilized to observe polymeric nanoparticles related to the drug delivery process.

Chapter 3 monitored the formation process of nanoparticles during the solvent evaporation from emulsion droplets and the miniemulsion polymerization reaction. Here, two fluorescence-based techniques were combined to monitor the formation process of nanoparticles. Time-correlated single-photon counting (TCSPC) was combined with FCS to monitor the transition from the initial liquid nanodroplet to the final particle dispersion and simultaneously track the size evolution of the nanodroplets. Therefore, a tailored fluorescent molecular rotor was embedded inside the nanodroplets as a reporter to track local environment changes during both reactions. The presented results in Chapter 3 demonstrated that the combination of the TCSPC and FCS technique is suitable to monitor the formation process of nanoparticles. In all measurements, two distinguishable fluorescence lifetimes were recorded. These lifetimes could be attributed to a solvent-rich and polymer-rich region. This approach can be further extended to study more complex formation processes, e.g. monitoring the phase separation during the synthesis of nanocapsules or the phase separation between polymer blocks during the formation of block copolymer nanoparticles.

Chapter 4 presented a newly developed approach for FCS measurements in small whole blood samples. For realizing the approach a plasma separation membrane was utilized to prevent the blood cells to enter the detection volume during the recording of FCS autocorrelation curves. The developed approach was able to follow the fate of squarogel nanocarriers injected into living mice. By collecting small amounts of blood after pre-defined time points, it was possible to monitor the nanocarrier in these blood samples up to 72 hours after injection. These studies revealed a degradation process of the squarogels nanocarrier after 24 h inside the blood stream, due to the hydrolysis of the ketal crosslinking. This finding was further supported by independently conducted incubation experiments at 37 °C in human blood. The presented approach shows the potential to follow nanocarriers during their circulation in living mice or patients regarding their stability, premature drug release, and aggregation behavior. The approach is not limited to a specific spectral range and can also measure nanocarriers labeled with NIR dyes. This opens the possibility to combine the presented approach with other techniques relying on NIR dyes, like NIR imaging. The combination of different characterization techniques can lead to a broader understanding of the drug delivery process and can help to develop more efficient nanocarriers.

The whole thesis is centered around polymeric nanoparticles. Due to their small size, polymeric nanoparticles possess different properties than their respective bulk materials. This difference makes them interesting for many applications, especially the application as nanocarriers. Here, two different approaches are presented which contribute toward a broader understanding of the synthesis of polymeric nanoparticles, which can be used as nanocarriers, and their characterization in whole blood. A broad understanding in these fields contributes to the synthesis of more efficient nanocarriers for treating different diseases.

7. Bibliography

1. Namazi, H., Polymers in our daily life. *Bioimpacts* **2017,** *7* (2), 73-74.
2. Chow, P. C. Y.; Someya, T., Organic Photodetectors for Next-Generation Wearable Electronics. *Adv Mater* **2020,** *32* (15), e1902045.
3. Ashizawa, M.; Zheng, Y.; Tran, H.; Bao, Z., Intrinsically stretchable conjugated polymer semiconductors in field effect transistors. *Progress in Polymer Science* **2020,** *100* (101181).
4. Cheng, X.; Pan, J.; Zhao, Y.; Liao, M.; Peng, H., Gel Polymer Electrolytes for Electrochemical Energy Storage. *Advanced Energy Materials* **2018,** *8* (7).
5. Teo, A. J. T.; Mishra, A.; Park, I.; Kim, Y. J.; Park, W. T.; Yoon, Y. J., Polymeric Biomaterials for Medical Implants and Devices. *ACS Biomater Sci Eng* **2016,** *2* (4), 454-472.
6. Alqurashi, H.; Khurshid, Z.; Syed, A. U. Y.; Rashid Habib, S.; Rokaya, D.; Zafar, M. S., Polyetherketoneketone (PEKK): An emerging biomaterial for oral implants and dental prostheses. *J Adv Res* **2021,** *28*, 87-95.
7. Bilal, M.; Iqbal, H. M. N., Naturally-derived biopolymers: Potential platforms for enzyme immobilization. *International Journal of Biological Macromolecules* **2019,** *130*, 462-482.
8. Rostami, M. R.; Yousefi, M.; Khezerlou, A.; Mohammadi, M. A.; Jafari, S. M., Application of different biopolymers for nanoencapsulation of antioxidants via electrohydrodynamic processes. *Food Hydrocolloids* **2019,** *97* (105170).
9. Otto, D. P.; de Villiers, M. M., Why is the nanoscale special (or not)? Fundamental properties and how it relates to the design of nano-enabled drug delivery systems. *Nanotechnology Reviews* **2013,** *2* (2), 171-199.
10. Nasir, A.; Kausar, A.; Younus, A., A Review on Preparation, Properties and Applications of Polymeric Nanoparticle-Based Materials. *Polymer-Plastics Technology and Engineering* **2014,** *54* (4), 325-341.
11. Rao, J. P.; Geckeler, K. E., Polymer nanoparticles: Preparation techniques and size-control parameters. *Progress in Polymer Science* **2011,** *36* (7), 887-913.
12. Polymer Nanoparticles for Nanomedicines: A Guide for their Design, Preparation and Development. Christine Vauthier, G. P., Ed. Springer: 2016.
13. Petros, R. A.; DeSimone, J. M., Strategies in the design of nanoparticles for therapeutic applications. *Nat Rev Drug Discov* **2010,** *9* (8), 615-27.
14. Zhou, J.; Chizhik, A. I.; Chu, S.; Jin, D., Single-particle spectroscopy for functional nanomaterials. *Nature* **2020,** *579* (7797), 41-50.
15. Zielinska, A.; Carreiro, F.; Oliveira, A. M.; Neves, A.; Pires, B.; Venkatesh, D. N.; Durazzo, A.; Lucarini, M.; Eder, P.; Silva, A. M.; Santini, A.; Souto, E. B., Polymeric

Nanoparticles: Production, Characterization, Toxicology and Ecotoxicology. *Molecules* **2020,** *25* (16).

16. Liao, Z.; Wong, S. W.; Yeo, H. L.; Zhao, Y., Smart nanocarriers for cancer treatment: Clinical impact and safety. *NanoImpact* **2020,** *20*.

17. Walsh, E. E.; Frenck, R. W., Jr.; Falsey, A. R.; Kitchin, N.; Absalon, J.; Gurtman, A.; Lockhart, S.; Neuzil, K.; Mulligan, M. J.; Bailey, R.; Swanson, K. A.; Li, P.; Koury, K.; Kalina, W.; Cooper, D.; Fontes-Garfias, C.; Shi, P. Y.; Tureci, O.; Tompkins, K. R.; Lyke, K. E.; Raabe, V.; Dormitzer, P. R.; Jansen, K. U.; Sahin, U.; Gruber, W. C., Safety and Immunogenicity of Two RNA-Based Covid-19 Vaccine Candidates. *N Engl J Med* **2020,** *383* (25), 2439-2450.

18. Vogel, A. B.; Kanevsky, I.; Che, Y.; Swanson, K. A.; Muik, A.; Vormehr, M.; Kranz, L. M.; Walzer, K. C.; Hein, S.; Guler, A.; Loschko, J.; Maddur, M. S.; Ota-Setlik, A.; Tompkins, K.; Cole, J.; Lui, B. G.; Ziegenhals, T.; Plaschke, A.; Eisel, D.; Dany, S. C.; Fesser, S.; Erbar, S.; Bates, F.; Schneider, D.; Jesionek, B.; Sanger, B.; Wallisch, A. K.; Feuchter, Y.; Junginger, H.; Krumm, S. A.; Heinen, A. P.; Adams-Quack, P.; Schlereth, J.; Schille, S.; Kroner, C.; de la Caridad Guimil Garcia, R.; Hiller, T.; Fischer, L.; Sellers, R. S.; Choudhary, S.; Gonzalez, O.; Vascotto, F.; Gutman, M. R.; Fontenot, J. A.; Hall-Ursone, S.; Brasky, K.; Griffor, M. C.; Han, S.; Su, A. A. H.; Lees, J. A.; Nedoma, N. L.; Mashalidis, E. H.; Sahasrabudhe, P. V.; Tan, C. Y.; Pavliakova, D.; Singh, G.; Fontes-Garfias, C.; Pride, M.; Scully, I. L.; Ciolino, T.; Obregon, J.; Gazi, M.; Carrion, R., Jr.; Alfson, K. J.; Kalina, W. V.; Kaushal, D.; Shi, P. Y.; Klamp, T.; Rosenbaum, C.; Kuhn, A. N.; Tureci, O.; Dormitzer, P. R.; Jansen, K. U.; Sahin, U., BNT162b vaccines protect rhesus macaques from SARS-CoV-2. *Nature* **2021,** *592* (7853), 283-289.

19. Huppertsberg, A.; Kaps, L.; Zhong, Z.; Schmitt, S.; Stickdorn, J.; Deswarte, K.; Combes, F.; Czysch, C.; De Vrieze, J.; Kasmi, S.; Choteschovsky, N.; Klefenz, A.; Medina-Montano, C.; Winterwerber, P.; Chen, C.; Bros, M.; Lienenklaus, S.; Sanders, N. N.; Koynov, K.; Schuppan, D.; Lambrecht, B. N.; David, S. A.; De Geest, B. G.; Nuhn, L., Squaric Ester-Based, pH-Degradable Nanogels: Modular Nanocarriers for Safe, Systemic Administration of Toll-like Receptor 7/8 Agonistic Immune Modulators. *J Am Chem Soc* **2021,** *143* (26), 9872-9883.

20. Klymchenko, A. S.; Liu, F.; Collot, M.; Anton, N., Dye-Loaded Nanoemulsions: Biomimetic Fluorescent Nanocarriers for Bioimaging and Nanomedicine. *Adv Healthc Mater* **2021,** *10* (1), e2001289.

21. Motealleh, A.; De Marco, R.; Kehr, N. S., Stimuli-responsive local drug molecule delivery to adhered cells in a 3D nanocomposite scaffold. *Journal of Materials Chemistry B* **2019,** *7* (23), 3716-3723.

22. Deirram, N.; Zhang, C.; Kermaniyan, S. S.; Johnston, A. P. R.; Such, G. K., pH-Responsive Polymer Nanoparticles for Drug Delivery. *Macromol Rapid Commun* **2019,** *40* (10), e1800917.

23. Perrigue, P. M.; Murray, R. A.; Mielcarek, A.; Henschke, A.; Moya, S. E., Degradation of Drug Delivery Nanocarriers and Payload Release: A Review of Physical Methods for Tracing Nanocarrier Biological Fate. *Pharmaceutics* **2021,** *13* (6).

24. Crucho, C. I. C.; Barros, M. T., Polymeric nanoparticles: A study on the preparation variables and characterization methods. *Mater Sci Eng C Mater Biol Appl* **2017,** *80*, 771-784.

25. Silvestre, A. L. P.; Oshiro-Junior, J. A.; Garcia, C.; Turco, B. O.; da Silva Leite, J. M.; de Lima Damasceno, B. P. G.; Soares, J. C. M.; Chorilli, M., Monoclonal Antibodies Carried in Drug Delivery Nanosystems as a Strategy for Cancer Treatment. *Curr Med Chem* **2021,** *28* (2), 401-418.

26. Zhou, Q.; Zhang, L.; Yang, T.; Wu, H., Stimuli-responsive polymeric micelles for drug delivery and cancer therapy. *Int J Nanomedicine* **2018,** *13*, 2921-2942.

27. Din, F. U.; Aman, W.; Ullah, I.; Qureshi, O. S.; Mustapha, O.; Shafique, S.; Zeb, A., Effective use of nanocarriers as drug delivery systems for the treatment of selected tumors. *Int J Nanomedicine* **2017,** *12*, 7291-7309.

28. Wang, X.; Wang, Y.; Chen, Z. G.; Shin, D. M., Advances of cancer therapy by nanotechnology. *Cancer Res Treat* **2009,** *41* (1), 1-11.

29. Cabral, H.; Miyata, K.; Osada, K.; Kataoka, K., Block Copolymer Micelles in Nanomedicine Applications. *Chem Rev* **2018,** *118* (14), 6844-6892.

30. Nuhn, L.; Hirsch, M.; Krieg, B.; Koynov, K.; Fischer, K.; Schmidt, M.; Helm, M.; Zentel, R., Cationic Nanohydrogel Particles as Potential siRNA Carriers for Cellular Delivery. *ACS Nano* **2012,** *6*, 2198-2214.

31. Tabujew, I.; Freidel, C.; Krieg, B.; Helm, M.; Koynov, K.; Mullen, K.; Peneva, K., The guanidinium group as a key part of water-soluble polymer carriers for siRNA complexation and protection against degradation. *Macromol Rapid Commun* **2014,** *35* (13), 1191-7.

32. Fritz, T.; Voigt, M.; Worm, M.; Negwer, I.; Muller, S. S.; Kettenbach, K.; Ross, T. L.; Roesch, F.; Koynov, K.; Frey, H.; Helm, M., Orthogonal Click Conjugation to the Liposomal Surface Reveals the Stability of the Lipid Anchorage as Crucial for Targeting. *Chemistry* **2016,** *22* (33), 11578-82.

33. Hood, M. A.; Paiphansiri, U.; Schaeffel, D.; Koynov, K.; Kappl, M.; Landfester, K.; Muñoz-Espí, R., Hybrid Poly(urethane–urea)/Silica Nanocapsules with pH-Sensitive Gateways. *Chemistry of Materials* **2015,** *27* (12), 4311-4318.

34. Leber, N.; Kaps, L.; Aslam, M.; Schupp, J.; Brose, A.; Schaffel, D.; Fischer, K.; Diken, M.; Strand, D.; Koynov, K.; Tuettenberg, A.; Nuhn, L.; Zentel, R.; Schuppan, D., SiRNA-

mediated in vivo gene knockdown by acid-degradable cationic nanohydrogel particles. *J Control Release* **2017,** *248*, 10-23.

35. Bouchaala, R.; Richert, L.; Anton, N.; Vandamme, T. F.; Djabi, S.; Mely, Y.; Klymchenko, A. S., Quantifying Release from Lipid Nanocarriers by Fluorescence Correlation Spectroscopy. *ACS Omega* **2018,** *3* (10), 14333-14340.
36. Draffehn, S.; Eichhorst, J.; Wiesner, B.; Kumke, M. U., Insight into the Modification of Polymeric Micellar and Liposomal Nanocarriers by Fluorescein-Labeled Lipids and Uptake-Mediating Lipopeptides. *Langmuir* **2016,** *32* (27), 6928-39.
37. Jenjob, R.; Seidi, F.; Crespy, D., Recent advances in polymerizations in dispersed media. *Adv Colloid Interface Sci* **2018,** *260*, 24-31.
38. Schaeffel, D.; Staff, R. H.; Butt, H. J.; Landfester, K.; Crespy, D.; Koynov, K., Fluorescence correlation spectroscopy directly monitors coalescence during nanoparticle preparation. *Nano Lett* **2012,** *12* (11), 6012-7.
39. Staff, R. H.; Schaeffel, D.; Turshatov, A.; Donadio, D.; Butt, H. J.; Landfester, K.; Koynov, K.; Crespy, D., Particle formation in the emulsion-solvent evaporation process. *Small* **2013,** *9* (20), 3514-22.
40. Crespy, D.; Landfester, K., Miniemulsion polymerization as a versatile tool for the synthesis of functionalized polymers. *Beilstein J Org Chem* **2010,** *6*, 1132-48.
41. Antonietti, M.; Landfester, K., Polyreactions in miniemulsions. *Progress in Polymer Science* **2002,** *27*, 689-757.
42. Landfester, K.; Bechthold, N.; Franca Tiarks; Antonietti, M., Formulation and Stability Mechanisms of Polymerizable Miniemulsions. *Macromolecules* **1999,** *32*, 5222-5228.
43. Tiarks, F.; Landfester, K.; Antonietti, M., Encapsulation of Carbon Black by Miniemulsion Polymerization. *Macromol. Chem. Phys.* **2001,** *202*, 51-60.
44. Schoth, A.; Keith, A. D.; Landfester, K.; Muñoz-Espí, R., Silanization as a versatile functionalization method for the synthesis of polymer/magnetite hybrid nanoparticles with controlled structure. *RSC Advances* **2016,** *6* (59), 53903-53911.
45. Manaia, E. B.; Abucafy, M. P.; Chiari-Andreo, B. G.; Silva, B. L.; Oshiro Junior, J. A.; Chiavacci, L. A., Physicochemical characterization of drug nanocarriers. *Int J Nanomedicine* **2017,** *12*, 4991-5011.
46. Mahira, S.; Rayapolu, R. G.; Khan, W., Nanoscale characterization of nanocarriers. In *Smart Nanocontainers*, 2020; pp 49-65.
47. Landfester, K., Recent developments in miniemulsions formation and stability mechanisms. *Macromol. Symp.* **2000,** *150*, 171-178.

48. Gharieh, A.; Khoee, S.; Mahdavian, A. R., Emulsion and miniemulsion techniques in preparation of polymer nanoparticles with versatile characteristics. *Advances in Colloid and Interface Science* **2019,** *269*, 152-186.

49. Friebel, M.; Roggan, A.; Muller, G.; Meinke, M., Determination of optical properties of human blood in the spectral range 250 to 1100 nm using Monte Carlo simulations with hematocrit-dependent effective scattering phase functions. *J Biomed Opt* **2006,** *11* (3), 34021.

50. Prozeller, D.; Morsbach, S.; Landfester, K., Isothermal titration calorimetry as a complementary method for investigating nanoparticle-protein interactions. *Nanoscale* **2019,** *11* (41), 19265-19273.

51. Martínez-Negro, M.; González-Rubio, G.; Aicart, E.; Landfester, K.; Guerrero-Martínez, A.; Junquera, E., Insights into colloidal nanoparticle-protein corona interactions for nanomedicine applications. *Adv. Colloid Interface Sci.* **2021,** *289*.

52. Negwer, I.; Best, A.; Schinnerer, M.; Schafer, O.; Capeloa, L.; Wagner, M.; Schmidt, M.; Mailander, V.; Helm, M.; Barz, M.; Butt, H. J.; Koynov, K., Monitoring drug nanocarriers in human blood by near-infrared fluorescence correlation spectroscopy. *Nat Commun* **2018,** *9* (1), 5306.

53. Schmitt, S.; Nuhn, L.; Barz, M.; Butt, H. J.; Koynov, K., Shining Light on Polymeric Drug Nanocarriers with Fluorescence Correlation Spectroscopy. *Macromol Rapid Commun* **2022**, e2100892.

54. Lakowicz, J. R., Principles of Fluorescence Spectroscopy. University of Maryland School of Medicine Baltimore, Maryland, USA: 2010.

55. Rigler, R.; Elson, E. S., Fluorescence Correlation Spectroscopy: Theory and Applications. Springer: 2001.

56. Thermo Fisher Scientific, https://www.thermofisher.com/de/de/home/brands/molecular-probes/key-molecular-probes-products/alexa-fluor/alexa-fluor-dyes-across-the-spectrum.html (accessed 28.02.2022).

57. Haidekker, M. A.; Theodorakis, E. A., Environment-sensitive behavior of fluorescent molecular rotors. *Journal of Biological Engineering* **2010,** *4:11*.

58. Haidekker, M. A.; Brady, T. P.; Lichlyter, D.; Theodorakis, E. A., Effects of solvent polarity and solvent viscosity on the fluorescent properties of molecular rotors and related probes. *Bioorg Chem* **2005,** *33* (6), 415-25.

59. Vaccaro, G.; Bianchi, A.; Mauri, M.; Bonetti, S.; Meinardi, F.; Sanguineti, A.; Simonutti, R.; Beverina, L., Direct monitoring of self-assembly of copolymeric micelles by a luminescent molecular rotor. *Chem Commun (Camb)* **2013,** *49* (76), 8474-6.

60. Nölle, J. M.; Jüngst, C.; Zumbusch, A.; Wöll, D., Monitoring of viscosity changes during free radical polymerization using fluorescence lifetime measurements. *Polymer Chemistry* **2014,** *5* (8), 2700-2703.

61. Klymchenko, A. S., Solvatochromic and Fluorogenic Dyes as Environment-Sensitive Probes: Design and Biological Applications. *Acc Chem Res* **2017,** *50* (2), 366-375.

62. Borelli, M.; Iasilli, G.; Minei, P.; Pucci, A., Fluorescent Polystyrene Films for the Detection of Volatile Organic Compounds Using the Twisted Intramolecular Charge Transfer Mechanism. *Molecules* **2017,** *22* (8).

63. Martini, G.; Martinelli, E.; Ruggeri, G.; Galli, G.; Pucci, A., Julolidine fluorescent molecular rotors as vapour sensing probes in polystyrene films. *Dyes and Pigments* **2015,** *113*, 47-54.

64. Boreham, A.; Brodwolf, R.; Walker, K.; Haag, R.; Alexiev, U., Time-Resolved Fluorescence Spectroscopy and Fluorescence Lifetime Imaging Microscopy for Characterization of Dendritic Polymer Nanoparticles and Applications in Nanomedicine. *Molecules* **2016,** *22* (1).

65. Cai, L.; Li, H.; Yu, X.; Wu, L.; Wei, X.; James, T. D.; Huang, C., Green Fluorescent Protein GFP-Chromophore-Based Probe for the Detection of Mitochondrial Viscosity in Living Cells. *ACS Appl Bio Mater* **2021,** *4* (3), 2128-2134.

66. Wang, H.; Zhao, W.; Liu, X.; Wang, S.; Wang, Y., BODIPY-Based Fluorescent Surfactant for Cell Membrane Imaging and Photodynamic Therapy. *ACS Appl Bio Mater* **2020,** *3* (1), 593-601.

67. Ashoka, A. H.; Ashokkumar, P.; Kovtun, Y. P.; Klymchenko, A. S., Solvatochromic Near-Infrared Probe for Polarity Mapping of Biomembranes and Lipid Droplets in Cells under Stress. *J Phys Chem Lett* **2019,** *10* (10), 2414-2421.

68. Becker, W., Fluorescence lifetime imaging--techniques and applications. *J Microsc* **2012,** *247* (2), 119-36.

69. Wahl, M. Time-Correlated Single Photon Counting 2014.

70. Magde, D.; Elson, E.; Webb, W. W., Thermodynamic Fluctuations in a Reacting System—Measurement by Fluorescence Correlation Spectroscopy. *Physical Review Letters* **1972,** *29* (11), 705-708.

71. Kristensen, K.; Urquhart, A. J.; Thormann, E.; Andresen, T. L., Binding of human serum albumin to PEGylated liposomes: insights into binding numbers and dynamics by fluorescence correlation spectroscopy. *Nanoscale* **2016,** *8* (47), 19726-19736.

72. Watanabe, S.; Hayashi, K.; Toh, K.; Kim, H. J.; Liu, X.; Chaya, H.; Fukushima, S.; Katsushima, K.; Kondo, Y.; Uchida, S.; Ogura, S.; Nomoto, T.; Takemoto, H.; Cabral, H.; Kinoh, H.; Tanaka, H. Y.; Kano, M. R.; Matsumoto, Y.; Fukuhara, H.; Uchida, S.; Nangaku, M.; Osada, K.; Nishiyama, N.; Miyata, K.; Kataoka, K., In vivo rendezvous of small nucleic

acid drugs with charge-matched block catiomers to target cancers. *Nat Commun* **2019,** *10* (1), 1894.

73. Fu, X.; Sompol, P.; Brandon, J. A.; Norris, C. M.; Wilkop, T.; Johnson, L. A.; Richards, C. I., In Vivo Single-Molecule Detection of Nanoparticles for Multiphoton Fluorescence Correlation Spectroscopy to Quantify Cerebral Blood Flow. *Nano Lett* **2020,** *20* (8), 6135-6141.

74. Wang, H.; Shang, L.; Maffre, P.; Hohmann, S.; Kirschhofer, F.; Brenner-Weiss, G.; Nienhaus, G. U., The Nature of a Hard Protein Corona Forming on Quantum Dots Exposed to Human Blood Serum. *Small* **2016,** *12* (42), 5836-5844.

75. Pereira, S.; Santos, R. S.; Moreira, L.; Guimaraes, N.; Gomes, M.; Zhang, H.; Remaut, K.; Braeckmans, K.; De Smedt, S.; Azevedo, N. F., Lipoplexes to Deliver Oligonucleotides in Gram-Positive and Gram-Negative Bacteria: Towards Treatment of Blood Infections. *Pharmaceutics* **2021,** *13* (7).

76. Krieger, J. W.; Singh, A. P.; Bag, N.; Garbe, C. S.; Saunders, T. E.; Langowski, J.; Wohland, T., Imaging fluorescence (cross-) correlation spectroscopy in live cells and organisms. *Nat Protoc* **2015,** *10* (12), 1948-74.

77. Kim, S. A.; Schwille, P., Intracellular applications of fluorescence correlation spectroscopy: prospects for neuroscience. *Curr Opin Neurobiol* **2003,** *13* (5), 583-90.

78. Koynov, K.; Butt, H.-J., Fluorescence correlation spectroscopy in colloid and interface science. *Current Opinion in Colloid & Interface Science* **2012,** *17* (6), 377-387.

79. Kramer, S.; Svatunek, D.; Alberg, I.; Grafen, B.; Schmitt, S.; Braun, L.; van Onzen, A.; Rossin, R.; Koynov, K.; Mikula, H.; Zentel, R., HPMA-Based Nanoparticles for Fast, Bioorthogonal iEDDA Ligation. *Biomacromolecules* **2019,** *20* (10), 3786-3797.

80. Gurny, R.; Peppas, N. A.; Harrington, D. D.; Banker, G. S., Development of Biodegradable and Injectable Latices for Controlled Release of Potent Drugs. *Drug Development and Industrial Pharmacy* **1981,** *7* (1), 1-25.

81. Jodar-Reyes, A. B.; Martin-Rodriguez, A.; Ortega-Vinuesa, J. L., Effect of the ionic surfactant concentration on the stabilization/destabilization of polystyrene colloidal particles. *J Colloid Interface Sci* **2006,** *298* (1), 248-57.

82. Desgouilles, S.; Vauthier, C.; Bazile, D.; Vacus, J.; Grossiord, J.-L.; Veillard, M.; Couvreur, P., The Design of Nanoparticles Obtained by Solvent Evaporation: A Comprehensive Study. *Langmuir* **2003,** *19*, 9504-9510.

83. Wang, J.; Schwendeman, S., Mechanisms of Solvent Evaporation Encapsulation Processes: Prediction of Solvent Evaporation Rate. *Journal of Pharmaceutical Sciences* **1999,** *88*, 1090-1099.

84. Sawalha, H.; Purwanti, N.; Rinzema, A.; Schroën, K.; Boom, R., Polylactide microspheres prepared by premix membrane emulsification—Effects of solvent removal rate. *Journal of Membrane Science* **2008,** *310* (1-2), 484-493.

85. Abe, A.; Albrecht, K.; Appel, A.-K.; Bode, S.; Crespy, D.; Deming, T. J.; DeVane, R.; Dingels, C.; Fiorin, G.; Freire, F.; Frey, H.; Gangloff, N.; Groll, J.; Haddleton, D. M.; Hager, M. D.; Hur, K.; Jia, Z.; Kerscher, B.; Klein, M. L.; Kobayashi, S.; Landfester, K.; Luxenhofer, R.; Möller, M.; Monteiro, M. J.; Mülhaupt, R.; Müllen, K.; Ohta, Y.; Quinoa, E.; Riguera, R.; Rudick, J. G.; Rybtchinski, B.; Sandmann, B.; Schadt, K.; Schubert, U. S.; Schüler, F.; Seco, J. M.; Shinoda, W.; Singh, S.; Staff, R. H.; Topuz, F.; Wiesner, U.; Yokozawa, T.; Zhang, Q., Hierarchical Macromolecular Structures: 60 Years after the Staudinger Nobel Prize II. Percec, V., Ed. Springer Cham Heidelberg New York Dordrecht London, 2013.

86. Deng, R.; Li, H.; Zhu, J.; Li, B.; Liang, F.; Jia, F.; Qu, X.; Yang, Z., Janus Nanoparticles of Block Copolymers by Emulsion Solvent Evaporation Induced Assembly. *Macromolecules* **2016,** *49* (4), 1362-1368.

87. Kikuchi, S.; Shoji, R.; Yoshida, S.; Kanehashi, S.; Ma, G.-H.; Ogino, K., Fabrication of inverse core–shell and Janus-structured microspheres of blends of poly(4-butyltriphenylamine) and poly(methyl methacrylate). *Colloid and Polymer Science* **2020,** *298* (3), 251-261.

88. Zhao, Y.; Fickert, J.; Landfester, K.; Crespy, D., Encapsulation of self-healing agents in polymer nanocapsules. *Small* **2012,** *8* (19), 2954-8.

89. Antonietti, M.; Landfester, K., Polyreactions in miniemulsions. *Prog. Polym. Sci.* **2002**, 689-757.

90. Chern, C. S., Emulsion polymerization mechanisms and kinetics. *Progress in Polymer Science* **2006,** *31* (5), 443-486.

91. Bibette, J.; Caruso, F.; Currie, F.; Elaissari, A.; Esumi, K.; Ganachaud, E.; Gruber, C.; Häger, M.; Holmberg, K.; Kräuter, I.; Landfester, K.; Leal-Calderon, E.; Paleos, C. M.; Pichot, C.; Schmitt, V.; Tovar, G. E. M.; Tsiourvas, D., Colloid Chemistry II Meijere, A. d.; Houk, K. N.; Kessler, H.; Lehn, J.-M.; Ley, S. V.; Schreiber, S. L.; Thiem, J.; Trost, B. M.; Vögtle, F.; Yamamoto, H.; Antonietti, M., Eds. Springer: Berlin, Heidelberg, New York, Hong Kong, London, Milan, Paris, Tokyo 2003.

92. Landfester, K.; Bechthold, N.; Tiarks, F.; Antonietti, M., Formulation and Stability Mechanisms of Polymerizable Miniemulsions. *Macromolecules* **1999,** *32*, 5222-5228.

93. Koenig, A.; Ziener, U.; Schaz, A.; Landfester, K., Polyurethane-block-polystyrene Prepared by Polymerization in Miniemulsion. *Macromolecular Chemistry and Physics* **2007,** *208* (2), 155-163.

94. Guo, J.; Choi, K. Y.; Schork, F. J., Miniemulsion Copolymerization of Ethylene and Vinyl Acetate. *Macromolecular Reaction Engineering* **2009,** *3* (7), 412-418.

95. Romio, A. P.; Rodrigues, H. H.; Peres, A.; Da Cas Viegas, A.; Kobitskaya, E.; Ziener, U.; Landfester, K.; Sayer, C.; Araújo, P. H. H., Encapsulation of magnetic nickel nanoparticles via inverse miniemulsion polymerization. *Journal of Applied Polymer Science* **2013,** *129* (3), 1426-1433.

96. Frey, M.-L.; Simon, J.; Brückner, M.; Mailänder, V.; Morsbach, S.; Landfester, K., Bio-orthogonal triazolinedione (TAD) crosslinked protein nanocapsules affect protein adsorption and cell interaction. *Polymer Chemistry* **2020,** *11* (23), 3821-3830.

97. Peres, L. B.; dos Anjos, R. S.; Tappertzhofen, L. C.; Feuser, P. E.; de Araújo, P. H. H.; Landfester, K.; Sayer, C.; Muñoz-Espí, R., pH-responsive physically and chemically cross-linked glutamic-acid-based hydrogels and nanogels. *European Polymer Journal* **2018,** *101*, 341-349.

98. Stefl, M.; Benda, A.; Gregor, I.; Hof, M., The fast polarization modulation based dual-focus fluorescence correlation spectroscopy. *Opt Express* **2014,** *22* (1), 885-99.

99. Miao, W.; Yu, C.; Hao, E.; Jiao, L., Functionalized BODIPYs as Fluorescent Molecular Rotors for Viscosity Detection. *Front Chem* **2019,** *7*, 825.

100. Lee, S. C.; Heo, J.; Woo, H. C.; Lee, J. A.; Seo, Y. H.; Lee, C. L.; Kim, S.; Kwon, O. P., Fluorescent Molecular Rotors for Viscosity Sensors. *Chemistry* **2018,** *24* (52), 13706-13718.

101. Amdursky, N.; Erez, Y.; Huppert, D., Molecular Rotors: What Lies Behind the High Sensitivity of the Thioflavin-T Fluorescent Marker. *Acc Chem Res* **2012,** *45*, 1548-1557.

102. Oswal, S.; Rathnam, M. V., Viscosity data of binary mixtures: ethyl acetate + cyclohexane, + benzene, + toluene, + ethylbenzene + carbon tetrachloride, and + chloroform at 303.15 K *Canadian Journal of Chemistry* **1982,** *62*, 2851-2853.

103. Wohlfarth, C. *Viscosity of styrene: Datasheet from Physical Chemistry · Volume 29: "Viscosity of Pure Organic Liquids and Binary Liquid Mixtures" in SpringerMaterials*, Springer-Verlag Berlin Heidelberg.

104. Wohlfarth, C. *Viscosity of hexadecane: Datasheet from Landolt-Börnstein - Group IV Physical Chemistry · Volume 25: "Supplement to IV/18" in SpringerMaterials,* Springer-Verlag Berlin Heidelberg.

105. Li, W.-I.; Anderson, K. W.; DeLuca, P. P., Kinetic and thermodynamic modeling of the formation of polymeric microspheres using solvent extraction/evaporation method. *Journal of Controlled Release* **1995,** *37*, 187-198.

106. Li, W.-I.; Anderson, K. W.; Mehta, R. C.; DeLuca, P. P., Prediction of solvent removal profile and effect on properties for peptide-loaded PLGA microspheres prepared by solvent extraction/evaporation method. *Journal of Controlled Release* **1995,** *37*, 199-214.

107. Colby, R. H., Structure and linear viscoelasticity of flexible polymer solutions: comparison of polyelectrolyte and neutral polymer solutions. *Rheologica Acta* **2009,** *49* (5), 425-442.

108. Reneker, D. H.; Yarin, A. L., Electrospinning jets and polymer nanofibers. *Polymer* **2008,** *49* (10), 2387-2425.

109. Zhu, D.; Haidekker, M. A.; Lee, J.-S.; Won, Y.-Y.; Lee, J. C.-M., Application of Molecular Rotors to the Determination of the Molecular Weight Dependence of Viscosity in Polymer Melts. *Macromolecules* **2007,** *40*, 7730-7732.

110. Jee, A.-Y.; Bae, E.; Lee, M., Internal Twisting Dynamics of Dicyanovinyljulolidine in Polymers. *J. Phys. Chem. B* **2009,** *113*, 16508-16512.

111. Brandes R., Lang F., Schmidt R. F., Physiologie des Menschen. 2019.

112. Müller-Esterl, W., Biochemie: Eine Einführung für Mediziner und Naturwissenschaftler. Springer Spektrum: 2018.

113. Wilhelm, S.; J. Tavares, A.; Qin Dai, S. O.; Audet, J.; F. Dvorak, H.; C. W. Chan, W., Analysis of nanoparticle delivery to tumours. *Nat Rev Mater* **2016,** *1* (16014).

114. Cheng, Y. H.; He, C.; Riviere, J. E.; Monteiro-Riviere, N. A.; Lin, Z., Meta-Analysis of Nanoparticle Delivery to Tumors Using a Physiologically Based Pharmacokinetic Modeling and Simulation Approach. *ACS Nano* **2020,** *14* (3), 3075-3095.

115. Srivastava, I.; Khan, M. S.; Dighe, K.; Alafeef, M.; Wang, Z.; Banerjee, T.; Ghonge, T.; Grove, L. M.; Bashir, R.; Pan, D., On-Chip Electrical Monitoring of Real-Time “Soft” and “Hard” Protein Corona Formation on Carbon Nanoparticles. *small methods* **2020,** *4* (7).

116. Yu, Q.; Zhao, L.; Guo, C.; Yan, B.; Su, G., Regulating Protein Corona Formation and Dynamic Protein Exchange by Controlling Nanoparticle Hydrophobicity. *Front Bioeng Biotechnol* **2020,** *8*, 210.

117. Xiao, W.; Gao, H., The impact of protein corona on the behavior and targeting capability of nanoparticle-based delivery system. *Int J Pharm* **2018,** *552* (1-2), 328-339.

118. Yong, S. B.; Song, Y.; Kim, H. J.; Ain, Q. U.; Kim, Y. H., Mononuclear phagocytes as a target, not a barrier, for drug delivery. *J Control Release* **2017,** *259*, 53-61.

119. Chinen, A. B.; Guan, C. M.; Ko, C. H.; Mirkin, C. A., The Impact of Protein Corona Formation on the Macrophage Cellular Uptake and Biodistribution of Spherical Nucleic Acids. *small* **2017,** *13* (16).

120. Zhang, Y. N.; Poon, W.; Tavares, A. J.; McGilvray, I. D.; Chan, W. C. W., Nanoparticle-liver interactions: Cellular uptake and hepatobiliary elimination. *J Control Release* **2016,** *240*, 332-348.

121. Lin, X.; Pan, Q.; He, Y., In situ detection of protein corona on single particle by rotational diffusivity. *Nanoscale* **2019,** *11* (39), 18367-18374.

122. Meghani, N. M.; Amin, H.; Park, C.; Cui, J. H.; Cao, Q. R.; Choi, K. H.; Lee, B. J., Combinatory interpretation of protein corona and shear stress for active cancer targeting of

bioorthogonally clickable gelatin-oleic nanoparticles. *Mater Sci Eng C Mater Biol Appl* **2020,** *111*, 110760.

123. Su, G.; Jiang, H.; Xu, B.; Yu, Y.; Chen, X., Effects of Protein Corona on Active and Passive Targeting of Cyclic RGD Peptide-Functionalized PEGylation Nanoparticles. *Mol Pharm* **2018,** *15* (11), 5019-5030.

124. Su, G.; Zhou, H.; Mu, Q.; Zhang, Y.; Li, L.; Jiao, P.; Jiang, G.; Yan, B., Effective Surface Charge Density Determines the Electrostatic Attraction between Nanoparticles and Cells. *The Journal of Physical Chemistry C* **2012,** *116* (8), 4993-4998.

125. Digiacomo, L.; Jafari-Khouzani, K.; Palchetti, S.; Pozzi, D.; Capriotti, A. L.; Lagana, A.; Zenezini Chiozzi, R.; Caputo, D.; Cascone, C.; Coppola, R.; Flammia, G.; Altomare, V.; Grasso, A.; Mahmoudi, M.; Caracciolo, G., A protein corona sensor array detects breast and prostate cancers. *Nanoscale* **2020,** *12* (32), 16697-16704.

126. Ho, Y. T.; Azman, N.; Loh, F. W. Y.; Ong, G. K. T.; Engudar, G.; Kriz, S. A.; Kah, J. C. Y., Protein Corona Formed from Different Blood Plasma Proteins Affects the Colloidal Stability of Nanoparticles Differently. *Bioconjug Chem* **2018,** *29* (11), 3923-3934.

127. Pitek, A. S.; Wen, A. M.; Shukla, S.; Steinmetz, N. F., The Protein Corona of Plant Virus Nanoparticles Influences their Dispersion Properties, Cellular Interactions, and In Vivo Fates. *Small* **2016,** *12* (13), 1758-69.

128. Mirshafiee, V.; Mahmoudi, M.; Lou, K.; Cheng, J.; Kraft, M. L., Protein corona significantly reduces active targeting yield. *Chem Commun (Camb)* **2013,** *49* (25), 2557-9.

129. Dai, Q.; Yan, Y.; Guo, J.; Björnmalm, M.; Cui, J.; Sun, H.; Caruso, F., Targeting Ability of Affibody-Functionalized Particles Is Enhanced by Albumin but Inhibited by Serum Coronas. *ACS Macro Letters* **2015,** *4* (11), 1259-1263.

130. Varnamkhasti, B. S.; Hosseinzadeh, H.; Azhdarzadeh, M.; Vafaei, S. Y.; Esfandyari-Manesh, M.; Mirzaie, Z. H.; Amini, M.; Ostad, S. N.; Atyabi, F.; Dinarvand, R., Protein corona hampers targeting potential of MUC1 aptamer functionalized SN-38 core-shell nanoparticles. *Int J Pharm* **2015,** *494* (1), 430-44.

131. Zhang, H.; Wu, T.; Yu, W.; Ruan, S.; He, Q.; Gao, H., Ligand Size and Conformation Affect the Behavior of Nanoparticles Coated with in Vitro and in Vivo Protein Corona. *ACS Appl Mater Interfaces* **2018,** *10* (10), 9094-9103.

132. Simon, J.; Muller, L. K.; Kokkinopoulou, M.; Lieberwirth, I.; Morsbach, S.; Landfester, K.; Mailander, V., Exploiting the biomolecular corona: pre-coating of nanoparticles enables controlled cellular interactions. *Nanoscale* **2018,** *10* (22), 10731-10739.

133. Giulimondi, F.; Digiacomo, L.; Pozzi, D.; Palchetti, S.; Vulpis, E.; Capriotti, A. L.; Chiozzi, R. Z.; Lagana, A.; Amenitsch, H.; Masuelli, L.; Peruzzi, G.; Mahmoudi, M.;

Screpanti, I.; Zingoni, A.; Caracciolo, G., Interplay of protein corona and immune cells controls blood residency of liposomes. *Nat Commun* **2019,** *10* (1), 3686.

134. Mirshafiee, V.; Kim, R.; Park, S.; Mahmoudi, M.; Kraft, M. L., Impact of protein pre-coating on the protein corona composition and nanoparticle cellular uptake. *Biomaterials* **2016,** *75*, 295-304.

135. Müller, L. K.; Simon, J.; Schöttler, S.; Landfester, K.; Mailänder, V.; Mohr, K., Pre-coating with protein fractions inhibits nano-carrier aggregation in human blood plasma. *RSC Advances* **2016,** *6* (99), 96495-96509.

136. Bertrand, N.; Grenier, P.; Mahmoudi, M.; Lima, E. M.; Appel, E. A.; Dormont, F.; Lim, J. M.; Karnik, R.; Langer, R.; Farokhzad, O. C., Mechanistic understanding of in vivo protein corona formation on polymeric nanoparticles and impact on pharmacokinetics. *Nat Commun* **2017,** *8* (1), 777.

137. Schottler, S.; Becker, G.; Winzen, S.; Steinbach, T.; Mohr, K.; Landfester, K.; Mailander, V.; Wurm, F. R., Protein adsorption is required for stealth effect of poly(ethylene glycol)- and poly(phosphoester)-coated nanocarriers. *Nat Nanotechnol* **2016,** *11* (4), 372-7.

138. Wang, J. L.; Du, X. J.; Yang, J. X.; Shen, S.; Li, H. J.; Luo, Y. L.; Iqbal, S.; Xu, C. F.; Ye, X. D.; Cao, J.; Wang, J., The effect of surface poly(ethylene glycol) length on in vivo drug delivery behaviors of polymeric nanoparticles. *Biomaterials* **2018,** *182*, 104-113.

139. Du, X. J.; Wang, J. L.; Liu, W. W.; Yang, J. X.; Sun, C. Y.; Sun, R.; Li, H. J.; Shen, S.; Luo, Y. L.; Ye, X. D.; Zhu, Y. H.; Yang, X. Z.; Wang, J., Regulating the surface poly(ethylene glycol) density of polymeric nanoparticles and evaluating its role in drug delivery in vivo. *Biomaterials* **2015,** *69*, 1-11.

140. Settanni, G.; Schafer, T.; Muhl, C.; Barz, M.; Schmid, F., Poly-sarcosine and Poly(Ethylene-Glycol) Interactions with Proteins Investigated Using Molecular Dynamics Simulations. *Comput Struct Biotechnol J* **2018,** *16*, 543-550.

141. Otter, R.; Klinker, K.; Spitzer, D.; Schinnerer, M.; Barz, M.; Besenius, P., Folding induced supramolecular assembly into pH-responsive nanorods with a protein repellent shell. *Chem Commun (Camb)* **2018,** *54* (4), 401-404.

142. Weber, B.; Birke, A.; Fischer, K.; Schmidt, M.; Barz, M., Solution Properties of Polysarcosine: From Absolute and Relative Molar Mass Determinations to Complement Activation. *Macromolecules* **2018,** *51* (7), 2653-2661.

143. Bleher, S.; Buck, J.; Muhl, C.; Sieber, S.; Barnert, S.; Witzigmann, D.; Huwyler, J.; Barz, M.; Süss, R., Poly(Sarcosine) Surface Modification Imparts Stealth-Like Properties to Liposomes. *small* **2019,** *15* (50).

144. Weiss, A. C. G.; Kelly, H. G.; Faria, M.; Besford, Q. A.; Wheatley, A. K.; Ang, C. S.; Crampin, E. J.; Caruso, F.; Kent, S. J., Link between Low-Fouling and Stealth: A Whole Blood

Biomolecular Corona and Cellular Association Analysis on Nanoengineered Particles. *ACS Nano* **2019,** *13* (5), 4980-4991.

145. Debayle, M.; Balloul, E.; Dembele, F.; Xu, X.; Hanafi, M.; Ribot, F.; Monzel, C.; Coppey, M.; Fragola, A.; Dahan, M.; Pons, T.; Nicolas Lequeux, Zwitterionic polymer ligands: an ideal surface coating to totally suppress protein-nanoparticle corona formation? *Biomaterials* **2019,** *219* (119357).

146. Banskota, S.; Saha, S.; Bhattacharya, J.; Kirmani, N.; Yousefpour, P.; Dzuricky, M.; Zakharov, N.; Li, X.; Spasojevic, I.; Young, K.; Chilkoti, A., Genetically Encoded Stealth Nanoparticles of a Zwitterionic Polypeptide-Paclitaxel Conjugate Have a Wider Therapeutic Window than Abraxane in Multiple Tumor Models. *Nano Lett* **2020,** *20* (4), 2396-2409.

147. Schöttler, D. S.; Landfester, P. D. K.; Mailänder, P. D. V., Controlling the Stealth Effect of Nanocarriers through Understanding the Protein Corona. *Angew Chem Int Ed Engl* **2016,** *55* (31).

148. Rausch, K.; Reuter, A.; Fischer, K.; Schmidt, M., Evaluation of Nanoparticle Aggregation in Human Blood Serum. *Biomacromolecules* **2010,** *11*, 2836-2839.

149. Gonzalez-Carter, D.; Liu, X.; Tockary, T. A.; Dirisala, A.; Toh, K.; Anraku, Y.; Kataoka, K., Targeting nanoparticles to the brain by exploiting the blood-brain barrier impermeability to selectively label the brain endothelium. *Proc Natl Acad Sci U S A* **2020,** *117* (32), 19141-19150.

150. Miyazaki, T.; Uchida, S.; Nagatoishi, S.; Koji, K.; Hong, T.; Fukushima, S.; Tsumoto, K.; Ishihara, K.; Kataoka, K.; Cabral, H., Polymeric Nanocarriers with Controlled Chain Flexibility Boost mRNA Delivery In Vivo through Enhanced Structural Fastening. *Adv Healthc Mater* **2020,** *9* (16), e2000538.

151. Tao, A.; Huang, G. L.; Igarashi, K.; Hong, T.; Liao, S.; Stellacci, F.; Matsumoto, Y.; Yamasoba, T.; Kataoka, K.; Cabral, H., Polymeric Micelles Loading Proteins through Concurrent Ion Complexation and pH-Cleavable Covalent Bonding for In Vivo Delivery. *Macromol Biosci* **2020,** *20* (1), e1900161.

152. Sueyoshi, D.; Anraku, Y.; Komatsu, T.; Urano, Y.; Kataoka, K., Enzyme-Loaded Polyion Complex Vesicles as in Vivo Nanoreactors Working Sustainably under the Blood Circulation: Characterization and Functional Evaluation. *Biomacromolecules* **2017,** *18* (4), 1189-1196.

153. Min, H. S.; Kim, H. J.; Naito, M.; Ogura, S.; Toh, K.; Hayashi, K.; Kim, B. S.; Fukushima, S.; Anraku, Y.; Miyata, K.; Kataoka, K., Systemic Brain Delivery of Antisense Oligonucleotides across the Blood-Brain Barrier with a Glucose-Coated Polymeric Nanocarrier. *Angew Chem Int Ed Engl* **2020,** *59* (21), 8173-8180.

154. Dakwar, G. R.; Braeckmans, K.; Ceelen, W.; De Smedt, S. C.; Remaut, K., Exploring the HYDRAtion method for loading siRNA on liposomes: the interplay between stability and biological activity in human undiluted ascites fluid. *Drug Deliv Transl Res* **2017,** *7* (2), 241-251.

155. Mittag, J. J.; Kneidl, B.; Preibeta, T.; Hossann, M.; Winter, G.; Wuttke, S.; Engelke, H.; Radler, J. O., Impact of plasma protein binding on cargo release by thermosensitive liposomes probed by fluorescence correlation spectroscopy. *Eur J Pharm Biopharm* **2017,** *119*, 215-223.

156. Yang, W.; Miyazaki, T.; Chen, P.; Hong, T.; Naito, M.; Miyahara, Y.; Matsumoto, A.; Kataoka, K.; Miyata, K.; Cabral, H., Block catiomer with flexible cationic segment enhances complexation with siRNA and the delivery performance in vitro. *Sci Technol Adv Mater* **2021,** *22* (1), 850-863.

157. Vilanova, O.; Mittag, J. J.; Kelly, P. M.; Milani, S.; Dawson, K. A.; Radler, J. O.; Franzese, G., Understanding the Kinetics of Protein-Nanoparticle Corona Formation. *ACS Nano* **2016,** *10* (12), 10842-10850.

158. Tiiman, A.; Jelic, V.; Jarvet, J.; Jaremo, P.; Bogdanovic, N.; Rigler, R.; Terenius, L.; Graslund, A.; Vukojevic, V., Amyloidogenic Nanoplaques in Blood Serum of Patients with Alzheimer's Disease Revealed by Time-Resolved Thioflavin T Fluorescence Intensity Fluctuation Analysis. *J Alzheimers Dis* **2019,** *68* (2), 571-582.

159. Haque, A.; Faizi, M. S. H.; Rather, J. A.; Khan, M. S., Next generation NIR fluorophores for tumor imaging and fluorescence-guided surgery: A review. *Bioorg Med Chem* **2017,** *25* (7), 2017-2034.

160. Kaps, L.; Nuhn, L.; Aslam, M.; Brose, A.; Foerster, F.; Rosigkeit, S.; Renz, P.; Heck, R.; Kim, Y. O.; Lieberwirth, I.; Schuppan, D.; Zentel, R., In Vivo Gene-Silencing in Fibrotic Liver by siRNA-Loaded Cationic Nanohydrogel Particles. *Adv Healthc Mater* **2015,** *4* (18), 2809-15.

161. Liu, H. S.; Ishizuka, T.; Kawaguchi, M.; Nishii, R.; Kataoka, H.; Xu, Y., A Nucleoside Derivative 5-Vinyluridine (VrU) for Imaging RNA in Cells and Animals. *Bioconjug Chem* **2019,** *30* (11), 2958-2966.

162. Li, H.; Van Herck, S.; Liu, Y.; Hao, Y.; Ding, X.; Nuhn, L.; Zhong, Z.; Combes, F.; Sanders, N. N.; Lienenklaus, S.; Koker, S. D.; David, S. A.; Wang, Y.; De Geest, B. G.; Zhang, Z., Imidazoquinoline-Conjugated Degradable Coacervate Conjugate for Local Cancer Immunotherapy. *ACS Biomater Sci Eng* **2020,** *6* (9), 4993-5000.

163. Kaps, L.; Leber, N.; Klefenz, A.; Choteschovsky, N.; Zentel, R.; Nuhn, L.; Schuppan, D., In Vivo siRNA Delivery to Immunosuppressive Liver Macrophages by alpha-Mannosyl-Functionalized Cationic Nanohydrogel Particles. *Cells* **2020,** *9* (8).

164. Sugiura, T.; Kawata, S.; Okada, T., Fluorescence imaging with a laser trapping scanning near-field optical microscope. *Journal of Microscopy* **1999,** *194*, 291-294.

165. Goel, S.; Zhang, G.; Dogra, P.; Nizzero, S.; Cristini, V.; Wang, Z.; Hu, Z.; Li, Z.; Liu, X.; Shen, H.; Ferrari, M., Sequential deconstruction of composite drug transport in metastatic breast cancer. *Sci. Adv.* **2020,** *6*.

166. Ma, M.; Zhu, H.; Ling, J.; Gong, S.; Zhang, Y.; Xia, Y.; Tang, Z., Quasi-amorphous and Hierarchical Fe2O3 Supraparticles: Active T1-Weighted Magnetic Resonance Imaging in Vivo and Renal Clearance. *ACS Nano* **2020,** *14* (4), 4036-4044.

167. PallCorporation VividPlasma Separation Membrane DataSheet. (accessed 04.11.2019).

168. Gaus, H. J.; Gupta, R.; Chappell, A. E.; Ostergaard, M. E.; Swayze, E. E.; Seth, P. P., Characterization of the interactions of chemically-modified therapeutic nucleic acids with plasma proteins using a fluorescence polarization assay. *Nucleic Acids Res* **2019,** *47* (3), 1110-1122.

169. Gupta, V.; Bhavanasi, S.; Quadir, M.; Singh, K.; Ghosh, G.; Vasamreddy, K.; Ghosh, A.; Siahaan, T. J.; Banerjee, S.; Banerjee, S. K., Protein PEGylation for cancer therapy: bench to bedside. *J Cell Commun Signal* **2019,** *13* (3), 319-330.

170. Jevsevar, S.; Kunstelj, M.; Porekar, V. G., PEGylation of therapeutic proteins. *Biotechnol J* **2010,** *5* (1), 113-28.

171. Bauer, T. A.; Horvat, N. K.; Marques, O.; Chocarro, S.; Mertens, C.; Colucci, S.; Schmitt, S.; Carrella, L. M.; Morsbach, S.; Koynov, K.; Fenaroli, F.; Blumler, P.; Jung, M.; Sotillo, R.; Hentze, M. W.; Muckenthaler, M. U.; Barz, M., Core Cross-Linked Polymeric Micelles for Specific Iron Delivery: Inducing Sterile Inflammation in Macrophages. *Adv Healthc Mater* **2021,** *10* (19), e2100385.

172. Kaps, L.; Huppertsberg, A.; Choteschovsky, N.; Klefenz, A.; Durak, F.; Schrors, B.; Diken, M.; Eichler, E.; Rosigkeit, S.; Schmitt, S.; Leps, C.; Schulze, A.; Foerster, F.; Bockamp, E.; De Geest, B. G.; Koynov, K.; Rader, H. J.; Tenzer, S.; Marini, F.; Schuppan, D.; Nuhn, L., pH-degradable, bisphosphonate-loaded nanogels attenuate liver fibrosis by repolarization of M2-type macrophages. *Proc Natl Acad Sci U S A* **2022,** *119* (12), e2122310119.

8. List of Figures

9. List of Tables

10. Symbols

I	Intensity
t	Time
τ	Fluorescence lifetime
τ_{Av}	Average fluorescence lifetime
τ_1	Short fluorescence lifetime
τ_2	Long fluorescence lifetime
A_1	Relative amplitude of τ_1
A_2	Relative amplitude of τ_2
$G(\tau)$	Autocorrelation function
$F(t)$	Fluorescence intensity signal
$\langle \dots \rangle$	Time average
N	Average number of particles
S	Structure parameter
τ_{D}	Diffusion time
τ_{T}	Decay time of the triplet state
f_{T}	Fraction of the triplet state
c	Concentration
M	Molar mass
V_{Obs}	Observation volume
r_0	Width of V_{Obs}
z_0	Height of V_{Obs}
R_{H}	Hydrodynamic radius
k_{B}	Boltzmann constant
T	Temperature
η	Viscosity
λ	Wavelength

11. Scientific Contributions

Article

Stefan Kramer, Dennis Svatunek, Irina Alberg, Barbara Grafen, **Sascha Schmitt**, Lydia Braun, Arthur H. A. M. van Onzen, Raffaella Rossin, Kaloian Koynov, Hannes Mikula, Rudolf Zentel; HPMA-Based Nanoparticles for Fast, Bioorthogonal iEDDA Ligation. Biomacromolecules 2019, 20, 3786-3797

Article

Tobias A. Bauer, Natalie K. Horvat, Oriana Marques, Sara Chocarro, Christina Mertens, Silvia Colucci, **Sascha Schmitt**, Luca M. Carrella, Svenja Morsbach, Kaloian Koynov, Federico Fenaroli, Peter Blümler, Michaela Jung, Rocio Sotillo, Matthias W. Hentze, Martina U. Muckenthaler, Matthias Barz, Core Cross-Linked Polymeric Micelles for Specific Iron Delivery: Inducing Sterile Inflammation in Macrophages. Adv. Healthcare Mater 2021, 2100385

Article

Leonard Kaps, Anne Huppertsberg, Niklas Choteschovsky, Adrian Klefenz, Feyza Durak, Babara Schrörs, Mustafa Diken, Emma Eichler, Sebastian Rosigkeit, **Sascha Schmitt**, Christian Leps, Alicia Schulze, Friedrich Foerster, Ernesto Bockamp, Bruno G. De Geest, Kaloian Koynov, Hans-Joachim Räder, Stefan Tenzer, Federico Marini, Detlef Schuppan, Lutz Nuhn, pH-degradable, bisphosphonate-loaded nanogels attenuate liver fibrosis by repolarization of M2-type macrophages. PNAS 2022, 119, No. 12

Article

Anne Huppertsberg, Leonard Kaps, Zifu Zhong, **Sascha Schmitt**, Judith Stickdorn, Kim Deswarte, Francis Combes, Christian Czysch, Jana De Vrieze, Sabah Kasmi, Niklas Choteschovsky, Adrian Klefenz, Carolina Medina-Montano, Pia Winterwerber, Chaojian Chen, Matthias Bros, Stefan Lienenklaus, Niek N. Sanders, Kaloian Koynov, Detlef Schuppan, Bart N. Lambrecht, Sunil A. David, Bruno G. De Geest, Lutz Nuhn,

	Squaric Ester-Based, pH-Degradable Nanogels: Modular Nanocarriers for Safe, Systemic Administration of Toll-like Receptor 7/8 Agonistic Immune Modulators J. Am. Chem. Soc. 2021, 143, 9872-9883
Review article	**Sascha Schmitt**, Lutz Nuhn, Matthias Barz, Hans-Jürgen Butt, Kaloian Koynov, Shining Light on Polymeric Drug Nanocarriers with Fluorescence Correlation Spectroscopy; Macromol. Rapid Commun. 2022, 2100892
Article	**Sascha Schmitt**, Anne Huppertsberg, Adrian Klefenz, Leonard Kaps, Volker Mailänder, Detlef Schuppan, Hans-Jürgen Butt, Lutz Nuhn, Kaloian Koynov, Fluorescence Correlation Spectroscopy Monitors the Fate of Degradable Nanocarriers in the Blood Stream; Biomacromolecules 2022, 23, 1065−1074